Dissertation presented to the Instituto Tecnológico de Aeronáutica, in partial fulfillment of the requirements for the degree of Master of Science in the Graduate Program of Physics, Field of Nuclear Physics.

Valéria Cristina Souza do Vale

STUDIES OF SCINTILLATION LIGHT AND IONIZATION CHARGE PRODUCTION IN LIQUID ARGON

Dissertation approved in its final version by signatories below:

Franciole da Cunha Marinho

Prof. Dr. Franciole Marinho
Advisor

Campo Montenegro
São José dos Campos, SP - Brazil
2025

Cataloging-in Publication Data
Documentation and Information Division

Vale, Valéria Cristina Souza do
Studies of scintillation light and ionization charge production in Liquid Argon / Valéria Cristina Souza do Vale.
São José dos Campos, 2025.
139f.

Dissertation of Master of Science – Course of Physics. Area of Nuclear Physics – Instituto Tecnológico de Aeronáutica, 2025. Advisor: Prof. Dr. Franciole Marinho.

1. Neutrinos. 2. Cintilação. 3. Interações de partículas. 4. Detecção de neutrinos. 5. Argônio. 6. Propagação da luz. 7. Física nuclear. 8. Física. I. Instituto Tecnológico de Aeronáutica. II. Title.

BIBLIOGRAPHIC REFERENCE

VALE, Valéria Cristina Souza do. **Studies of scintillation light and ionization charge production in Liquid Argon**. 2025. 139f. Dissertation of Master of Science – Instituto Tecnológico de Aeronáutica, São José dos Campos.

CESSION OF RIGHTS

AUTHOR'S NAME: Valéria Cristina Souza do Vale
PUBLICATION TITLE: Studies of scintillation light and ionization charge production in Liquid Argon.
PUBLICATION KIND/YEAR: Dissertation / 2025

It is granted to Instituto Tecnológico de Aeronáutica permission to reproduce copies of this dissertation and to only loan or to sell copies for academic and scientific purposes. The author reserves other publication rights and no part of this dissertation can be reproduced without the authorization of the author.

Valéria Cristina Souza do Vale
Marshal Eduardo Gomes Square, 50.
12228-900 – São José dos Campos–SP

STUDIES OF SCINTILLATION LIGHT AND IONIZATION CHARGE PRODUCTION IN LIQUID ARGON

Valéria Cristina Souza do Vale

Thesis Committee Composition:

Prof. Dr.	Pedro José Pompeia	Chair	-	ITA
Prof. Dr.	Franciole Marinho	Advisor	-	ITA
Prof. Dr.	Wayne Leonardo Silva de Paula	Internal referee	-	ITA
Prof. Dr.	Marco André Ferreira Dias	External referee	-	UNIFESP

ITA

Dedico este trabalho a ti, aluno que lê minhas palavras. Tu deves questionar sem medo, mas com respeito – como quem aprende com os mais velhos. É assim, com respeito e curiosidade genuína, que tu vais construir a ciência.

Acknowledgments

The master's journey was marked by challenges, learning, and many achievements. Along the way, I was fortunate to have the support of people who were essential in making this work possible. I would like to thank everyone who contributed in any way to make this happen.

To my God, to Our Lady of Nazareth, to Lord Jesus, and to my guiding spirits. Thank you for all the protection and guidance. Thank you for hearing all my prayers.

I am deeply grateful to my dear mother. Thank you for your unconditional support, constant love, and for believing in me, even during the moments when I doubted myself. Thank you for being my foundation and my safe harbor.

I would like to thank my advisor, for his guidance and for the teachings that significantly contributed to the development of this work, as well as for the opportunity for academic and personal growth throughout this process.

To the professors and colleagues of the Graduate Program at ITA, thank you for the learning environment that made all the difference during this journey. A special thank you to Prof. Dr. Manuel Malheiro for his constant encouragement during my graduate journey, while he was still among us. I hope to guide my future students with the same enthusiasm you shared. Your legacy on Earth is unquestionable.

To my boyfriend. I am deeply grateful for everything you have done for me. Thank you for being such a sharp advisor and a present listener. Thank you for all your patience during my moments of stress, for your words of support and love. Thank you for encouraging me, for believing in me, and for the value you give to my work and academic life.

To my friends Gle, Suellen, Lucas, Agatha, Elvys, Filipe (Barca), Rebeca (Lolita Asamiya), Mary, Amanda, and Alana. You stood by my side with words of enthusiasm and good humor. Thank you so much for helping me maintain balance and lightness. Thank you, Yudi, for sharing your knowledge, for the recommendations of Neutrino Physics books, and for your friendship.

I am grateful to the Particle and Astroparticle Physics Group of UFRN for the shared knowledge, the friendship, and the warm welcome during my brief stay at the IIP. My time with you was profoundly enriching.

I would also like to express my gratitude to the UFV Particle Physics Study Group. Thank you for the seminars, debates, and the exchange of knowledge. Your openness in welcoming an external student like me was deeply appreciated. Through this collaboration, I found answers to many questions, expanded my understanding, and, without a doubt, made my Tuesday mornings far more inspiring.

To my beloved cats. Thank you for all the joyful and happy moments you gave me, for keeping me company during the many days (and nights) of study. You always made me smile with a head bump and a purr. This work belongs to you, too.

To Paysandu Sport Club, for winning the Copa Verde 2025. Watching Wolves matches helped ease some of the homesickness, even from the other side of the country.

I also thank the Coordination for the Improvement of Higher Education Personnel (CAPES) for the financial support during this graduate program.

"Meow."

(F.D.C. Willard)

"Meow."

(F.D.C. Willard)

Resumo

A física de neutrinos é um campo da física de partículas dedicado ao estudo das propriedades dessas partículas e suas interações com a matéria. Ainda que muitas características sejam conhecidas devido aos diversos esforços teóricos e experimentais ao longo de várias décadas, ainda há diversas questões em aberto a respeito dos neutrinos. Por isso, o desenvolvimento de tecnologias como detectores baseados em Câmaras de Projeção Temporal com Argônio Líquido (LArTPCs). Experimentos de nova geração, como o Deep Underground Neutrino Experiment (DUNE), desenvolvem essas tecnologias para a investigação de parâmetros de oscilação de neutrinos, violação de simetria CP e buscas por física além do modelo padrão. A quantificação da produção de cargas elétricas e luz de cintilação induzidas pela passagem de partículas relativísticas carregadas em argônio líquido é relevante para o funcionamento de LArTPCs. Este trabalho irá aprimorar o modelo fenomenológico LArQL, que descreve a anticorrelação entre a produção de cargas livres (Q) e luz de cintilação (L), incluindo efeitos de recombinação e cargas de escape em regiões de baixo campo elétrico. O modelo leva em consideração o número total de quanta produzidos, recombinação baseada no modelo de Birks, dependência do campo elétrico e a energia média por separação iônica. A pesquisa será organizada em duas etapas principais. Ajuste global: Integração de nove conjuntos de dados de recuos de elétrons (ER) em argônio líquido, correlacionando carga, cintilação, campo elétrico e energia depositada. Validação do modelo: Teste com 9 bancos de dados de ER não incluídos no ajuste para avaliar a precisão e robustez das estimativas. Os ajustes propostos melhoram a variância das estimativas de carga e cintilação para ER em $\sim$6,64% para os datasets incluídos no fit, conforme avaliado pela redução média nos valores de Soma de Resíduos Quadrados (SRQ) em relação ao modelo LArQL com os parâmetros originais. Além disso, para os dados não incluidos no fit todos os datasets apresentaram uma representação satisfatória pelo modelo, tanto para dados de luz e carga para diferentes experimentos.

Abstract

Neutrino physics is a branch of particle physics dedicated to studying the properties of these particles and their interactions with matter. Although many characteristics of neutrinos are known due to extensive theoretical and experimental efforts over several decades, numerous open questions remain. This motivates the development of technologies such as Liquid Argon Time Projection Chamber (LArTPC) detectors. Next-generation experiments, such as the Deep Underground Neutrino Experiment (DUNE), advance these technologies to investigate neutrino oscillation parameters, CP symmetry violation, and search for physics beyond the Standard Model. Quantifying the production of ionization charge and scintillation light induced by the passage of relativistic charged particles in liquid argon is crucial for the performance of LArTPCs. This work aims to improve the phenomenological model LArQL, which describes the anticorrelation between free charge (Q) and scintillation light (L) production, incorporating recombination and escape charge effects in low electric field regions. The model accounts for the total number of produced quanta, recombination based on Birks' model, electric field dependence, and the average energy per ion pair production. The research will be organized into two main stages. Global fit: Integration of nine electron recoil (ER) datasets in liquid argon, correlating charge, scintillation, electric field, and deposited energy. Model validation: Testing against nine ER datasets not included in the fitting process to assess the model's accuracy and robustness. The proposed adjustments improve the variance of charge and scintillation estimates for ER by $\sim 6.64\%$ for the datasets included in the fit, as evaluated by the average reduction in the Sum of Squared Residuals (SSR) compared to the original LArQL model parameters. Furthermore, for the datasets not included in the fit, the model provided a satisfactory representation of both light and charge data across different experiments.

List of Figures

List of Tables

List of Abbreviations and Acronyms

CC	Charged-Current
NC	Neutral-Current
ES	Elastic Scattering
CR	Cosmic Ray
CNO	Carbon-Nitrogen-Oxygen
DM	Dark Matter
ER	Electron Recoils
NR	Nuclear Recoils
HIP	Highly Ionizing Particle
LIP	Lowly Ionizing Particle
SM	Standard Model
SSM	Solar Standard Model
WIMP	Weakly Interactive Massive Particle
FD	Far Detector
ND	Near Detector
LAr	Liquid Argon
GAr	Gaseous Argon
XA	X-Arapuca
SURF	Stanford Underground Research Facility
LArTPC	Liquid Argon Time Projection Chamber
DUNE	Deep Underground Neutrino Experiment
GALLEX	Gallium Experiment
GNO	Gallium Neutrino Observatory
SNO	Sudbury Neutrino Experiment
Super-K	Super-Kamiokande
T2K	Tokai-to-Kamioka
NOνA	NuMI Off-axis ν_e Appearance
JUNO	Jiāngmén Underground Neutrino Observatory
DP	Dual-Phase

SP	Single-Phase
APA	Anode Plane Assembly
CPA	Cathode Plane Assembly
TPB	Tetraphenyl Butadiene
PEN	Polyethylene Naphthalate
PDS	Photo Detection System
PD	Photo Detector
LBL	Long-Baseline
SBL	Short-Baseline
PID	Particle Identification
PMT	Photomultiplier Tubes
S/N	Signal to Noise
SNB	Supernova Neutrino Burst
TOF	Time of Arrival
VUV	Vacuum Ultraviolet
WS	Wavelength Shifter
LSQ	Least Squares approximation
SSR	Sum of Squared Residuals
RMS	Root Mean Square

List of Symbols

S_1	Primary scintillation signal
S_2	Secondary scintillation signal (Electroluminescence)
S	Scintillation ratio
$\mathscr{R}$	Recombination
R	Collected charge factor
dE/dx	Deposited energy per unit length
ε	Electric field
χ_0	Escaping electrons factor
η_0	Fraction of missing photons
f_{corr}	Correction factor
S_0	Scintillation at null field
Q_∞	Maximum collectable charge
Q	Charge yield
L	Light yield
E	Energy
N_q	Number of quanta
N_{ion}	Number of ionizations
N_{ex}	Number of excitations
W_{ion}	Average energy expended per formation ion-electron pair
ρ_{LAr}	LAr density
M	Molar per liter
SNU	Solar Neutrino Unit
σ	Cross-section
L	Lepton number
$\hat{C}$	Charge operator
$\hat{P}$	Parity operator
ν_μ	Muon neutrino
ν_e	Electron neutrino
ν_τ	Tau neutrino

Contents

1 Introduction

The technology of Liquid Argon Time-Projection Chambers (LArTPC) is dedicated to experiments for neutrino detection through the quantification of scintillation light production and ionizing electric charges resulting from the passage of relativistic charged particles through the cryogenic volume composed of Liquid Argon (LAr). To enable the reconstruction of the particle trajectories and deposited energies, and the particles produced in the interaction of a neutrino with argon atoms in the detector's sensitive region, this cryogenic volume is subject to a strong electric field to produce a drag on the movement of electric charges toward an arrangement of anode wire planes[1 2 3].

Thus, it is possible to reconstruct the trajectories of these relativistic particles. Scintillation can occur due to both ionization and the excitation of argon atoms, also caused by the passage of these particles, which may lead to the formation of excimers or excited dimers, upon decaying a photon with a wavelength of 127 ± 10 nm is produced, an Vacuum Ultraviolet (VUV).

The LArQL is a phenomenological model proposed to express an anti-correlation relationship between the production of charges and scintillation light from the interaction of ionizing electrically charged particles with LAr, as well as other related quantities dependent on the deposited energy and the applied electric field in the cryogenic volume. One advantage of this model is its ability to predict data considering regions with low or zero-intensity electric fields for various experiments. The model uses the average number of total quanta produced, the energy deposition per unit length, the average energy expended per ion pair separation, a correction factor dependent on the deposited energy per unit length and the electric field, and a recombination factor from Birks' model[4].

The work aimed to improve the capability of estimating scintillation in LAr, which comes from the deposition of energy per unit length caused by the passage of relativistic particles through weak interactions in the sensitive region of LArTPCs, providing modeling contributions for scintillation estimations in LArTPCs. To this purpose, two specific objectives were defined for the development of this research: The first, consisted of a fit of the model parameters, performed with 9 datasets for the scintillation and charge recombination for electron recoils as a function of the applied electric field and the deposited energy, present in the literature, using as a method the minimization of the values of the Sums of Squared Residuals. The second objective focused on making estimates for electron recoils datasets not included in the fit to assess the quality of the adjustments.

The chapter 2 outlines the theoretical and experimental aspects of neutrino particles, including their proposal, discovery, characteristics, and parameters relevant to neutrino oscillation measurements.

The chapter 3 describes the LArTPC technology, addressing the features of single and dual-phase designs. It examines the mechanisms of productions of scintillation light production for both S_1 and S_2 light, within the cryogenic volume, its propagation, and the correlation between the energy deposited by ionizing particles and the transport of released electrons.

The chapter 4 provides an overview of the analyzed experimental datasets for electron recoils, detailing the apparatus, data treatment, and key results. The chapter is divided into two sections: About the datasets included in the fit and the datasets used for model comparison.

In chapter 5, the treatment of experimental data based on the LArQL phenomenological model is detailed, highlighting data optimization via the Least Squares Method. The scintillation and recombination graphs are presented to derive statistically adjusted global parameters that optimize nine experimental datasets (from refs.[5] [6] and [7]) by minimizing the residuals.

The results from the previous chapter are documented in chapter 6, including estimates for datasets excluded from the fit (from refs.[7] [8] [9] [10] and [11]) using the obtained global parameters and the alpha particles correction term. Finally, chapter 7 summarizes the conclusions of the study.

2 Neutrino Physics

This chapter gives a brief outline of neutrino physics. Section 2.1 covers a short history of neutrinos and their main properties in the Standard Model (SM). Section 2.2 presents the neutrino oscillation mechanism and its parameters, relating to the experiments designed to measure them. Lastly, section 2.3 discusses the neutrino mass hierarchy, the experimental approach, and the main neutrino sources used in experimental designs.

2.1 Neutrinos brief review

Following the discovery of natural radioactivity in 1896 by H. Becquerel[12], radioactivity was uncovered, particularly through the work of M. Curie and E. Rutherford[13]. In 1897 J. Thomson discovered the electron, the first known subatomic particle[14]. In 1899, the nuclear beta (β) decay:

$$n \rightarrow p + e^- + \nu_e \tag{2.1}$$

was discovered by E. Rutherford[15]. In 1934, the positron β decay:

$$p \rightarrow n + e^+ + \nu_e. \tag{2.2}$$

was first observed by I. Curie and F. Joliot[16].

In 1930, W. Pauli postulated the existence of an additional final state particle to explain the electron continuous energy spectrum observed, ensuring the conservation of energy and momentum for beta decays[17]. To solve the problem, this particle was hypothesized as a neutral fermion with spin $1/2$, the neutrino[18].

The neutrino hypothesis allowed E. Fermi 1934 to develop the first theoretical framework for describing the beta decay in nuclei, assuming that protons and neutrons form the nucleus. Also, Fermi suggested a procedure to detect neutrinos, that is an antineutrino colliding with a proton, which would produce a neutron and a positron in an inverse beta-decay[19]:

$$\bar{\nu}_e + p \rightarrow n + e^+. \tag{2.3}$$

2.1.1 Neutrinos Detection

Nowadays, it is known that neutrinos and anti-neutrinos, in analogy to the quark families, exist in three flavours. The electron (ν_e), muon (ν_μ) and tau neutrino (ν_τ). This section describes how these particles were first experimentally observed.

Neutrinos were first experimentally detected in 1956 by C. Cowan and F. Reines. At the Savannah River nuclear site (South Carolina, USA), Cowan and Reines used a reactor as an electron anti-neutrino ($\bar{\nu}_e$) source to detect neutrino interactions with protons. Their detector was composed of a tank filled with cadmium chloride dissolved in water ($CdCl_2$) with external scintillator volumes equipped with photomultiplier tubes (PMTs) to detect light produced by positron annihilation and a subsequent neutron capture as illustrated in fig. 2.1. Notice these were the final state particles of the reaction in eq. 2.3. This experiment allowed them to confirm the existence of what is now known as electron neutrinos[20].

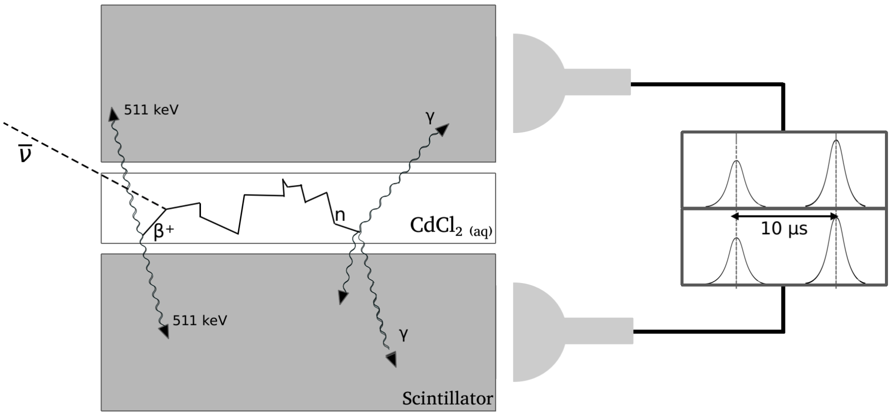

FIGURE 2.1 – The Reines-Cowan experimental setup. Adapted from[20]. The measurement was based on the time coincidence of the two photons produced on the positron annihilation ($E_\gamma = 511$keV), and the posterior Cd neutron capture ($\sim 10\mu$s delay).

This experiment led Fermi to express his gratitude in a letter, acknowledging the experimental confirmation of his theory, for which Reines was awarded the Nobel prize in Physics in 1995.

In 1962, an experiment at Brookhaven National Laboratory (BNL) led by L. Lederman, M. Schwartz, and J. Steinberger indicated the existence of the ν_μ produced through π decays:

$$\pi^\pm \rightarrow \mu^\pm + (\nu_\mu/\bar{\nu}_\mu). \tag{2.4}$$

The experiment consisted of a proton beam accelerated to an energy of $E \sim 15$ GeV in the Brookhaven Alternating Gradient Synchrotron (AGS), and directed to a beryllium target[21]. The collisions produced pions that decayed, according to the reactions in eq. 2.4, resulting in a collimated beam of muons and neutrinos. A 13 m-thick steel shield stopped the muons and allowed only (mostly) the neutrinos to reach the detector. Figure 2.2 illustrates the experiment.

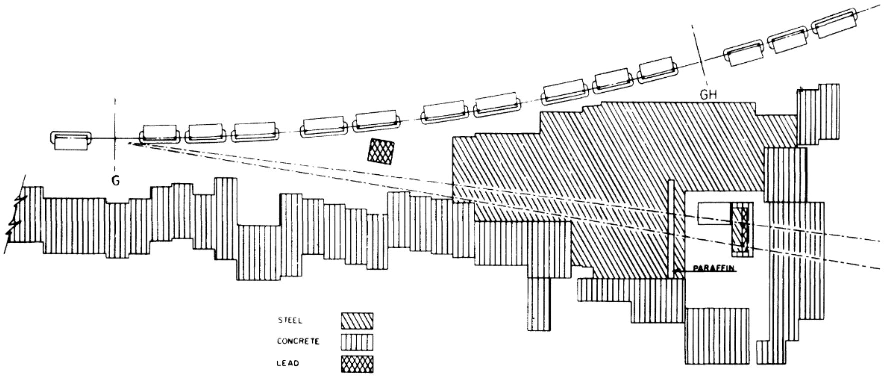

FIGURE 2.2 – The AGS neutrino experiment. The proton interactions at the target produced pions that decayed in flight and its final state particles flux stroke into a 13m thick iron shield wall with the neutrinos passing through. The neutrino interactions were then observed in an aluminum spark chamber, located behind the shield. Figure reproduced from[21].

The neutrino interactions observed were as indicated in eq. 2.5:

$$\begin{aligned} \nu_\mu + n &\rightarrow \mu^- + p, \\ \bar{\nu}_\mu + p &\rightarrow \mu^+ + n. \end{aligned} \tag{2.5}$$

Therefore the charged leptons in the final state were of a different flavour when compared to the ones produced in beta decays and in the Savannah River Experiment ($\nu_e/\bar{\nu}_e$). This indicated the produced neutrinos interacted differently when compared to the previous experiments suggesting those were neutrinos of a different flavour, $\nu_\mu/\bar{\nu}_\mu$. This discovery resulted in the Nobel prize in Physics in 1988[22].

After the discovery of the third charged lepton (τ), the ν_τ was first postulated by M. Perl in 1975[23]. The existence of the τ leptons was described as experimental evidence for new, at least, two particles. According to the reaction:

$$e^+ + e^- \rightarrow \tau^+ + \tau^- \rightarrow e^\pm + \mu^\mp + 4\nu \tag{2.6}$$

where it was noted the production of e, μ pairs with missing energy and momentum. These events were found using the Stanford Linear Accelerator Center Lawrence Berkley Laboratory (SLAC-LBL) magnetic detector at the cooling beams facility Stanford Positron Electron Accelerating Ring (SPEAR). Nowadays it is known that in the reaction proposed by M. Perl *et al.*: $e^+ + e^- \rightarrow \tau^+ + \tau^- \rightarrow e^\pm + \mu^\mp + \geq 2$ unknown particles, the "unknown particles" are 4 neutrinos as represented in eq. 2.6[23].

In July 2000, a team of 52 physicists from the Direct Observation of the Tau Neutrino (DONUT) Collaboration at Fermilab successfully provided direct evidence for the existence of the ν_τ, by observing the interactions:

$$\begin{aligned}
&\nu_\tau + N \rightarrow \tau^- + X, \\
&\text{with: } \tau^- \rightarrow \mu^-, e^- + \nu_{\mu,e}\nu_\tau, \\
&\text{or: } \tau^- \rightarrow h^- + \nu_\tau,
\end{aligned} \tag{2.7}$$

where N represents a nucleon, the X is any possible final state particle, and h an hadron[24].

The experiment was specifically designed to detect the Charged Current (CC, see subsection 2.1.2) interactions of the ν_τ and its charge conjugate and utilized a proton beam from the Fermilab Tevatron, which interacted with a tungsten beam dump to produce a flux of neutrinos. These interactions were identified by observing the production of the τ lepton, which has a lifetime of 2.9×10^{-13} seconds, as the only lepton produced at the primary vertex [25].

The detector as represented in fig. 2.3 (left) consisted of a scintillation counter veto wall to filter non-neutrinos events, an emulsion target for event capture near the interaction region, trigger hodoscopes, an analyzing magnet for momentum measurement, drift chamber to reconstruct particles trajectory, an electromagnetic calorimeter and a muon identifier. At the beam energy used in the DONUT experiment, 800 GeV, the τ lepton decays within 2 mm from the interaction vertex, producing a single charged particle. Figure 2.3 (right) shows that the τ decays into a charged particle and two non-detected neutrinos. Therefore, this decay appears as a distinct single-charged particle trajectory with an identifiable kink.

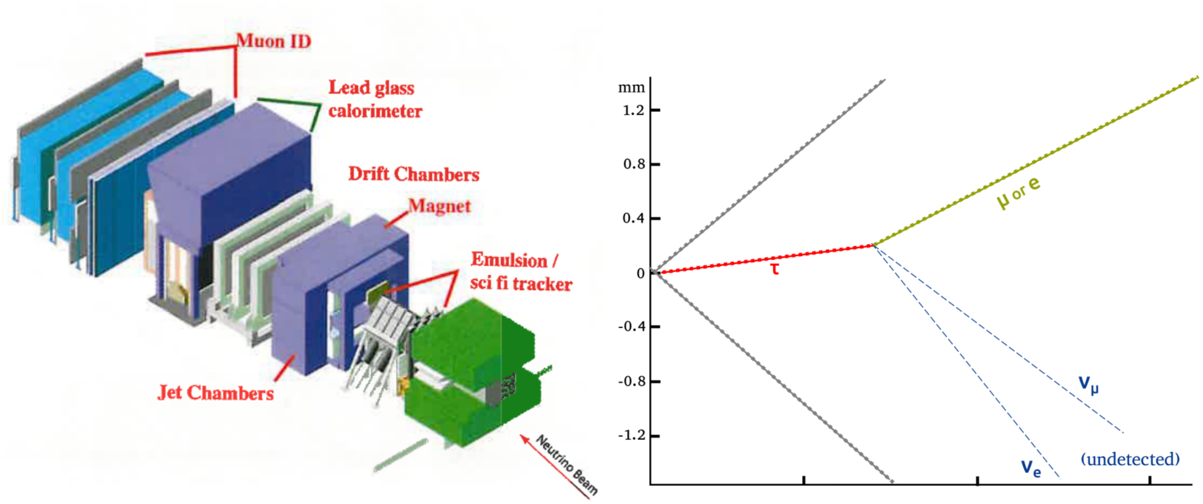

FIGURE 2.3 – The DONUT detector. At the right, the final state particles' trajectory, represented in eq. 2.7. The red line represents the τ, which decays into a lepton e or μ with a trajectory kink and two neutrinos. Figure taken from[25].

2.1.2 Neutrinos in the Standard Model

The SM is a gauge theory describing three fundamental forces—electromagnetic, weak, and strong- interactions experienced by the fundamental particles[26]. Neutrinos are elementary particles in the Standard Model (SM), classified as leptons with spin $1/2$, are electrically neutral and do not interact via the electromagnetic force, but participate in weak interactions mediated by the $W^{\pm}$ (for CC interactions) and Z^0 (for Neutral Current, or NC, interactions) bosons. Neutrinos are introduced in the SM as massless particles, meaning that the neutrino flavour would be conserved. However, experimental evidence has demonstrated that neutrinos change flavour as they propagate (neutrino oscillation), indicating that neutrinos have mass[27] [28].

Symmetries: Parity and Charge

Parity is a symmetry operation that inverts spatial coordinates, transforming $\overrightarrow{x} \rightarrow -\overrightarrow{x}$ and can be represented in quantum mechanics by the $\hat{P}$ operator. Parity is conserved in all fundamental interactions of elementary particles except for weak interactions.

The violation of the P symmetry was first experimentally observed by C. S. Wu in 1957[29]. This was achieved using an apparatus to observe the asymmetry of the distributions of the angles between the emitted β particles' momentum and the direction of polarization of the decaying ^{60}Co nucleus.

$$^{60}Co \rightarrow {}^{60}Ni + \beta^{-} + \bar{\nu}_e + 2\gamma \ (2.82\text{MeV}). \tag{2.8}$$

The β particles' angular asymmetry was observed by comparing the angular distributions measured for both ^{60}Co vertical polarizations. Figure 2.4 shows the apparatus used in the experiment. The β emissions were detected using an anthracene sample which acted as a scintillator detector positioned inside the cryostat, near 2 cm from the cobalt source. Two sodium iodide (NaI) scintillator counters were positioned on the equatorial and polar planes of the source to monitor the γ emissions. The beta asymmetry observed in Wu's experiment led to the conclusion of parity violation in weak interactions.

The charge transformation, represented by the operator $\hat{C}$, converts a particle into its corresponding antiparticle. Charge symmetry is conserved in all fundamental interactions of elementary particles, except in weak interactions. For instance, a W^{-} boson can couple with a left-handed electron (e_L^-) but the charge conjugate of such transition is not observed in nature ($W^{+} \rightarrow e_L^{+}\nu$)[30].

Although C and P symmetries are not conserved in weak interactions, one could argue that the composed CP operator is. For example, in the W boson leptonic transitions, CP is perfectly conserved. However, this symmetry is observed to be violated in certain interference phenomena, as an example, in neutral kaon decays (K-meson)[31].

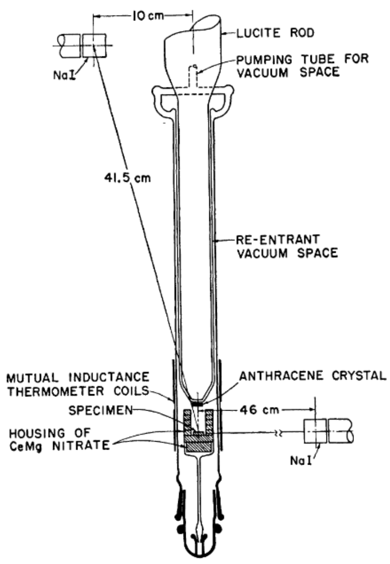

FIGURE 2.4 – Wu's experimental setup. Figure taken from[29]. The β emissions were detected with the anthracene crystal positioned near from ^{60}Co source. The anthracene scintillation was detected with two NaI scintillation counters placed on equatorial and polar planes.

CP-violation was first observed in 1964, in an experiment led by J. Cronin and V. Fitch that involved the K-meson decays[32]. The experimental setup was built on the Brookhaven AGS with K-mesons produced on the collisions of a 30 GeV proton beam directed to a Be target. The detector (see fig. 2.5) consisted of a helium volume to observe the K^0 ($d\bar{s}$) decays in STP conditions, two spectrometers composed of spark chambers for track determination, separated by a magnetic field of 178 kG-in for determining particles' charge and momentum, and a triggering system that was equipped with water Čerenkov detectors, to detect the signals from particles faster than light in water and scintillator detectors, to detect charged particles, both positioned behind the spectrometers.

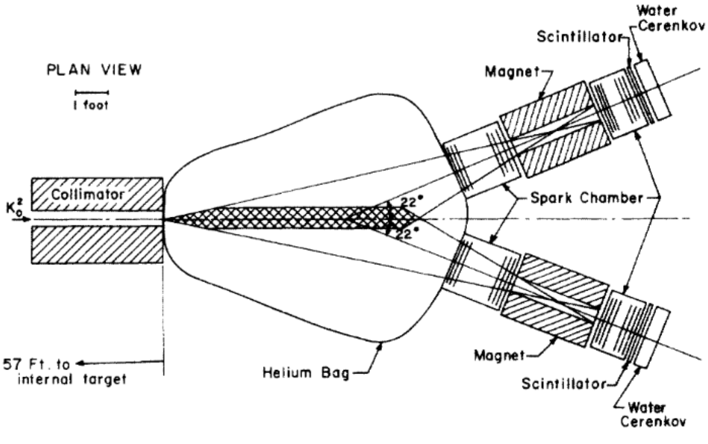

FIGURE 2.5 – Experiment conducted by Cronin and Fitch for the measurement of K meson decay rates. Figure taken from[32]. The setup was composed by two spectrometers for track determination in front of a triggering system with Čerenkov detectors and scintillation detectors.

The K-meson beam produces two kinds of particles with different time and decay modes. The long-lived kaons (K_L^0) have more probability to decay into three pions, with a mean lifetime of 5.18×10^{-8}. The short-lived kaons (K_S^0), with a mean lifetime of 8.958×10^{-11}, more likely to decay into two pions. The K_S^0 particles decay faster, meaning that only K_L^0 decays should be observed at the detectors. However, the measurements pointed out that either K_S and K_L were observed, meaning that K_L oscillated to K_S with CP values of +1 and -1, respectively, indicating occurrence of CP violation for such cases.

It is now known that the K_S and K_L are quantum mixtures of the mass states K^0 and $\bar{K}^0$:

$$\left|K_{S,L}(t)\right\rangle = \frac{1}{\sqrt{2(1+|\varepsilon|^2)}}[(1+\varepsilon)\left|K^0\right\rangle + (1-\varepsilon)\left|\bar{K}^0\right\rangle]e^{-i\lambda_{L,S}t}, \tag{2.9}$$

where ε is a complex parameter[26 33].

The discovery of CP violation in the neutrino sector will offer additional information about its role in the observed matter-antimatter asymmetry in the universe.

Lepton number

The total lepton number L is a quantum number that is also known as *lepton charge*, which represents the difference between the number of leptons and antileptons in reactions between elementary particles. Each generation of leptons has its own lepton number: L_e, L_μ and L_τ, as represented in tab. 2.1. Quarks and hadrons have a null lepton number.

TABLE 2.1 – Lepton number and charge (Q) for each lepton doublet.

Q	$L_e = 1$	$L_\mu = 1$	$L_\tau = 1$
-1	e^-	μ^-	τ^-
0	ν_e	ν_μ	ν_τ

Also, the individual flavour lepton numbers (L_e, L_μ, L_τ) are conserved during transitions, however, these are not conserved along neutrino oscillations (see sec. 2.2). Hence, one can introduce a more general quantity as:

$$L = L_e + L_\mu + L_\tau, \tag{2.10}$$

which restores overall lepton conservation in both situations.

2.2 Neutrino oscillations

In this section, the observations that led to the conclusion that neutrinos change their flavour as they propagate are discussed (subsection 2.2.1) and the neutrino oscillation formalism is introduced (subsection 2.2.2).

2.2.1 Neutrino Solar Experiments

The Sun produces its energy by hydrogen nuclear fusion. Two main nuclear fusion processes happen inside the star: the proton-proton (p-p) and Carbon, Nitrogen, and Oxygen (CNO) cycles. Within these cycles, nuclear reactions produce ν_es. These are listed in tab. 2.2 along with the corresponding neutrino energy production threshold and capture cross section with ^{37}Cl.

TABLE 2.2 – Neutrino-producing reactions in the Sun, energy thresholds and capture cross-section for ν_e by ^{37}Cl. Taken from[34].

Reaction	E_νMeV	σ(cm^2)
p-p Chain:		
$p+p\rightarrow d+e^++\nu_e$	≥ 0.42	0
$p+e^-+p\rightarrow d+\nu_e$	1.44	16×10^{-46}
$^3He+p\rightarrow {}^4He+e^++\nu_e$	≥ 18.8	3.9×10^{-42}
$^8B\rightarrow {}^8Be^*+e+\nu_e$	≥ 15	1.14×10^{-42}
CNO cycle:		
$^{13}N\rightarrow^{13}C+e^++\nu_e$	≥ 1.2	1.7×10^{-46}
$^{15}O\rightarrow^{15}N+e^++\nu_e$	≥ 1.73	6.8×10^{-46}

The Solar Standard Model (SSM) predicts the expected neutrino flux produced by nuclear fusion to be equal to $2\times10^{38}\nu_e s^{-1}$[35]. The SSM is based on the following assumptions:

- The Sun evolves in Static Equilibrium between pressure and gravity;
- The nuclear reactions in the Sun are the only source of energy;
- The condition of the Sun, in its main sequence, is considered homogeneous and highly convective;
- The energy of the Sun can be transferred by conduction, convection, radiation, and neutrino losses.

The Homestake experiment

Built between 1965 and 1967, aimed to perform measurements of ν_e fluxes from the Sun, with energies $E_\nu \geq 0.814$ MeV. The experiment mainly consisted of a tank with 6.1 m diameter and 14.6 m length, 95% filled with tetrachloroethylene (C_2Cl_4) and 5% filled with gaseous He, under 1.5 atm of pressure. Figure 2.6 shows the experimental apparatus which was positioned 1.478 km underground in the Homestake Mine, South Dakota, USA[36].

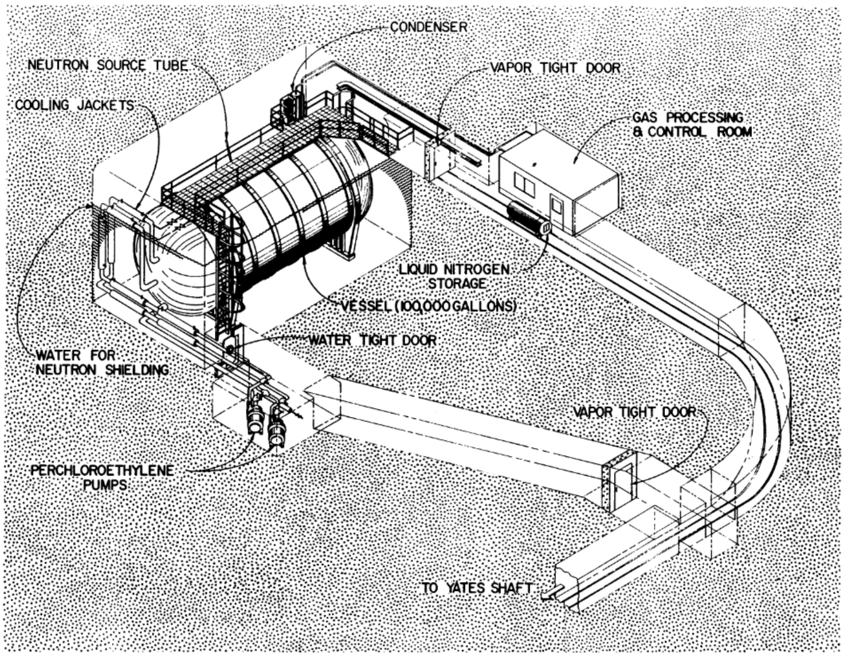

FIGURE 2.6 – The Homestake Solar Neutrino experiment. The main components are indicated and, in particular, the 615 t tank filled mostly with C_2 Cl_4 and the processing room containing the nitrogen-cooled charcoal trap, for extracting the Ar atoms produced during inverse β decays. Figure taken from[34].

The solar neutrino flux was measured by counting the argon atoms (^{37}Ar) produced in the inverse β decay of chlorine (^{37}Cl):

$$\nu_e + {}^{37}Cl \to {}^{37}Ar + e^-, \tag{2.11}$$

provided by the neutrino interactions with the ^{37}Cl, with an expected average rate of 1.7 interactions per day. The ^{37}Ar was extracted from the gaseous phase by a purification system with a nitrogen-cooled charcoal trap (see fig. 2.7). The Ar is easily extracted from the C_2Cl_4 by purging it with He as Ar is a noble element and does not make chemical bonds. The He+Ar mixture is transferred outside of the tank into a purification system, where Ar is then extracted from the mixture with the charcoal trap. After purification, He is fed back into the tank.

These Ar atoms were extracted from the tank and counted through their decays. The observed interaction rate per day was only 0.48 ± 0.04[26][34] in contrast to the higher rate expected according to the SSM. This neutrino deficit detected was then known as the Neutrino Solar Problem.

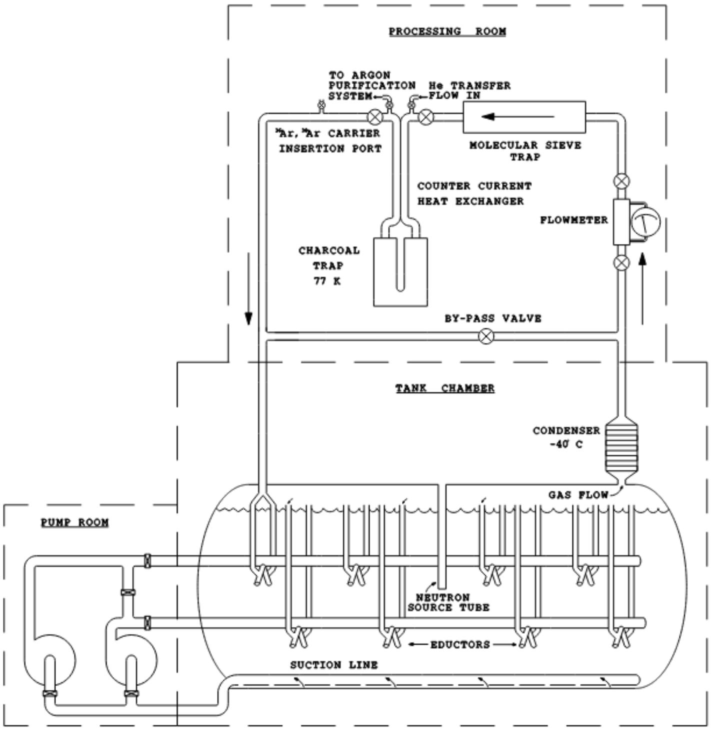

FIGURE 2.7 – Functioning of the Homestake Solar Neutrino experiment. Figure taken from[34]. The Ar is extracted from the liquid by purging it He. The He+Ar is transferred outside of the tank into a purification system, where Ar is then extracted from the mixture with a charcoal trap.

Gallium-based experiments

Two experiments employed gallium (^{71}Ga) as a target to detect low-energy neutrinos from the initial reaction of the p-p cycle. Both experiments employed neutrino interaction detection techniques for the following reaction:

$$^{71}Ga + \nu_e \rightarrow ^{71}Ge + e^-, \tag{2.12}$$

where the ^{71}Ge is extracted from the target and its late decay is used for counting the incoming neutrino interactions.

The Soviet-American Gallium Experiment (SAGE) in Baksan Neutrino Observatory (BNO), Russia, started to take data in 1990 and worked with 57 t of liquid metallic Ga [37]. The experiment was installed in an underground main chamber with 60 m length, 10 m width, and 12 m height, delimited by 60 cm of concrete and 6 m of steel on all sides, containing 7 chemical reactors. Figure 2.8 shows the configuration of one of the reactors. A Teflon tank with Ga is attached to band heaters which maintain Ga in a liquid state, and is mixed with Teflon vanes that release an oxidative solution: 200 L of deionized water, 5 L 7 M of HCl and 16 L of a 30% solution of H_2O_2. All of these are contained inside a steel tank. The Ge reacts by selective oxidation to the aqueous mixture, and its volume is then reduced by a factor of 8 and concentrated. The Ge is removed as a solution of $GeCl_4$ by a gas flow and trapped in 1 L of deionized water. Then, the GeH_4 is synthesized, purified, and directed to a proportional gas counter (80 ∼ 90% filled with Xe), which accounts for the proportion between the Ge mass and the carrier solution mass. The efficiency of extraction was about 77% before 1997 and 87% after. The neutrino capture rate measured was $67.2^{+7.2+3.5}_{-7.0-3.0}$ SNU (1 SNU - Solar Neutrino Unit = 10^{-36} captures per atom per second[38]).

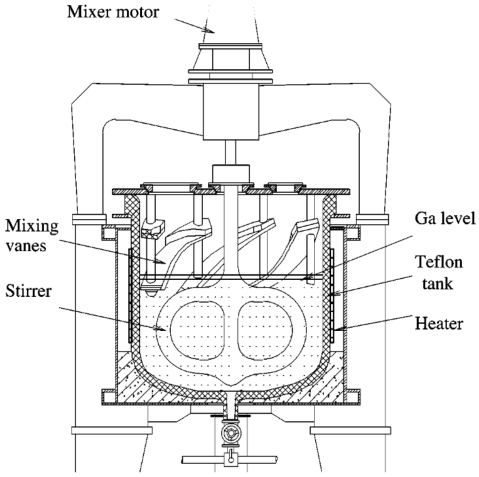

FIGURE 2.8 – The SAGE chemical reactor. Figure taken from[37]. The figure shows one of the 7 reactors. The main components indicated are the Teflon tank, mostly filled with Ga, and the vanes, responsible for dispersing the oxidant reagent (H_2O_2) for extracting Ge from liquid Ga.

The Gallium Neutrino Observatory experiment (GNO)[39], and the Gallium Experiment (GALLEX)[40], located at the Gran Sasso Underground Laboratory (LGNS), used 101 t of $GaCl_3$, with 30.3 t of Ga, and took data between 1991 and 2003 (From 1991 to 1999 → GALLEX. From 1999 to 2003 → GNO). As represented in fig. 2.9 it was composed of 2 tanks with 70 m^3 each, containing the target solution, $GaCl_3$. Before each run, 1 mg of other Ge isotopes (^{72}Ge, ^{74}Ge, and ^{76}Ge) were used for calibration. According to the reaction 2.12, in GALLEX, each Ge atom was incorporated into the $GeCl_4$ molecules at tank A, that are volatile in the presence of HCl and soluble in water. The ^{71}Ge and its carrier were extracted by 2000 m^3 of nitrogen for 20 h towards tank B by a gas pump. In this Tank Ge was absorbed in pure water (∼ 30 L) in absorption columns. The solution was then, concentrated into a 1 L volume and extracted back to be synthesized as GeH_4 and purified. The proportional counter was filled with 30% of Ge and 70% of Xe. The neutrino capture rate measured was $69.3 \pm 4.1 \pm 3.6$ SNU.

Both experiments had the ^{71}Ga isotope in its natural abundance (39.9%). The SSM prediction was $127.9^{+8.1}_{-8.2}$ SNU[35]. The rate measurements performed with these experiments also revealed a deficit of solar neutrinos, which was later explained by observations from subsequent experiments using water Čerenkov detectors.

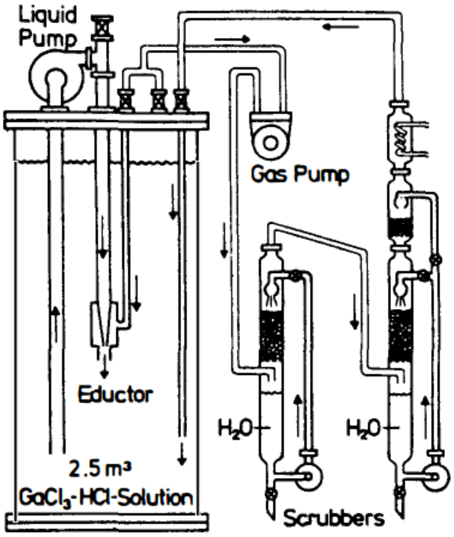

FIGURE 2.9 – The Gallium experiment[41]. The tank contains the target solution $GaCl_3$+HCl, which produces $GeCl_4$ (volatile) and was extracted with nitrogen, which was transferred by the gas pump to water columns to synthesize GeH_4. Then the Ge was purified and measured by proportional counters.

Water Čerenkov experiments

The Čerenkov radiation occurs when a relativistic charged particle pass through a dielectric medium, with its speed greater than the speed of light in that material ($v_p > c/n$), producing a ring of light, as illustrated in fig 2.10. The molecules, around the particles' trajectory, polarize as a response and, when returning to their ground state, release a blue wavelength photon.

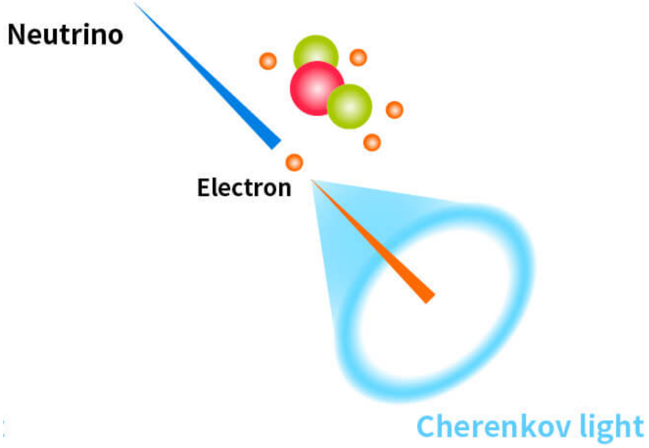

FIGURE 2.10 – The Čerenkov light emitted as a result of the passage of an electron produced on a neutrino interaction on water. Figure taken from[42].

In these experiments the Čerenkov light can be detected as signals detected by photomultiplier tubes installed on a large tank walls, enabling the real-time measurement of solar neutrinos.

The Kamioka Neutrino Detector (Kamiokande), shown in fig. 2.11, was a Water-Čerenkov detector, of 2140 t fiducial volume located in Kamioka mine in Gifu, Japan. It had 1071 20"

PMTs being 948 placed inside the detector, covering 20% of the inner surface, to collect Čerenkov light signals and 123 instrumented in the outer detector for cosmic ray (CR) muon tagging and detecting other outside activities. Initially designed for nucleon decay, it was modified in 1986 for solar ^{8}B-neutrino detection. Kamiokande started its measurements in 1987 and confirmed the solar neutrino problem indicated in the previous experiments. It also detected 12 electron events from the first observed neutrino supernova burst (SN 1987A), located in the Large Magellanic Cloud. This measurement resulted in the 2002 Nobel prize in physics for Dr. Masatoshi Koshiba[43] [44][45]. Along came its successor, Super-Kamiokande (Super-K), with a much larger volume and improved inner surface detector coverage of 40%. This detector started taking data in 1996[27][46]. The energy thresholds for Kamiokande and Super-K were of 6.5keV and 3.5 keV, respectively.

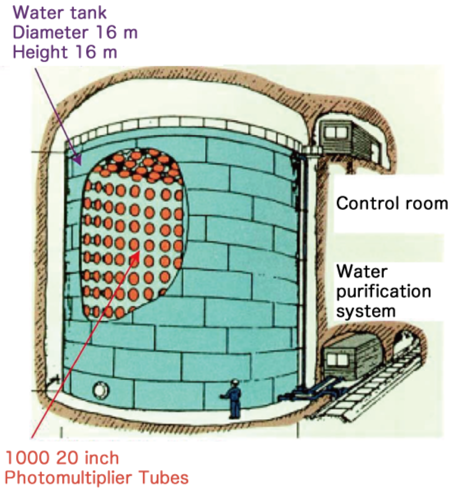

FIGURE 2.11 – The Kamioka Neutrino Detector. Figure taken from[42]. The PMTs on the inner walls detect the Čerenkov light emitted due to the charged particles produced in neutrino interactions.

Another important experiment based on the Water tank technique was the Sudbury Neutrino Observatory (SNO, see figs. 2.12) constructed in a nickel mine in Sudbury, Canada, 2000 m underground, using a Water Čerenkov detector with 1000 t of heavy water (D_2O) and equipped with 9456 PMTs, mounted on a stainless steel structure, in a 12 m diameter acrylic vessel to measure the ν flux from the Sun. The detector took data between 1999 and 2006.

It must be noted that in all Water experiments all types of neutrinos can interact through elastic scattering (ES) with electrons:

$$\nu_x + e^- \to \nu_x + e^- . \tag{2.13}$$

In the heavy water doped SNO neutrinos can also experience the following CC and NC

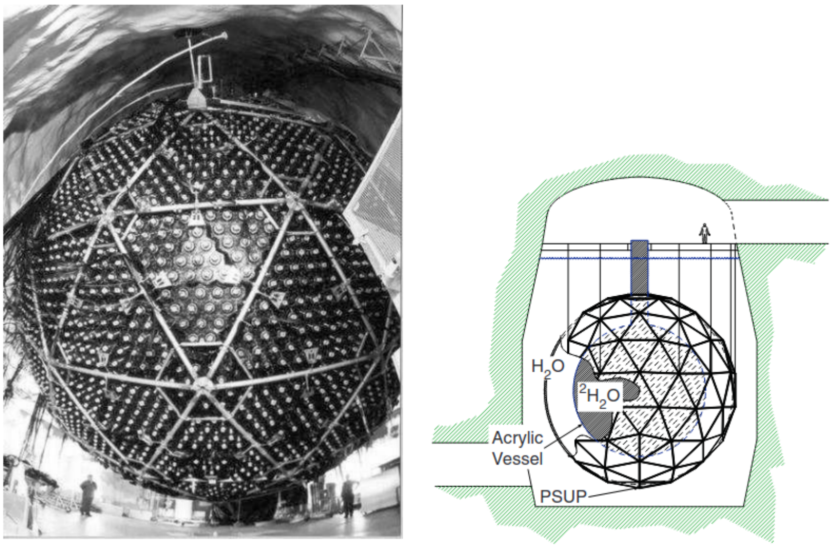

(a) The SNO detector photography. Taken from[47]. (b) The SNO detector scheme. Taken from[48].

FIGURE 2.12 – SNO detector. The 9456 PMTs were mounted at the stainless steel geodesic structure. The 12 m-diameter acrylic vessel stored 10^6 kg of D_2O was shielded with 7×10^6 kg of H_2O. (a) The construction of the Sudbury Neutrino Observatory (SNO). (b) The SNO detector scheme.

interactions:

$$\nu_e + d \to e^- + p + p, \tag{2.14}$$

$$\nu_x + d \to \nu_x + p + n, \tag{2.15}$$

$$ES_{rate} \propto \upsilon(\nu_e) + 0.154[\upsilon(\nu_\mu) + \upsilon(\nu_\tau)], \tag{2.16}$$

$$CC_{rate} \propto \upsilon(\nu_e) \tag{2.17}$$

$$NC_{rate} \propto \upsilon(\nu_e) + \upsilon(\nu_\mu) + \upsilon(\nu_\tau) \tag{2.18}$$

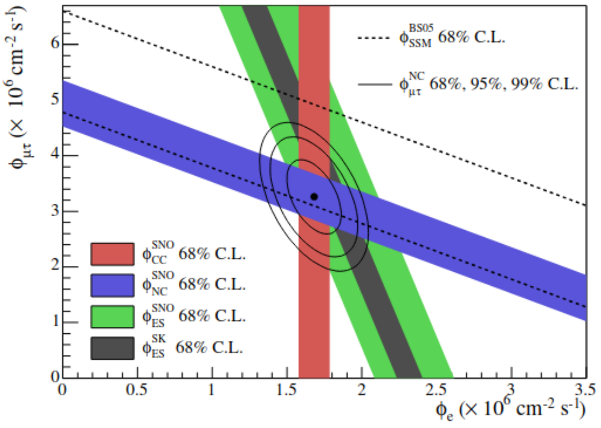

FIGURE 2.13 – The ν_e and $\nu_\mu + \nu_\tau$ flux limits from SNO, combined with Super-K. The solid bands represent the ES, CC, and NC reactions, and the dashed lines the SSM prediction. The intersection of these bands represents the best combination of all measurements. Taken from[49].

In 2000, a combined analysis with Super-K and SNO data was performed. Figure 2.13 shows the relationship of the ν_e and ν_μ + ν_τ fluxes from ES, CC, and NC reactions each represented by a different band color. The intersection between these bands indicates an appearance of $\phi_{\mu\tau}$ as part of the original ϕ_e from the Sun which oscillated along the way. In addition, the SSM prediction was endorsed[26 42].

2.2.2 Neutrino oscillation model

Neutrino oscillation is a quantum mechanics phenomenon in which a neutrino changes its flavour as it propagates through space. Neutrinos can be categorized according to their *weak interaction eigenstates* ν_e, ν_μ, and ν_τ, as well as mass eigenstates ν_1, ν_2, and ν_3. Through the observation of the charged lepton produced during CC interactions, the neutrino flavour can be identified.

In the scenario of non-zero neutrino masses, the mass eigenstates and weak eigenstates are not necessarily the same. For weak interactions involving leptons there exists a corresponding definition for neutrino mixing[30 26].

Neutrino flavours oscillate over large distances, which accounts for the discrepancy between the flux of (ν_e) observed in solar neutrino experiments (fig. 2.13). This is described by the interference of the quantum states of these particles as they propagate. A neutrino state can be represented by eq. 2.19, with $\alpha = e, \mu, \tau$:

$$|\nu_\alpha\rangle = \begin{pmatrix} \nu_e \\ \nu_\mu \\ \nu_\tau \end{pmatrix}. \tag{2.19}$$

It can also be represented by linear combinations of the neutrino mass eigenstates ν_i $(i = 1,2,3)$[30 26]:

$$|\nu_\alpha\rangle = \sum_i U_{\alpha i} |\nu_i\rangle\,, \tag{2.20}$$

where $U_{\alpha i}$ is the Pontecorvo-Maki-Nakagawa-Sakata (PMNS) matrix, expressed as a 3 × 3 rotation matrix[50 51]:

$$U_{\alpha i} = \begin{pmatrix} U_{e1} & U_{e2} & U_{e3} \\ U_{\mu 1} & U_{\mu 2} & U_{\mu 3} \\ U_{\tau 1} & U_{\tau 2} & U_{\tau 3} \end{pmatrix}$$

$$= \begin{pmatrix} 1 & 0 & 0 \\ 0 & c_{23} & s_{23} \\ 0 & -s_{23} & c_{23} \end{pmatrix} \begin{pmatrix} c_{13} & 0 & s_{13}e^{-i\delta_{CP}} \\ 0 & 1 & 0 \\ -s_{13}e^{-i\delta_{CP}} & 0 & c_{13} \end{pmatrix} \begin{pmatrix} c_{12} & s_{12} & 0 \\ -s_{12} & c_{12} & 0 \\ 0 & 0 & 1 \end{pmatrix}, \tag{2.21}$$

with $c_{ij} = \cos\theta_{ij}$ and $s_{ij} = \sin\theta_{ij}$, where δ_{CP} is the CP phase, which is non-zero if CP symmetry is violated during neutrino oscillations. Both phases have intervals equal to $0 \leq \delta \leq 2\pi$. Equation 2.22 also has three rotation angles: θ_{23}, θ_{12}, and θ_{13} with $0 \leq \theta_{ij} \leq \frac{\pi}{2}$:

$$\begin{aligned} \sin^2\theta_{12} &\equiv \frac{|U_{e2}|^2}{1-|U_{e3}|^2}, \\ \sin^2\theta_{23} &\equiv \frac{|U_{\mu 3}|^2}{1-|U_{e3}|^2}, \\ \sin^2\theta_{13} &\equiv |U_{e3}|^2. \\ \cos^2\theta_{12} &\equiv \frac{|U_{e1}|^2}{1-|U_{e3}|^2}. \end{aligned} \tag{2.22}$$

These angles are measured in atmospheric, solar, and reactor neutrino, performed at short distances ($L \sim 1$ Km), respectively[33 52], see tab. 2.3.

The relativistic energy for a neutrino can be written as:

$$E_i = \sqrt{m_i^2 + p_i^2} \simeq p_i + \frac{m_i^2}{2E}, \tag{2.23}$$

and the mass eigenstates' time dependence is described by the plane wave, with $\hbar = c = 1$:

$$|\nu_i(t)\rangle = e^{-i(E_i t)} |\nu_i(0)\rangle. \tag{2.24}$$

a neutrino with flavour ν_α, emitted by a source at $t = 0$, propagates with time into a state

$$|\nu_\alpha(t)\rangle = \sum_i U_{\alpha i} e^{-iE_i t} |\nu_i\rangle, \tag{2.25}$$

and the probability for flavour transitioning ($\nu_\alpha \to \nu_\beta$) is:

$$P(\nu_\alpha \to \nu_\beta) = |\langle \nu_\beta | \nu_\alpha(t)\rangle|^2 = \sum_{i,k} U_{\alpha i} U^*_{\beta i} U^*_{\alpha k} U_{\beta k} e^{-i(E_i - E_k)t}, \tag{2.26}$$

and considering $t = L$,[53]

$$P_{\nu_\alpha \to \nu_\beta}(L,E) \approx \sum_{k,i} U_{\alpha i} U^*_{\beta i} U^*_{\alpha k} U_{\beta k} e^{-\frac{i\Delta m^2_{ij} L}{2E}} \tag{2.27}$$

with the probabilities of oscillations depending on the differences of the squared masses $\Delta m^2_{ij} = m_i^2 - m_k^2$ and L the distance between the detector and the source of particles[33 54 30].

If $\alpha \neq \beta$, the probability is called *appearance*, and if $\alpha = \beta$, *survival*. Figure 2.14 illustrates both probabilities ($P(\nu_e \to \nu_\mu)$ and $P(\nu_e \to \nu_e)$) for a simplified model with just two flavours. In this model, there is only one mixing angle θ and the maximum mixing of an oscillation is proportional to the $\sin^2 2\theta$ value. For antineutrinos, the eq. 2.26 becomes:

$$P(\bar{\nu}_\alpha \to \bar{\nu}_\beta) \approx \sum_{k,i} U^*_{\alpha i} U_{\beta i} U_{\alpha k} U^*_{\beta k} e^{-\frac{i\Delta m^2_{ij} L}{2E}}.$$

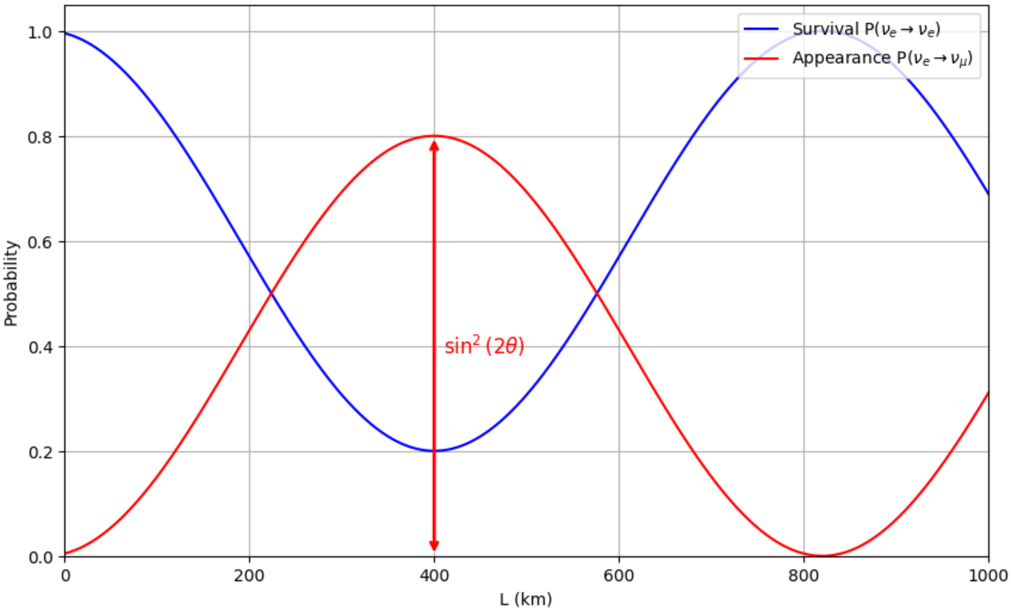

FIGURE 2.14 – Neutrino oscillation probability of two flavours. The probability that the neutrino has the same flavour as when the neutrino was emitted is called *survival* and is represented by the blue curve. The probability of oscillation to other flavours is called *appearance*, and the $P(\nu_e \to \nu_\mu)$ is represented by the red curve. The $\sin^2 2\theta = 0.8$ represents the maximum mixing for this case and the amplitude of the oscillation, with $E_\nu = 1$ GeV and $\Delta m^2 = 0.002$ eV^2. Adapted from[55].

If CP is violated, applying the CP transformation, will lead to $P(\nu_\alpha \to \nu_\beta) \neq P(\bar{\nu}_\alpha \to \bar{\nu}_\beta)$. Experimentally, this means that the difference in the measurement of oscillation probabilities for neutrinos and antineutrinos would indicate CP violation[33] [56].

The oscillation phase $\Delta m^2_{ik}(L/4E)$ depends on the ratio L/E, fundamental for LBL neutrino oscillation experiments design.

2.3 Neutrino masses

Considering a neutrino emitted by a source at a distance L from a detector, the time of arrival t of a massive neutrino has a delay Δt compared to the time a massless particle takes to travel the same path:

$$\Delta t = \frac{L}{v} - \frac{L}{c}, \tag{2.28}$$

where v is the massive neutrino speed. For a relativistic neutrino with mass $m \ll E$ and $c = 1$:

$$\frac{1}{v} = \frac{1}{\sqrt{1 - \frac{m2}{2E^2}}} \simeq 1 + \frac{m^2}{2E^2}, \tag{2.29}$$

equation 2.28, for a single neutrino, becomes:

$$\Delta t \simeq \frac{m^2}{2E^2} L. \tag{2.30}$$

The time duration of an emitted supernova neutrino burst at its source is unknown, and one can make a simple assumption of the observed burst at a L distance by assuming a Dirac delta type of burst. The time delay spread $\Delta T = T(E + \Delta E) - T(E)$ at the observation point for this hypothetical neutrino burst is:

$$\begin{aligned} \Delta T &= \frac{m^2 L}{2(E + \Delta E)^2} - \frac{m^2 L}{2E^2} \\ &= \frac{m^2 L}{2} \left[\frac{1}{E^2} - \frac{1}{E^2} - \frac{2\Delta E}{E^3} \right] \end{aligned} \tag{2.31}$$

$$\Delta T \simeq \frac{m^2}{E^2} L \frac{\Delta E}{E}, \tag{2.32}$$

where ΔE is the neutrino's energy distribution spread and $1/(E + \Delta E)^2 \approx \left(1/E^2\right) - \left(2\Delta E/E^3\right)$, obtained by Taylor's expansion. This time delay for the neutrino burst should be such $1/E^2$ that $\Delta T < \Delta T_{obs}$, where ΔT_{obs} is the observed time delay of the neutrino burst at the detector position. This implies an upper limit for the neutrino mass:

$$m \leq E \sqrt{\frac{E}{\Delta E} \frac{\Delta T_{obs}}{L}}. \tag{2.33}$$

Kamiokande detected 12 neutrino events from SN1987A and for these the average energy was $E \simeq 15$ MeV, with $\Delta T_{obs} \lesssim 12s$ and $\Delta E \sim 15$ MeV yielding an limit for the electronic antineutrino mass of:

$$m_{\nu_e} \lesssim 30.0 \text{ eV}. \tag{2.34}$$

Lower mass upper bounds have been achieved through model-dependent assumptions for the burst time structure around 1 eV. Neutrino masses are smaller by a factor of 10^6 than the e^- and by a factor of 10^9 of the τ[53].

These bounds are important to estimate the neutrino masses and their hierarchy. Considering that lighter neutrinos travel faster than heavier ones, they arrive at the detector at different times. These measurements would be different from the ones that had been produced during SN Bursts, indicating neutrino oscillations during the travel.

2.3.1 Mass hierarchy

Mass hierarchy refers to the current experimental indetermination of the relative mass order of the neutrino mass states m_1, m_2 and m_3. There are two possible ordinations for these masses.

- **Normal hierarchy:** Where the $m_1 < m_3$, it implies that $m_1 < m_2 < m_3$ and the mass difference Δm^2_{32} is *positive*.
- **Inverted hierarchy:** Where the $m_1 > m_3$, which implies that $m_3 < m_1 < m_2$ and the mass difference Δm^2_{32} is *negative*.

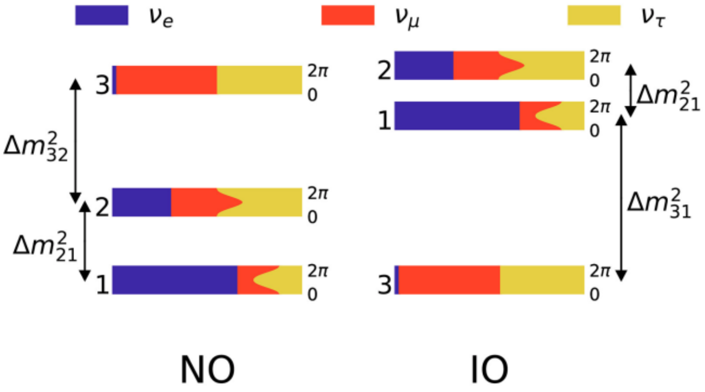

FIGURE 2.15 – Probability of detecting the neutrino flavour in the i-the mass eigenstate as the CP-violating phase, δ_{CP} is varied. The "NO" and "IO" mean "Normal Order" and "Inverted Order", respectively[57]. The colored blocks represent the mass eigenstates and probability of the neutrino being detected with a certain flavor. The blue block represents the ν_e, red for ν_μ and yellow for ν_τ.

As represented in fig. 2.15, each mass eigenstate ν_i has a flavour combination, which determines the probability of the flavour that the neutrino could be detected. The ν_1 mass eigenstate is composed by a mixture of 66.7% of ν_e, 16.7% of ν_τ and 16.7% of ν_μ. The ν_2 mass eigenstate is a mixture of 33.3% of ν_e, ν_μ and ν_τ, and the ν_3 mass eigenstate, 49% of ν_μ, 49% of ν_τ and 2% of ν_e detection probability. For that reason, the eigenstates are not associated with a single neutrino flavour, but a quantum mixture of them. The edges signed with "0" and "2π" in fig. 2.15 represent the δ_{CP} phase variation[58].

$$\Delta m^2_{21} = m^2_2 - m^2_1 \approx 8 \times 10^{-5} eV^2 \tag{2.35}$$

$$|\Delta m^2_{32}| = |m^2_3 - m^2_2| \approx 2 \times 10^{-3} eV^2 \tag{2.36}$$

The mass hierarchy also serves as a constraint on theoretical mechanisms proposed for neutrino mass generation, particularly models incorporating the seesaw mechanism, and impacts on interpreting experimental data from neutrinoless double beta decay searches. In addition, the mass hierarchy affects the understanding of flavor evolution in neutrinos emitted during core-collapse supernovae and provides the approach for the strategies employed to determine the CP-violating phase in the lepton sector, contributing to a broader comprehension of fundamental symmetries in particle physics[59].

2.3.2 Current status

Experiments and studies have been performed to clarify the information about neutrino oscillation parameters from solar, reactor, accelerator, and atmospheric neutrinos (see tab. 2.3)[30]. The results of the neutrino oscillations provided measurements of the squared differences of these masses. The determination of neutrino oscillation parameters is one of the main goals of today's experiments, e.g. Tokai to Kamioka (T2K)[60], NuMI Off-axis ν_e Appearance (NOvA)[61] and Jiāngmén Underground Neutrino Observatory (JUNO)[62].

TABLE 2.3 – Oscillation parameters and their determination depending on the type of experiment[63].

Experiment	Dominant	Important
Solar	θ_{12}	$\Delta m^2_{21}, \theta_{13}$
Reactor LBL (KamLAND)	Δm^2_{21}	θ_{12}, θ_{13}
Reactor SBL (Daya Bay, RENO, D-Chooz)	$\theta_{13}, \lvert\Delta m^2_{31,32}\rvert$	
Atmospheric (Super-K)		$\theta_{23\text{and}13}, \lvert\Delta m^2_{31,32}\rvert, \delta_{CP}$
Accel. LBL $\nu_\mu, \bar{\nu}_\mu$ disapp. (K2K, MINOS, T2K, NOνA)	$\lvert\Delta m^2_{31,32}\rvert, \theta_{23}$	
Accel. LBL $\nu_e, \bar{\nu}_e$ app. (MINOS, T2K, NOνA)	δ_{CP}	θ_{13}, θ_{23}

The next generation of neutrino experiments, such as DUNE has among its main goals:

- Precise measurements of neutrino mixing angles;
- Measurement of the CP phase δ_{CP} to determine if there is CP violation;
- Determination of the sign of Δm^2_{31}.

Such challenges demand research and design efforts to develop their detector technologies. In chapter 3 the Liquid Argon Time Projection Chamber (LArTPC) concept is introduced.

3 Liquid Argon Time Projection Chambers

The *Liquid Argon Time-Projection Chambers* (LArTPCs) are a technology used in particle physics experiments to study rare processes such as neutrino interactions. Their working principle is based on the acquisition of the ionized charges produced by charged particles to reconstruct trajectories and energies and analyze interaction mechanisms. The techniques developed for current LArTPC experiments are expected to enable the next generation of long-baseline neutrino oscillation experiments to broaden our understanding of neutrino physics[64] [2].

3.1 Functioning principles

A LArTPC comprises three main components. One of the components is a tank containing Liquid Argon (LAr), maintained at ideal pressure and temperature (around 87 K) by a cryogenic system, allowing argon to remain liquid. The other two components are the *cathode plane*, which establishes an electric field through the LAr by gradually reducing the voltage across the field cage, and the *anode plane*, arranged parallel to the cathode plane[1].

The operating principle of LArTPCs relies on the ionization and excitation of argon when a charged particle traverses the LAr, which generates ionization electrons and ions drifted by the electric field applied ε. An intense electric field is produced in the sensitive volume of the detector as a high voltage difference is kept between the anodic planes and the cathode. The time of arrival (TOF) of the electrons at the anode plane provides the z-coordinates of the track. A charged particle, originating from a natural or artificial source, interacts with argon atoms, depositing energy. A major fraction of the energy deposited is converted into amounts of free ionization electrons and scintillation light and, by convenience, can be estimated via the *deposited energy per unit length* (dE/dx).

LArTPCs can be classified into two designs: *single-phase* (SP), represented by fig. 3.1a, and *dual-phase* (DP), fig. 3.1b. In SP-LArTPCs, the ionization electrons drift toward the anode. The anodic wire planes form a grid with different orientations relative to the y-axis. The first layers generate bipolar induction signals as electrons pass through them, while the final layer

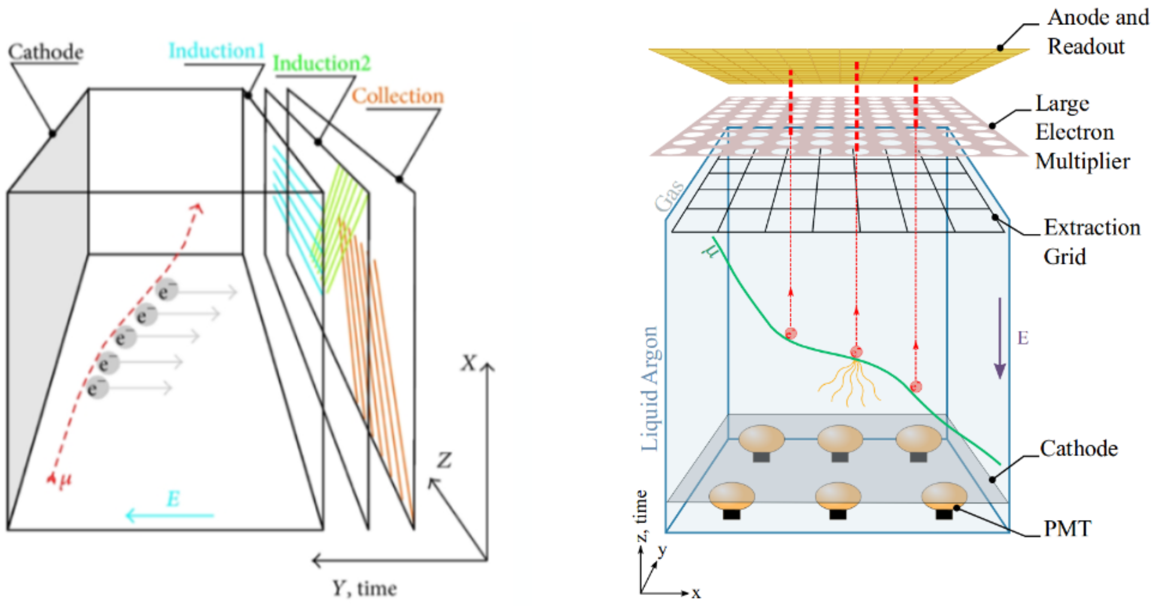

(a) Single-Phase LArTPC. Taken from[65].

(b) Dual-Phase LArTPC. Taken from[66].

FIGURE 3.1 – (a) The incoming neutrino interacts with a nucleus, producing relativistic charged particles that pass through the LAr medium. Electrons are produced via ionization and drift toward a set of anodic wires under a strong electric field applied in the volume. The VUV light is detected by PDs present on the electrodes of the LArTPC. (b) The drifted charges produced during ionization are directed to the extraction grid, located at the liquid/gas interface. The electroluminescence mechanism allows detection of the S_2 signal, providing charge measurement.

collects the drifting electrons, resulting in a monopolar signal[2]. The combination of the TOF and the y and x projections of the arriving particle provides 2D projections of the particle trajectory, which is then used to reconstruct the 3D image of the event. In DP-LArTPCs, the electrons drift to the gas phase above the LAr. The amplification of the signal occurs in the gas phase (GAr). For a detailed comparison of SP and DP-LArTPCs, see tab. 3.1. One can also reconstruct the total deposited energy of the interaction event by measuring the total amount of electric charge collected or converted.

Photons with wavelengths of approximately $127 \pm 10\,\mathrm{nm}$ are also released through scintillation. These *Vacuum Ultraviolet* (VUV) photons produce a *prompt light* signal in the detector volume, which is quickly collected by the Photon Detector (PD) devices. The detection information from the PDs is combined to determine the instant of the neutrino interaction (t_0) of events in the volume, also indicating when the *ionization electrons* begin to drift[3] [2].

LAr is a dense medium and an excellent scintillator, allowing for localization and tracking of the particle interactions due to the scintillation light, which traverses the detector on a timescale of nanoseconds and is shifted into the visible spectrum for collection by PDs. Closer wire spacing enhances event resolution within the detector; however, it increases the cost of readout electronics due to additional wire channels. Furthermore, closer spacing diminishes the signal-to-noise (S/N) ratio of ionization measurements since the ionization charge is divided among more wire channels[2] [3].

The S/N ratio is critical, as the ionization measurement directly reflects dE/dx of the relativistic particles, allowing for calorimetric and particle information. An additional advantage is the capability to detect both charged particles and the scintillation light produced during interactions, providing a supplementary method to characterize events by combining particle trajectory information with light signals.

The LArTPCs, however, face challenges. Maintaining argon in its liquid state requires a sophisticated cryogenic infrastructure. Moreover, detecting and amplifying electrical signals requires sensitive and noise-resistant electronics. Another challenge is the substantial volume of data generated, which necessitates robust processing and storage systems.

DUNE is an example of neutrino experiment based on the LArTPC technology[67] [3] [68] [69] [66] [56] [70] [2] [71] and will be further discussed in section 3.5. For the development of the work analysis presented in this dissertation data from the following LAr-based experiments are used and described in section 4: ARIS[7], ICARUS[5], MicroBooNE[72], ReD[11], Doke *et al.*[6], the ANKOK prototype[10], Hitachi *et al.*[73].

3.1.1 LAr characteristics

In the case of LArTPCs, argon is utilized as target because:

- LAr is the 3^{rd} most abundant gas in the Earth's atmosphere, making its extraction easy and cost-effective.
- LAr is a dielectric material with high density ($1.4\,\mathrm{g/cm^3}$) and moderate radiation length ($14\,\mathrm{cm}$)[74].
- It can be produced with good purity at relatively low cost[75] [76].
- It exhibits a high scintillation rate, on the order of 4×10^4 photons/MeV[7].
- LAr is transparent to scintillation light, allowing for its effective detection.
- It has high electron mobility ($500\,\mathrm{cm}^2 \cdot (V \cdot s)^{-1}$), does not attach electrons, and permits long drift distances[75] [74].
- It is chemically inert and can be liquefied using liquid nitrogen[75].
- Working with LAr allows for the identification of showers, derived from the ratio of the secondary scintillation signal (S_2) to the primary scintillation signal (S_1).

3.2 Interactions and detection of charged particles

Neutrinos interact with the detector through weak interaction processes, as outlined in ch. 2. The signal is detected from the charged final state particles produced during these interactions with relativistic velocities. The cross-section between neutrinos and other target particles is:

$$\sigma \approx \frac{sG_F^2}{(\hbar c)^4}, \tag{3.1}$$

where $\sqrt{s} = \sqrt{2mc^2E}$ representing the center-of-energy mass in which E is the energy of neutrino and m, the mass of the target and G_F the Fermi constant. Neutrinos have a smaller cross-section with e than with nucleons[77]. Neutrino cross-sections are small for all targets (from 10^{-17} to 10^{-15} mb (1 mb = 10^{-24} cm^2)[78], even though matter can be traversed by large fluxes of neutrinos, a few of them interact indicating the need for enormous volume detectors to be sufficiently sensitive to these processes. Once a neutrino interaction happens in such a large volume, the observation of its final state particles must be performed.

When a relativistic charged particle traverses a medium, it interacts electromagnetically with atomic electrons, primarily losing energy through ionization. For a singly charged particle with velocity $v = \beta c$ moving through a medium with atomic number Z and number density n, the dE/dx is described by the *Bethe-Bloch equation*:

$$\frac{dE}{dx} \approx -4\pi\hbar^2c^2\bar{\alpha}^2\frac{nZ}{m_ev^2}\left[\ln\left(\frac{2\beta^2\gamma^2c^2m_e}{I_e}\right) - \beta^2\right], \tag{3.2}$$

where I_e is the effective ionization potential of the material, approximately given by $I_e \approx 10\,\mathrm{Z\,eV}$, $\bar{\alpha}$ the dimensionless fine-structure constant ($\bar{\alpha} = e/4\pi$) and $\gamma = 1/\sqrt{1-(v^2/c^2)}$. For a specific medium, the ionization energy loss rate for a charged particle depends on its velocity. The term $1/v^2$ in eq. 3.2 indicates that dE/dx is increased for low-velocity particles. On the other hand, as $\beta \to 1$, dE/dx varies logarithmically with $(\beta\gamma)^2$. This results in a gradual "relativistic rise" in the ionization energy loss rate, which does not significantly depend on the material itself, except for its density ρ. The number density of atoms can be expressed as $n = \frac{\rho}{Am_u}$, where A is the atomic mass number and $m_u = 1.66 \times 10^{-27}$ kg is the unified atomic mass unit. Thus, we can rewrite eq. 3.2 as

$$\frac{1}{\rho}\frac{dE}{dx} \approx -\frac{4\pi\hbar^2c^2\bar{\alpha}^2}{m_ev^2m_u}\frac{Z}{A}\left[\ln\left(\frac{2\beta^2\gamma^2m_ec^2}{I_e}\right) - \beta^2\right]. \tag{3.3}$$

The dE/dx is proportional to Z/A; since atomic nuclei typically contain nearly equal numbers of protons and neutrons, Z/A remains approximately constant. Consequently, the rate of energy loss due to ionization is primarily proportional to density and does not significantly depend on the specific material[26].

Charged particles lose energy through ionization in the medium they traverse. For instance, muons with energies below about 100 GeV primarily lose energy through ionization, allowing them to travel considerable distances even in dense materials like iron. A 10 GeV muon loses approximately 13 MeV/cm in iron. Consequently, muons are highly penetrating particles, often traversing the entire detector while leaving a trail of ionization. This characteristic can be leveraged for muon identification, as other charged particles typically engage in different interaction types in addition to ionization energy loss[26]. Depending on the particle type, other energy-loss mechanisms may also occur originating short particle tracks or showers.

Detectors based on plastic and liquid scintillators have been employed in neutrino experiments. In an organic scintillator, the passage of a charged particle can leave molecules in an excited state. The subsequent decay of these excited states results in the emission of light. If this light emission occurs in the UV range, fluorescent dyes can be incorporated into the scintillator, such that they can absorb UV and re-emit photons in the blue range. This blue light can then be detected using PMTs designed for this purpose[26]. For noble element TPCs, the scintillation light emission occurs in the VUV range, and similar techniques are employed with Wavelength Shifters (WS).

3.2.1 Light mechanisms

3.2.1.1 S_1 light

As stated previously in Section 3.1, a portion of the energy deposited by ionizing particles leads to the creation of electron-ion pairs ($\mathrm{Ar}^+ + e$). At the same time, another fraction is converted into argon excitons (Ar^*). Both argon excitons and ions interact with other argon atoms, leading to the formation of molecular states such as Ar_2^* and Ar_2^+.

These molecular states, the *excimers*, decay emitting *scintillation light*, as depicted in fig. 3.2. The (Ar_2^*) exist in two excited states: singlet $\left({}^1\Sigma_u^+\right)$ and triplet $\left({}^3\Sigma_u^+\right)$, each with distinct decay times: $\tau_{fast} = 7$ ns for the singlet form and $\tau_{slow} = 1.5$ μs for triplet form. Scintillation light arises in Ar from the excited states of molecular argon excimers transitioning to their lowest energy unbound state. S_1 is the detected primary scintillation signal produced in LAr along charged particles trajectories[79] [80].

The production of scintillation photons is directly proportional to the energy deposited by the ionizing particle. The typical light yield in LAr is 4×10^4 photons/MeV in the absence of a drift field. Under electric field conditions such as $\varepsilon = 0.5$ kV/cm, this yield decreases to approximately 2.4×10^4 photons/MeV due to reduced recombination. Scintillation photons in pure LAr are challenging to detect since most photosensors are insensitive to these VUV wavelengths, and the photons can be absorbed during propagation. Consequently, PMTs are often equipped with WS or fluorescent materials[79].

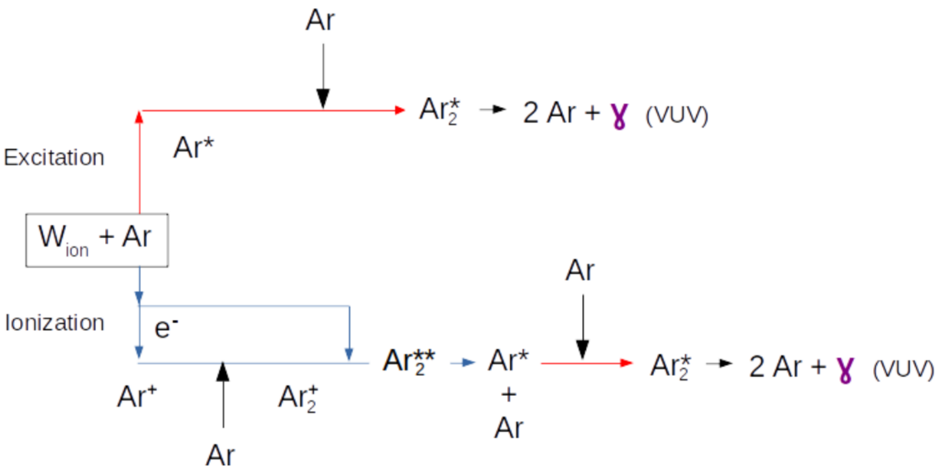

FIGURE 3.2 – Mechanisms of scintillation and ionization in LAr. Taken from[4].

The drift field acts to suppress part of the total amount of ionization electrons to recombine with argon ions, which limits light emission. On the other hand, an increase in electron recombination leads to greater light production but simultaneously diminishes the charge signal, as they are inversely related due to the principle of energy conservation. This can be mathematically expressed as:

$$L+Q=N_{ion}+N_{ex}, \tag{3.4}$$

where L gives the amount of scintillation photons produced, Q is related to the amount of free ionization electrons, and N_{ion} and N_{ex} refer to the average amount of ionization and excitations occurring, respectively. All these amounts are given per energy deposited unit.

The S_1 signal provides a fast time reference (t_0), corresponding to the moment at which the interaction occurs, which is crucial for triggering data acquisition and determining the 3D event location by combining it with the drift time of the charge signal. The term "Time Projection Chamber" originates from this use of t_0 for event reconstruction. Scintillation light aids in calorimetric reconstruction in two primary ways:

1. The t_0 provided by the light signal enhances the charge-based calorimetric measurements.
2. The total number of scintillation photons is proportional to the energy deposited, allowing for direct energy measurement from the light signal.

As the drift length increases, the charge signal degrades due to electron diffusion and recombination with impurities. Knowing the drift distance enables corrections that improve energy resolution. Additionally, the light signal supports particle identification (PID) by analyzing the ratio of fast to slow photons, which varies with particle type. Therefore, an efficient photon detection system is essential for LArTPCs.

3.2.1.2 S_2 light

In DP-LArTPCs (see fig. 3.1b), the *electroluminescence light signal*, or, S_2 is generated when drifted electrons reach the liquid-gas interface. A high electric field (ε_d), produced by an extraction grid, $\sim$ 5 mm above this interface in the GAr, extracts the electrons into the gas phase. The charge is then amplified inside Large Electron Multipliers (LEMs), with the photon output being directly proportional to the extracted charge. Unlike the S_1, the S_2 is proportional to the charge yield[66].

TABLE 3.1 – Comparison of SP and DP LArTPCs.

Feature	**SP**	**DP**
Drift Medium	LAr	LAr + GAr
Signal Amplification	Not Applicable	Occurs in GAr
N° of Signals Collected	S_1 + Induction Signals	$S_1 + S_2$
Overall Density	Higher due to LAr	Lower due to GAr
S/N Ratio	Higher Signal Collection	Lower Signal Collection
S2/S1 Ratio	Not Applicable	Applicable

3.3 Limitations of LArTPCs

There are challenges in designing a Photon Detection System (PDS) for large LArTPCs:

- LAr scintillation light occurs at 127 nm, outside the sensitivity range of most photosensors;
- In large detectors, light must travel significant distances, causing signal attenuation;
- Photon detectors must operate within strong electric fields.

Large surface PMTs are commonly used but struggle to detect 127 nm light and are affected by electric fields. To address this, they are often placed outside the active volume. In LArTPCs, PMTs are typically installed outside the LAr active volume with their optical window facing towards that region.

The WS such as Tetraphenyl Butadiene (TPB) and Polyethylene Naphthalate (PEN) convert VUV light into the visible range. A bialkali photocathode can detect approximately 20% of visible photons at 400 nm. TPB is highly efficient but challenging to handle due to its dust-like nature and the specialized deposition techniques required, especially for large detectors. TPB can be applied to a plate before or directly onto the PMT. The PEN, a thermoplastic, is easier to handle than TPB, making it more practical for large detectors. The DUNE collaboration (see sec. 3.5.) has proposed X-ARAPUCA (XA, see fig. 3.9) as an alternative solution, using dichroic filters and Silicon Photomultipliers (SiPMs) to trap and detect photons, with P-Terphenyl (PTP) as WS[74 81 82].

For optimal performance, highly pure argon is critical because photons and ionization electrons are absorbed by impurities. In pure LAr, photon absorption is minimal, with an attenuation length of 30 m at 2 ppm of N_2. Rayleigh scattering can further extend the photon propagation path, increasing the likelihood of absorption by impurities[83].

3.4 Contributions to Neutrino Physics

The LArTPCs have advanced the understanding of neutrino oscillations, particularly in exploring CP symmetry violation, which may provide information to help explain the dominance of matter over antimatter. LArTPCs have also been instrumental in studying neutrinos from atmospheric, solar, and accelerator-produced sources, providing key insights into the neutrino mass hierarchy and other fundamental properties.

Investigating the neutrino sector is of interest as it offers ways of probing for physics beyond the SM, with experiments like DUNE playing a key role. DUNE combines the world's most intense neutrino beam, a deep underground site, and large LAr detectors to address some of the most fundamental questions in particle physics[56 66]. In LArTPCs, the particle tracks, as seen in fig. 3.3, are characterized by their produced electric charges (dQ/dx) and dE/dx. This procedure is referred to as particle identification (PID).

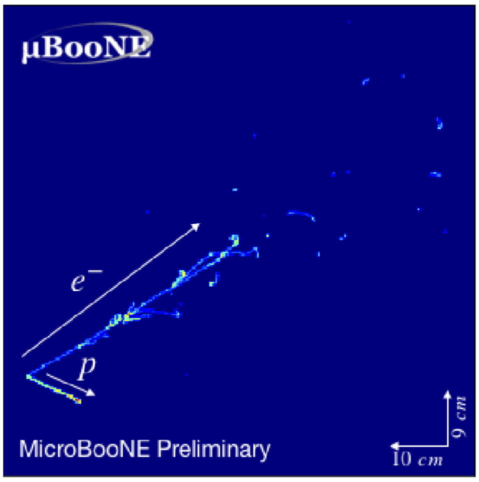

FIGURE 3.3 – Example of multiple PID. The proton track has high energy deposition at the end, while the electron track shows multiple scatterings. Taken from[84].

PID relies on several factors:

- **Signal collection and track reconstruction.** Drift time and wire position provide a 3D map of ionization trails. *Tracks* (from muons and protons) and *showers* (from electrons and photons) are identified accordingly.

- **dQ/dx, dE/dx data and pattern recognition.** Particles lose energy as they ionize LAr, and dE/dx helps identify the type of particle. Electrons and photons typically produce electromagnetic showers, while protons exhibit a Bragg peak at the end of their tracks. Muons leave straight tracks with relatively constant dE/dx, and pions may produce similar tracks but can also display an interaction vertex-like pattern at the end of the track.

- **Momentum estimation.** Momentum estimates help distinguish between heavier particles like protons and lighter particles like muons or pions. For particles stopping in the detector, their range is used to estimate momentum, while exiting particles' momentum is inferred from Coulomb scattering.

- **Vertex analysis.** Interaction vertices, such as those from neutrino interactions or pion decays, help classify outgoing tracks or showers.

3.5 Deep Underground Neutrino Experiment - DUNE

The Deep Underground Neutrino Experiment (DUNE) is currently under construction at by its international collaboration. Its main goal is to study the neutrino oscillation parameters, determine mass ordering, and the CP violation phase in the leptonic sector. DUNE will also be a world-class astrophysics neutrino observatory and nucleon decay detector[67] [66] [85].

The experiment will consist of two sites (see fig. 3.4): The Far Detector (FD), with a 40 k-ton fiducial mass, divided into four modules, will be built about 1.5 km underground at the Sanford Underground Research Facility (SURF) in South Dakota, USA, 1300 km from Fermilab. A Near Detector (ND) will be located at Fermilab in Illinois, 574 m from its intense neutrino beam production. Both FD and ND will be aligned to the neutrino beam line[67].

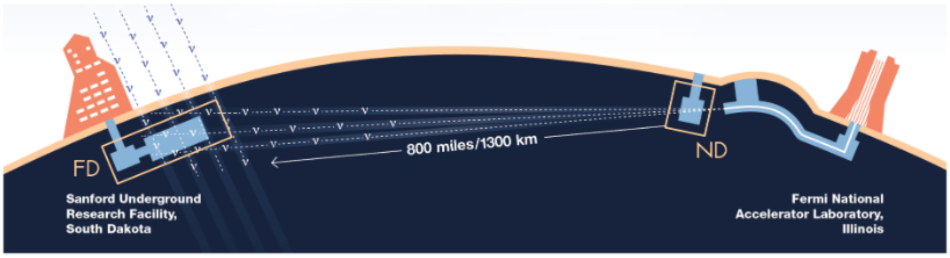

FIGURE 3.4 – The DUNE experimental setup overview. Taken from[85]. It is mainly composed of a Near Detector (ND), placed at 574 m from the neutrino beam production, and a Far Detector (FD), located in South Dakota, 1300 km from Fermilab.

The DUNE beam will be composed by ν_μ or $\bar{\nu}_\mu$. The DUNE Physics program is:

- **Primary science goals**
    - Measurement of Δm^2_{23} mass ordering, θ_{23} mixing angle, and its octant determination;
    - CP violation discovery (or exclusion) from the δ_{CP} phase measurement;
    - Measurement of the ν_e flux from a core-collapse supernova that should occur during DUNE lifetime. Such a measurement would provide information about the early stages of core-collapse and the possible signature of the birth of a black hole;
    - Proton decay searches in several modes. That would represent a key requirement of the Grand Unification of the Forces;
- **Ancillary physics goals**
    - Beyond Standard Model (BSM) searches with accelerator-based neutrino flavor experiments;
    - Neutrino oscillation measurements using atmospheric neutrinos;
    - Neutrino cross-sections and nuclear effects studies utilizing the ND;
    - Searches for DM, using a variety of signatures in ND, FD, and non-accelerator searches;

3.5.1 Near detector

The ND detector will be located 574 downstream from the target and will be composed of three detector components: *ArgonCube*; a high-pressure argon TPC (HpgTPC) within a magnet surrounded by an *electromagnetic calorimeter (ECAL)*, together called *Multi-Purposed Detector (MPD)*. Lastly, the third component is an on-axis beam monitor, the *System for on-Axis Neutrino Detection (SAND)*, that can move sideways up to 33 m off-axis of the beam, offering access to different neutrino energy spectra. This improvement in the degrees of freedom for the ND measurements is called DUNE Precision Reaction-Independent Spectrum Measurement (DUNE-PRISM). The details of the DUNE ND can be seen in figs. 3.5 and 3.6.

3.5.2 Far detector

The DUNE FD modules will be based on the TPC technology, each one contained on a cryostat of 17.5 kt of LAr, with 10 kt of fiducial mass/each. These modules will have dimensions of 18.9m(W) × 17.8m(H) × 65.8m(L) and internal dimensions of $14.0(W) \times 14.1(H) \times 62.0(L)$[56]
86 72 5
.

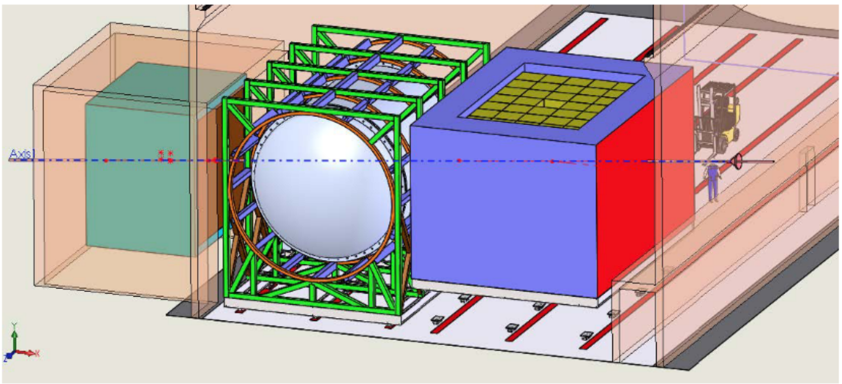

FIGURE 3.5 – Scheme of the DUNE ND components and the beam direction. The MPD is an on-axis configuration. Taken from[56].

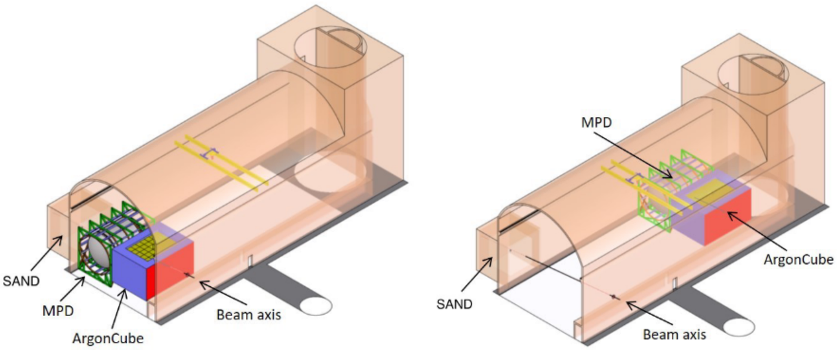

FIGURE 3.6 – Scheme of the DUNE ND hall and the on-axis (left) and off-axis (right) configuration. Taken from[56].

The FD module volumes of LAr are subjected to an electric field of $\varepsilon = 500$ V/cm and, as detailed in sec. 3.1 instrumented with three anode planes. As an example, fig. 3.7 shows the so called Horizontal Drift (HD) detector module. It will be composed of a total of 150 6 m × 2.3 m Anode Plane Assembly (APAs) arranged in 3 main vertical planes and 2 vertical cathodes. The cathode anode distance is ~ 3.6 m. The relative voltage between the layers is chosen to make the first two layers (U and V) transparent to the drifting electrons, and then, the last layer (X) collects the drifting electrons. The other modules will have different detection technology arrangements.

In the FD detectors, the measurement can be done by looking for the disappearance or appearance of a neutrino flavor of a beam through CC interactions. In this case, the interactions in LAr can happen through four possible reactions:

$$\nu_\mu + n \to p + \mu^-, \qquad \bar{\nu}_\mu + p \to n + \mu^+, \tag{3.5}$$

for survival and

$$\nu_e + n \to p + e^-, \qquad \bar{\nu}_e + p \to n + e^+, \tag{3.6}$$

for the appearance of neutrinos and antineutrinos.

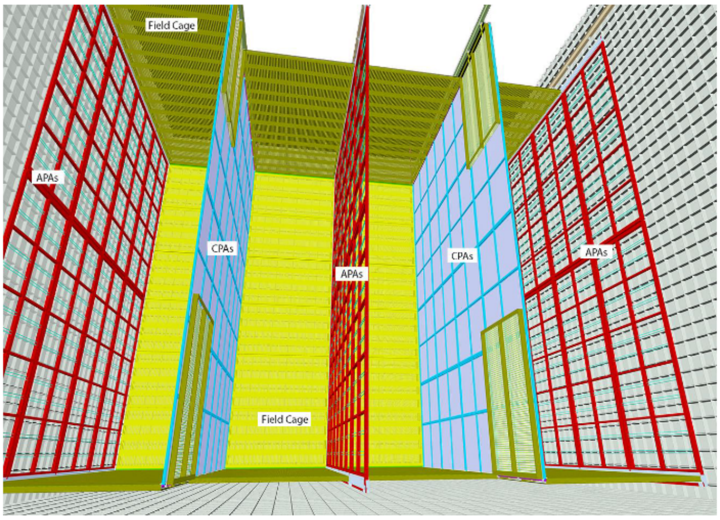

FIGURE 3.7 – The arrangement of the elements in the HD TPC. Two rows of cathode plane assemblies are interleaved with three rows of anode plane assemblies inside the field cage. Taken from[3].

Figure 3.8a shows the oscillation probability $\nu_\mu \rightarrow \nu_e$ as a function of the neutrino energy in GeV. The colored curves represent the δ_{CP} phase angles and their influence on the oscillations. Figure 3.8b represents the oscillation probability for $\bar{\nu}_\mu \rightarrow \bar{\nu}_e$, as a function of the neutrino energy, under $\delta_{CP} = -\pi/2, 0$, and $\pi/2$ (colored curves). These plots also indicate that energy must be measured with great precision in DUNE to allow the determination of the physics parameters of interest accordingly. The use of PDS measurements can help in the further improvement of energy determination, which can have a positive impact on physics measurements.

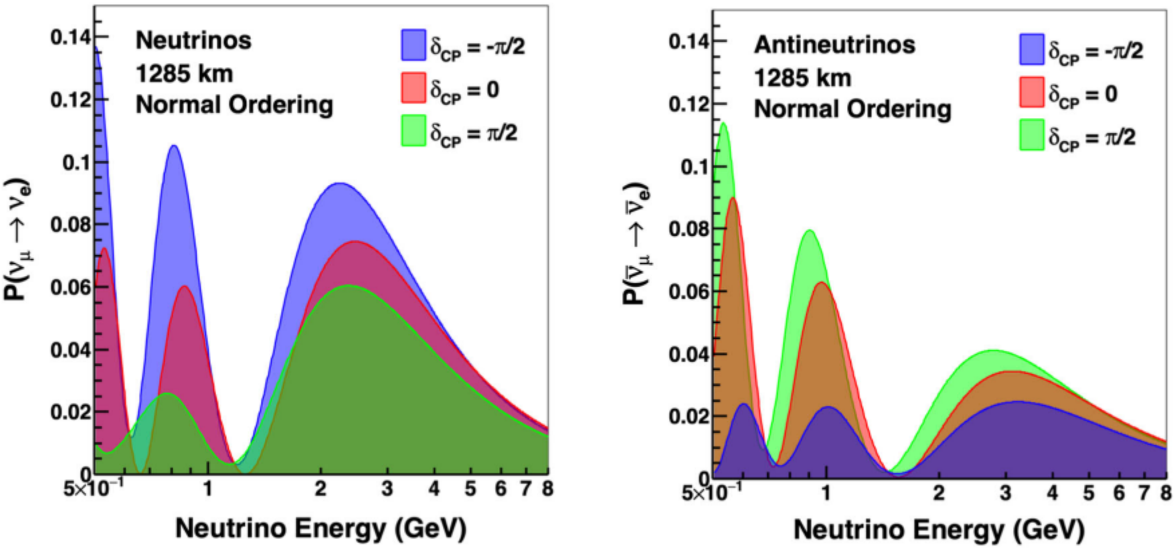

(a) $P(\nu_\mu \rightarrow \nu_e)$ oscillation probability under $\delta_{CP} = -\pi/2, 0$, and $\pi/2$.

(b) $P(\bar{\nu}_\mu \rightarrow \bar{\nu}_e)$ oscillation probability under $\delta_{CP} = -\pi/2, 0$, and $\pi/2$.

FIGURE 3.8 – Oscillation probabilities for neutrino (left) and antineutrino (right) transitions under different δ_{CP} phases. Taken from[87].

The beam that will be utilized in the experiment is provided by the Proton Improvement Plan-II (PIP-II) which consists of a proton beam that will work at 1.2 MW, correspondent to

1.1×10^{21} Protons-On-Target (POT) per year, assuming a combined uptime and efficiency of the Fermilab accelerator complex and the Long-Baseline Neutrino Facility (LBNF) beamline of 56%. It is assumed that the beam power will be upgraded to 2.4 MW by 2030[66] [56].

3.5.3 Photo Detection System

The scintillation photons are detected in PD modules, which for at least 2 modules of the far detector that will be XAs. These are light traps that employ a two stage wavelength arrange with a dicroic filter (fig 3.9). For the HD modules, the PDs and its cold electronics will be integrated into the APAs[87] [74] [56].

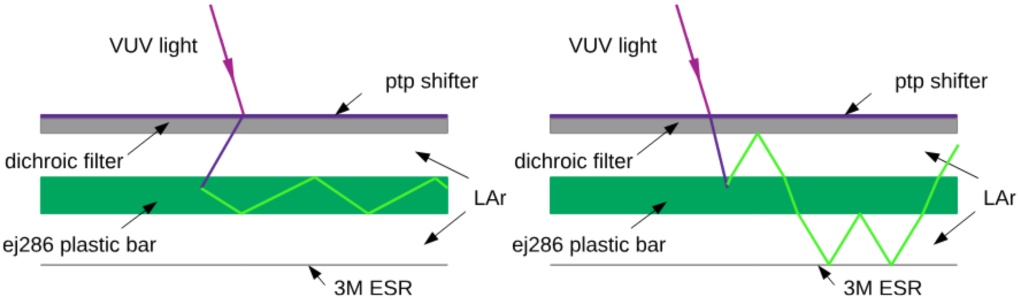

FIGURE 3.9 – The XA concept scheme. Taken from[82]. The photon enters in the XA and it is trapped, reflecting it to the SiPM that collects the signal.

Even in LAr with very high purity, signal degradation can occur along the very long drift distances in DUNE. Correcting the energy response is therefore necessary and is possible by knowing the t_0, which results in the resolution improvement. As previously mentioned this quantity is provided by the PDS. Another important task of the PDS is to trigger on non-beam events with incoming particles energy ranging from 10 MeV up to tens of GeV. Examples of such studies are the detection of core collapse supernova, searches for nucleon decays and oscillation of neutrino from atmospheric showers.

4 Liquid Argon Time Projection Chambers experiments

The following sections will outline the main characteristics of the experiments analyzed in this work. Some of these experiments, such as those conducted by Doke *et al.*[88] [89] [90] [73] [91] [6], utilized both LAr and liquid xenon (LXe). However, this work focuses on the study of light and charge production in LAr. The measurement graphs presented in this chapter provide the original context for the experimental data employed in this research and illustrate how the data were initially fitted as reported in their first publications.

4.1 Datasets for LArQL Global Fit

In this section will be described the experiments from where the data analyzed in this work was taken. The datasets from [5] [7] and [6] were originally used in ref.[4] work, which served as a comparison reference for the development of this research, which used light and charge data from Electron Recoils (ER). For further details, see ch. 5.

4.1.1 ICARUS project

The Imaging Cosmic And Rare Underground Signals (ICARUS) experiment was a scientific collaboration that used LArTPCs to detect and analyze neutrino interactions (including studies on neutrino oscillations). It also searches for rare physics events and studies CRs. This section discusses two early versions: the *ICARUS 3-ton* and the *T600*[92] [5].

4.1.1.1 Experimental apparatus

The ICARUS detector (fig. 4.1) has been installed at different locations for data taken, initially at the Gran Sasso National Laboratory (LNGS) in Italy[5] [92] [93].

The *ICARUS 3-ton* small-scale prototype collected data from CR and radioactive sources. The apparatus had two perpendicular wire planes with 2 mm spacing. The charge collection

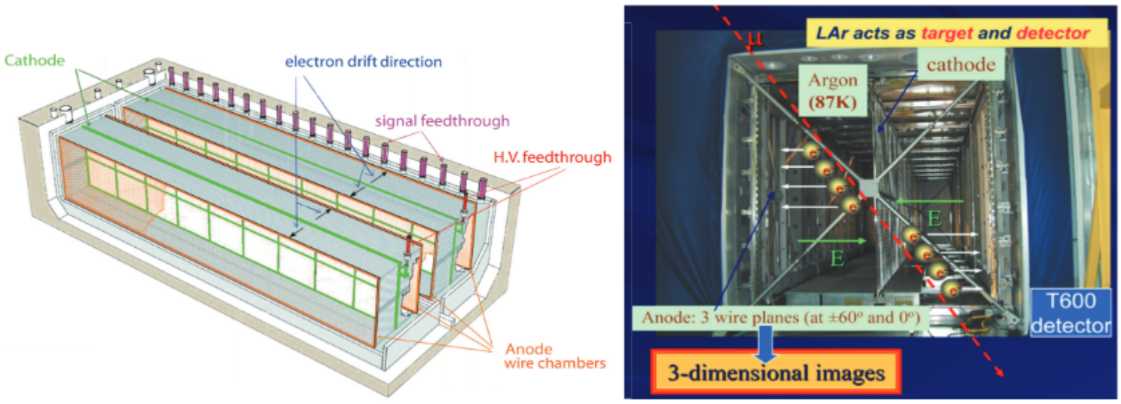

FIGURE 4.1 – Scheme of the detector on the left and a representation of the working principle of the ICARUS TPC on the right. Taken from[92].

from muons and proton tracks were analyzed under $\varepsilon = 200$, 350, and 500 V/cm. The dependence of the charge collection factor R with dE/dx was determined, covering energies from mip (Minimum Ionizing Particle) to approximately 30 MeV.

The full detector ICARUS T600 was composed of a large cryostat divided into two identical, adjacent half-modules with an overall volume of about 760 t of LAr (see fig. 4.1). Each module, with internal dimensions of $3.6 \times 3.9 \times 19.6\,\mathrm{m}^3$, had two TPCs separated by a common cathode, with the modules consisting of three wire planes. A nominal electric field of $\varepsilon_D = 500$ V/cm was applied, where the scintillation light detection was crucial for determining the t_0 of the events and the trigger signal. The PMTs operate with TPB as a WS[92] [5].

The data from these experiments provided precise determination from the parameters of the Birks's model[5]. This model is relevant to the discussion in ch. 5.

4.1.1.2 Experimental data

The Birks' law described the recombination factor $\mathscr{R}$, with parameters fitted to the data. This model showed good estimations in low-field regions when an additional parameter was included. The $\mathscr{R}$, according to the Birks' Law, is:

$$\mathscr{R} = \frac{Q}{Q_\infty} = \frac{A_B}{1 + k_B \frac{\frac{dE}{dx}}{\varepsilon}}, \tag{4.1}$$

where A_B was a normalization parameter in the model, and k_B is a constant. Notice for $\varepsilon \to \infty$, $Q \to Q_\infty$. The original measurements graphs for $\mathscr{R}(\varepsilon, dE/dx)$ can be seen in figs. 4.2. The experimental values obtained for A_B and k_B parameters are shown in tab. 4.1. Do not mistake the collected charge factor R and the recombination factor $\mathscr{R}$. The collected charge factor R is the ratio between the charge extracted by the ε field and the total charge produced. The recombination factor $\mathscr{R}$ is given by the ratio between the charge that recombines with the ions and the total charge produced.

TABLE 4.1 – Summary of fitted Birks parameters. The fit to Scalettar et al.[9] data was limited to $\varepsilon \leq 5\,\text{kV/cm}$ to allow for comparison with ICARUS data. Taken from[5].

Dataset	Particle	Range of ε (kV/cm)	A_B	k_B (kV/cm)(g/cm^{2}MeV)
3-ton	μ, p	$0.25-0.5$	0.8 ± 0.003	0.0486 ± 0.0006
T600	μ	0.5	0.81 ± 0.05	0.055 ± 0.005
Scalettar *et al.*	364 keV e^-	$0.075-1.5$	0.83 ± 0.01	-

The ICARUS experiment obtained parameter values of $A_B = 0.8 \pm 0.003$ and $k_B = 0.0486 \pm 0.0006\,(\text{kV/cm})(\text{g/cm}^2)/\text{MeV}$. The $\mathscr{R}$ datasets from[9] and[8] were also analyzed in this work.

4.1.2 Doke *et al.*

The experimental papers of Doke *et al.*. were published between 1981 and 2002 and compiled scintillation data for various particles in LAr and liquid xenon (LXe). The focus in this section will be on the results in LAr[88] [73] [89] [6]. These studies discuss how dE/dx affects decay times and scintillation yield in LAr under different types of excitation, such as e^-, $\alpha-$ particles, and fission fragments.

The scintillation measurements were made with ionizing particles from radioactive sources and accelerators with an energy range of 20–40 MeV. A liquid WS Dimethyl-POPOP converted the scintillation and was detected by PMTs that measured the t_0[90] [89] [6].

4.1.2.1 Experimental data

From these works dedicated to the measurement of scintillation light the energies to produce an e$^-$-ion pair (W_{ion}) and a VUV photon (W_{ph}) were determined and correlated as:

$$W_{ph} = \frac{W_{ion}}{\left(1 + \frac{N_{ex}}{N_{ion}}\right)}. \tag{4.2}$$

Other fundamental findings were related to the fast and slow components' behavior. For instance, as mentioned in sec. 3.2.1.1, the fast component has a decay of approximately 7 ns. The decay times were found to be independent of dE/dx, which indicated that the quenching observed at higher densities does not affected the decay rates of Ar excimers.

Another important information from these studies was an indication for the existence of escaping electrons at $\varepsilon \sim 0$ that do not recombine, resulting at a reduced light yield for certain values of dE/dx. Figure 4.3 shows this trend for the relative light yield as dE/dx values reduce.

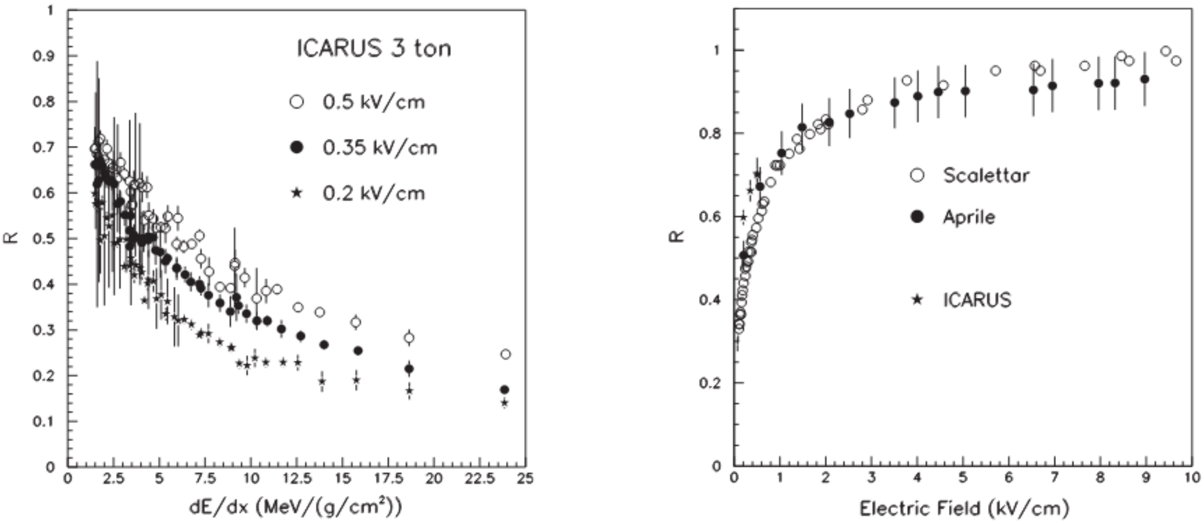

(a) The $\mathscr{R}$ measured with the ICARUS 3-ton prototype as a function of dE/dx[5].

(b) The $\mathscr{R}$ as a function of the electric field for 364[9] and 976 keV[8] electrons, and for m.i.p. in ICARUS TPC[5]. The errors in ref.[9] were smaller than the symbol size.

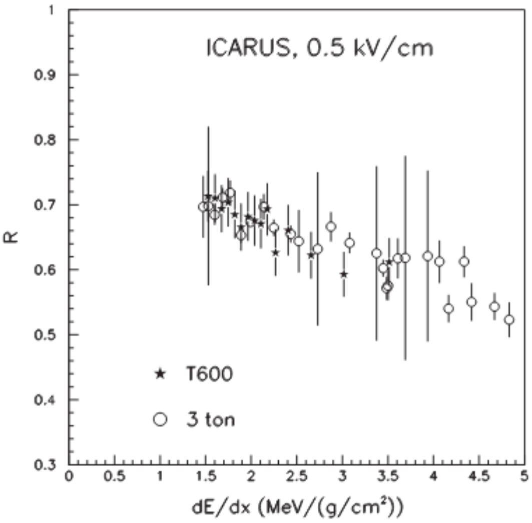

(c) The $\mathscr{R}$ of ICARUS T600 and 3-ton detectors at 500 V/cm as a function of dE/dx. The errors for T600 data include a 5% systematic uncertainty[5].

FIGURE 4.2 – Measurements of $\mathscr{R}$ in ICARUS experiments: (a) $\mathscr{R}$ vs dE/dx for the 3-ton prototype; (b) $\mathscr{R}$ vs electric field for different energy electrons and m.i.p. (c) Comparison of $\mathscr{R}$ vs dE/dx for T600 and 3-ton detectors at 500 V/cm. Taken from[5].

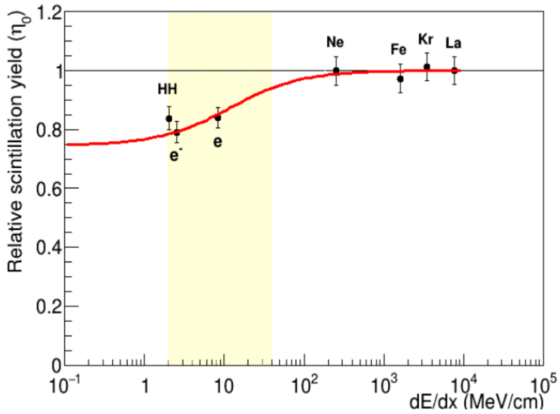

FIGURE 4.3 – Relative light yield at $\varepsilon = 0$ as function of dE/dx. Reproduced from[4] based on data from[6].

4.1.3 ARIS experiment

The Argon Response to Ionization and Scintillation (ARIS) experiment was designed to investigate LAr's response to nuclear recoils (NR) and ER. The experiment is capable of measuring NR down to approximately 2 keV$_{ee}$ (ee = electron equivalent)[7].

4.1.3.1 Experimental apparatus

The DP-TPC was in a stainless steel dewar and was mounted 1 m away from the LICORNE neutron production target at the ALTO facility in Orsay, France (see fig. 4.4a). It has a $\sim$ 0.5kg active mass and a PTFE inner surface with an enhanced specular reflector film for increased light reflection. The ε field was generated by two fused silica windows placed at the end of the cylindrical volume, coated with indium tin oxide (see fig. 4.4b)[7] [94].

The ionization can be compared to S_1 signals with/without the electric field applied. The WS utilized was TPB. These scintillation photons were detected by one 3-inch R11065 PMT below the cathode and seven 1-in R8520 PMT above the anode. These detectors are represented in fig. 4.4a as A0, A1, A2, A3, A4, A5, A6 and A7. For the S_1 data, the t_0 can be reduced to $\sim$ 10 μs from hundreds of ms, because of the drift field that can reduce the drift time. The TPC response to light was calibrated with ^{241}Am and ^{133}Ba γ sources located outside surface of the dewar (see fig. 4.4a). The energies of the sources were 59.5 keV $\rightarrow {}^{241}$Am and 81.0 to 383.8 keV $\rightarrow {}^{133}$Ba[7].

4.1.3.2 Experimental data

The measurements were performed with multiple sources, such as the ^{83m}Kr and γ sources at the Compton scattering regime (see fig. 4.5a). The Light Yield (L) response for ER at null fields were not affected by the quenching effects, depending on the energy, meaning that L was

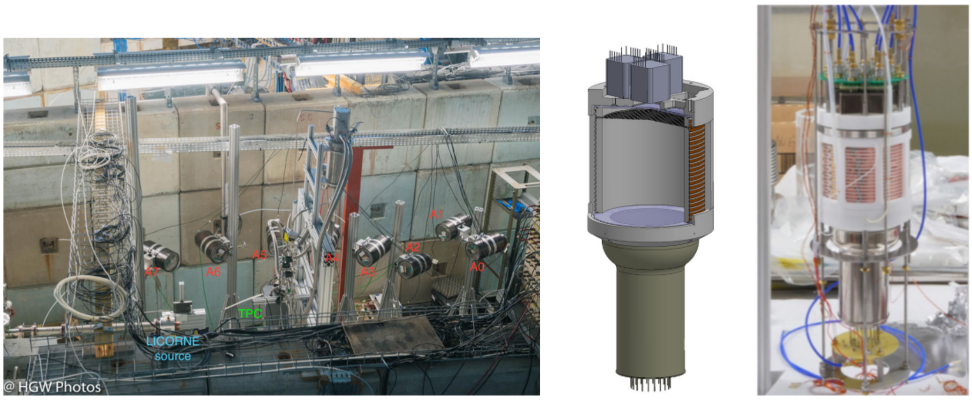

(a) ARIS setup.

(b) ARIS TPC. Scheme and photography.

FIGURE 4.4 – In (a) The TPC (green letters) was placed between the eight scintillation detectors: A0, A1, A2, A3, A4, A5, A6, and A7 (in red) and in the neutron beamline (indicated in blue). In (b) Design and picture of the TPC. Figures taken from[7].

proportional to the dE/dx. The evaluated L values were within a 5% between 41.5 keV and 300 keV as can be seen in 4.5.

The S_1 signal varies depending on the electric field strength, whereas this work goes from 0 to 500 $\mathrm{V/cm}$[7]. The ration $S_1/S_1(\varepsilon = 0)$ dependence on the energy can be seen in fig. 4.5.

The measurements of the light yield $S(E_{ee}, \varepsilon)$ (E_{ee} = Electron Equivalent Energy) were fitted through the expression:

$$S(E_{ee}, \varepsilon) = \frac{S_1(\varepsilon)}{S_1(\varepsilon = 0)} \quad = \frac{\alpha + \mathscr{R}(E_{ee}, \varepsilon)}{1 + \alpha}, \tag{4.3}$$

where $\alpha = N_{ex}/N_{ion} = 0.21$ and the fraction $\mathscr{R}$ of charge that recombines was estimated using the Doke-Birks model[89] [7] [95], that is used for ER in low-energy limits:

$$\mathscr{R}(E_{ee}, \varepsilon) = \frac{A\frac{dE}{dx}}{1 + \frac{A}{(1-C)}\frac{dE}{dx}} + C, \tag{4.4}$$

with:

$$C = C' e^{-D\varepsilon}. \tag{4.5}$$

All parameters are real constants and the values returned by the fit were $A = (2.5 \pm 0.2) \times 10^{-3}$ cm/MeV, $\mathrm{C}' = 0.77 \pm 0.01$, and $D = (3.5 \pm 0.3) \times 10^{-3}$ cm/V[7].

The S_1 signal changes as a function of ε and dE/dx due to the quenching that suppresses it. The ARIS data describes how LAr detectors respond to different particle interactions under the influence of several electric fields values, especially evolving the linear response of LAr scintillation to ERs.

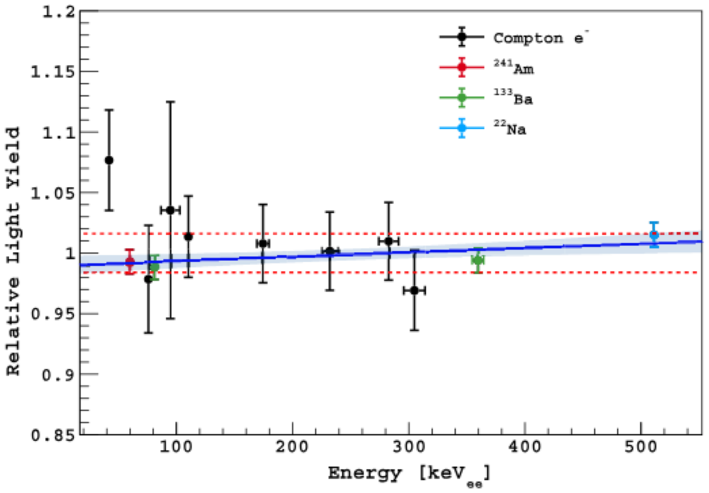

(a) The L, concerning the mean value of the eight ND measurements, as a function of the Compton e^- energy from ^{7}Li* deexcitation and from ^{241}Am(59.5 keV), ^{133}Ba(81 and 356 keV), and ^{22}Na(511 keV)γ sources.

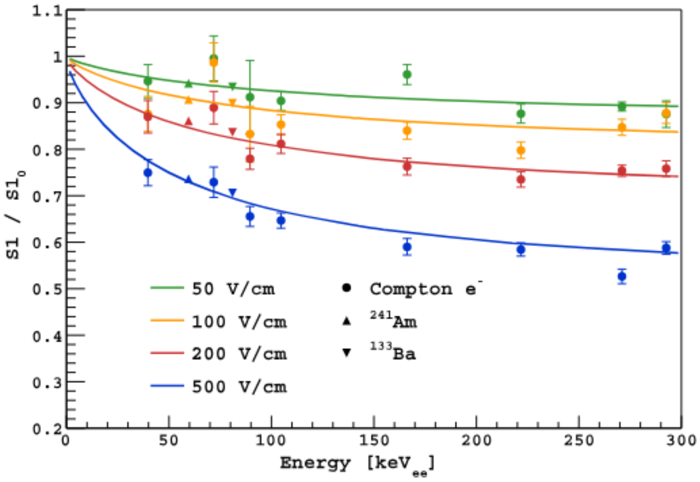

(b) Scintillation $S_1/S_1(0)$ at different drift fields, fit with eq. 4.3.

FIGURE 4.5 – Comparison of scintillation $S_1/S_1(0)$ at different drift fields and the L values as functions of the Compton e^- energy and energy sources. Figures taken from[7].

4.2 Datasets for LArQL model comparison

A dedicated literature research for more experimental datasets was developed and is presented in this section. These are later used in chapter 6 for direct comparisons with predictions of the LArQL model.

4.2.1 MicroBooNE

The Micro Booster Neutrino Experiment (μBooNE or MicroBooNE) detector was the first LArTPC-SP in the Short-Baseline Neutrino (SBN) program to be operational. It was built to observe interactions of neutrinos from the on-axis Booster Neutrino Beam (BNB) and off-axis

Neutrinos at the Main Injector (NuMI) beams at FERMILAB in Batavia, IL, located approximately 470 m from the neutrino production target[96] [97] [98] [99].

4.2.1.1 Experimental apparatus

The MicroBooNE is with a LArTPC with 170 t of active volume with dimensions $2.56 \times 2.33 \times 10.36$ m^3, that works on an electric field of 0.273 kV/cm leading to a drift velocity of 0.11 cm/μs. The drifted charge derived from particle interactions is read in three planes with a wire pitch of 3 mm. The scintillation photons are detected by 32 HAMAMATSU R5912-02MOD PMTs coated with TPB[97] [72]. The scheme of the detector can be seen in figure 4.6a.

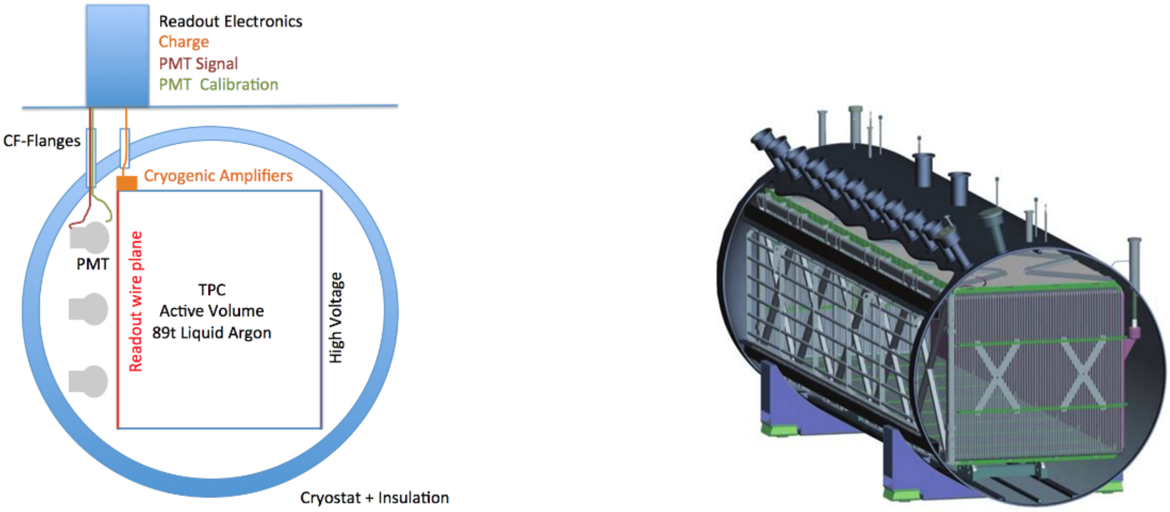

(a) Frontal scheme of the MicroBooNE detector. Figure taken from[97].

(b) Scheme of the MicroBooNE detector in a diagonal perspective. Figure taken from[100].

FIGURE 4.6 – Combined schemes of the MicroBooNE detector. The 89 t active volume is housed by a cryostat where wires read out the charge produced by particle interactions. Scintillation light is recorded with PMTs, and the readout electronics are placed outside the vessel.

For calibration, a set of steps were made in this experiment. First, the time-dependence and the position of the detector response to the ionization charge were corrected with crossing CR muons. Figure 4.7a illustrates an example of CR muon. The second step consisted of converting the dQ/dx to dE/dx using stopping muons from neutrino interactions; in other words, the stopping muons were produced in CC interactions that decayed inside the detector with a Bragg peak in the detector. This step is the dE/dx calibration. The final step consisted of a refinement of the relation between the measured charge and the dE/dx for highly-ionizing particles, which used the stopping protons from neutrino interactions. For examples of the PID achieved after these steps, see fig. 4.7.

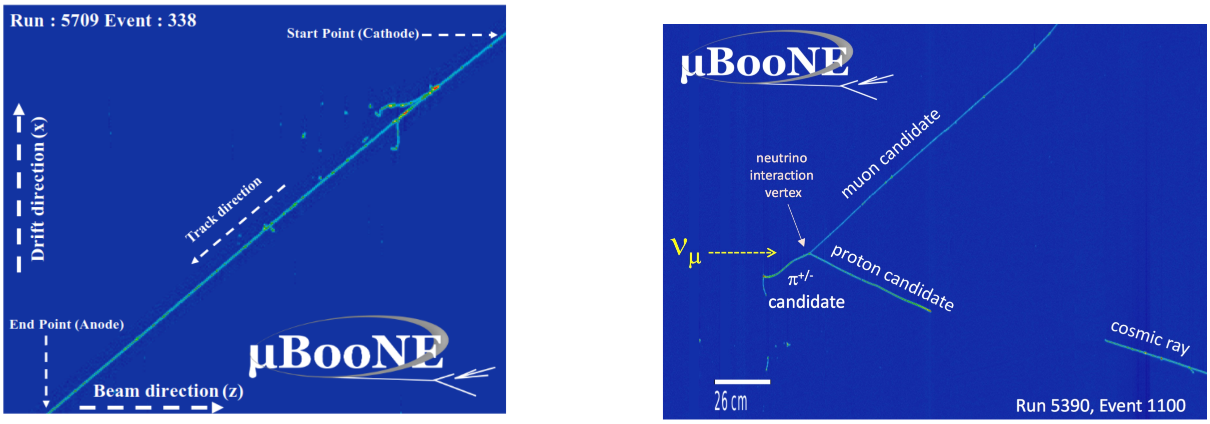

(a) Example of an event of anode-cathode crossing CR. Figure taken from[72].

(b) Event display of a three-track neutrino event with a muon, a charged pion, and a proton candidate in the final state. Figure taken from[101].

FIGURE 4.7 – Examples from the MicroBooNE detector: (a) anode-cathode crossing CR, and (b) candidate neutrino interaction displaying electromagnetic activity.

4.2.1.2 Experimental data

Calibration studies of charge production through the dQ/dx quantity and its dependence on dE/dx were developed. According to the Birks formula presented in section 4.1.1 their relationship can be expressed as follows[72]:

$$\frac{dQ}{dx} = \frac{A_B}{W_{ion}} \left(\frac{\frac{dE}{dx}}{1 + \frac{k_B}{\rho \varepsilon} \frac{dE}{dx}} \right), \tag{4.6}$$

which employed to enable the comparison between dQ/dx and dE/dx. Both quantities dQ/dx and dE/dx were measured for each event analyzed and displayed in a two dimensional histogram as shown in fig 4.8 and the data was compared to equation 4.6 using both the proposed set of parameters from [5] and a fitted version to the histogram.

In conclusion, MicroBooNE used CR to remove the temporal and spatial variations in the detector response, stopping muons to determine the absolute dE/dx for m.i.p., stopping protons to refine dQ/dx correlation with dE/dx[102], represented by fig. 4.8.

4.2.2 ANKOK prototype

The ANKOK experiment was a direct DM search experiment using argon. This experiment aims to detect WIMPs with masses of around $\approx 10\,\mathrm{GeV/c^2}$ and has as one of its main goals the design and construction of a high-sensitivity detector for low-mass WIMPs. The LArTPC (Waseda Liquid Argon test stand) was located at the Nishi-Waseda campus of Waseda University in Tokyo, Japan, and focuses on ER and NR discrimination of S_1/S_2 under higher drift fields. In the present section, we focus on the ANKOK prototype, which consists of a DP-

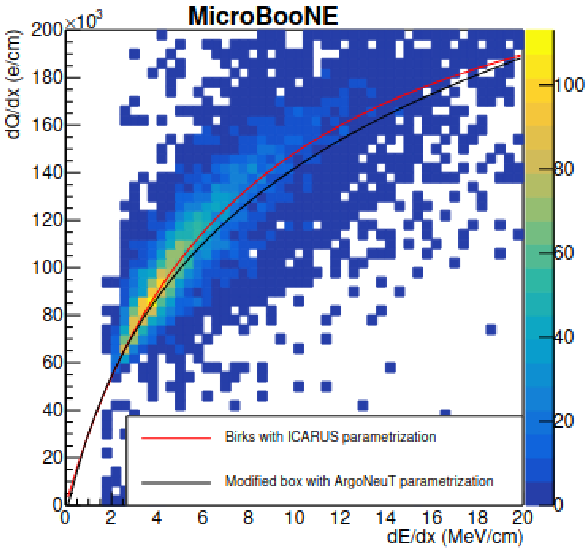

FIGURE 4.8 – The dQ/dx in the function of the $(dE/dx)_{range}$ distribution with the 4.6 (in black) and 4.6 (in red) models plotted in comparison, for proton tracks and an electric field of 0.273 kV/cm and with the ICARUS and ArgoNeuT parameters. The color scale next to the graph represents the frequency distribution of the $dQ/dx(dE/dx_{range})$. Figure taken from[72].

LArTPC, its Research and Development (R&D), and data published in 2018[10].

4.2.2.1 Experimental Apparatus

The detector (see 4.9) consists of a DP-TPC with an active volume of $\approx 0.5\,\text{kg}$ and dimensions $\phi = 6.4\,\text{cm} \times H = 10\,\text{cm}$, composed of PTFE, with electrodes made of indium-tin-oxide (ITO) and a wire grid plane (stainless steel wire with a diameter of $100\,\mu$m and pitch of 4 mm). Two HAMAMATSU R11065 PMTs located at the top and bottom of the detector and are coated with TPB as WS (128 nm to 420 nm). The circuit generates high voltage to vary the ε from 0 to 3.0 kV/cm, with a maximum of 30 kV in LAr.

The potential difference between the anode and the wire was 4.5 kV, resulting in extraction and S_2 emission fields of 3.6 kV/cm in LAr and 5.4 kV/cm in GAr. The sources used for γ-ray and neutron calibration were ^{22}Na and ^{252}Cf, respectively. An NaI(TI) scintillator behind the source detects the γ-ray and estimates the TOF[10]. Figure 4.9 provides details of the TPC.

4.2.2.2 Experimental data

The data acquisition system consists of a 250 MS/s flash ADC and a three-channel coincidence trigger for the top, bottom, and NaI(TI) scintillator. The S_1 was of $5.7 \pm 0.3\,\text{p.e./ keV}_{\text{ee}}$ for 511 keV γ-ray at $\varepsilon = 0$ V/cm. The S_1 decreases and S_2 increases at higher fields due to the $\mathscr{R}$. The fig. 4.10 illustrates the behavior of S_1 and S_2.

For ER, recombination $\mathscr{R}$ was calculated using the Doke-Birks model. The data is fitted

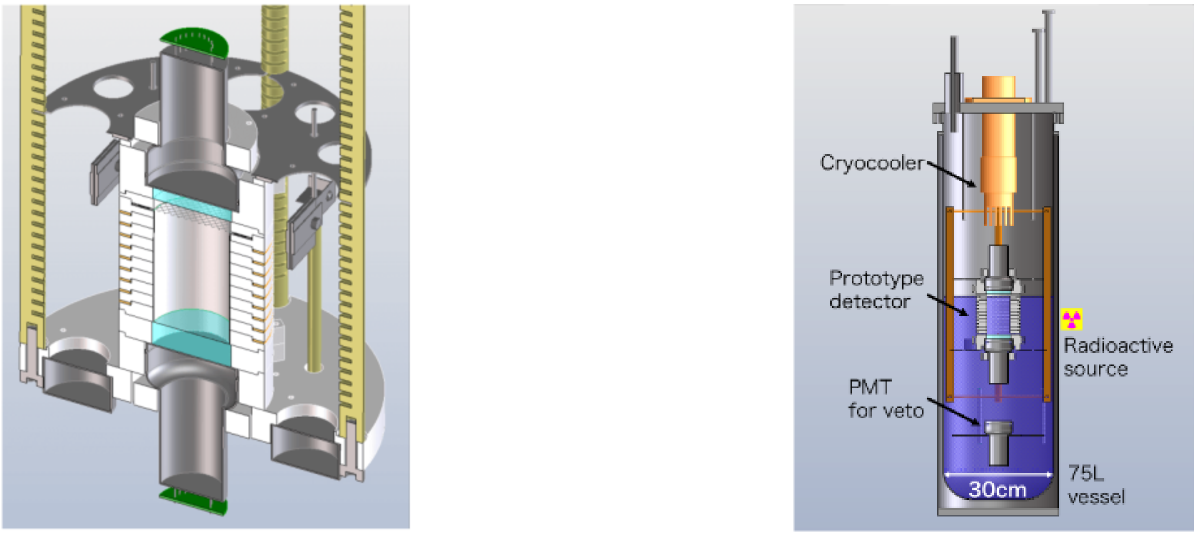

(a) TPC scheme with liquid/gaseous volume division phase. Figure taken from[10].

(b) The full-apparatus scheme. Figure taken from[103].

FIGURE 4.9 – Cross-section schemes of the TPC from different angles.

using the eq 4.7:

$$\frac{S_1(\varepsilon)}{S_1(\varepsilon_{min}=0)} = 1 - C_1 \cdot (1-\mathscr{R}(\varepsilon)) \quad \text{and} \quad \frac{S_2(\varepsilon)}{S_2(\varepsilon_{max}=3)} = C_2 \cdot (1-\mathscr{R}(\varepsilon)), \tag{4.7}$$

where C_1 and C_2 are constants.

In conclusion, the ANKOK prototype evaluated ER discrimination power using a small TPC with ^{22}Na and ^{252}Cf sources. The ANKOK experiment gathered data for both NR and ER. The S_2/S_1 ratio for low-energy events in LArTPCs was used to analyze drift electric field impacts on ER discrimination[104] [10].

4.2.3 ReD experiment

The Recoil Directionality (ReD) experiment was part of the DarkSide Collaboration that investigates the directional sensitivity of Ar detectors via columnar $\mathscr{R}$ to NRs in the E range of $20-200$ keV$_{nr}$ for direct DM searches, collecting data for both NR and ER[7] [11].

4.2.3.1 Experimental apparatus

The apparatus (see fig 4.11) consists of a DP-LArTPC with an active mass of 185 g (if filled with LAr) with dimensions 5 cm × 5 cm × 6 cm(L × W × H). It was delimited by two acrylic windows with 4.5 mm. The top and bottom windows were covered by a transparent conductive layer of ITO. The extraction grid was made of stainless steel 50μm thick. This apparatus can work both as a SP or DP TPC. For the GAr production, the TPC works with a

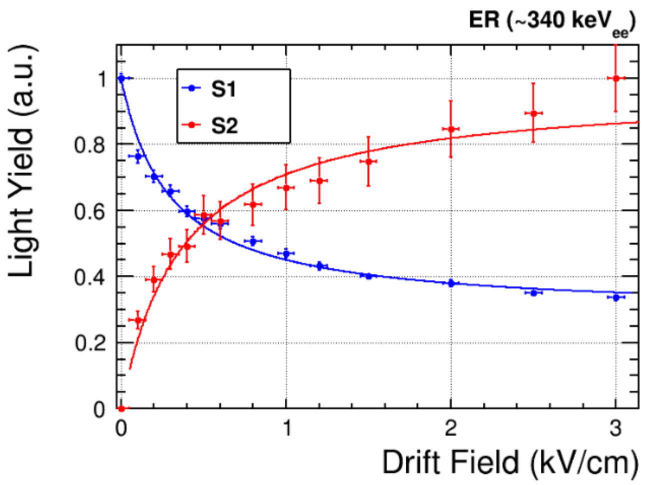

1

FIGURE 4.10 – Dependence of S_1 yield (in blue) and S_2 yield (in red) for ER events at 340 keV$_{ee}$, normalized at 3 kV/cm. Figure taken from[10].

boiler consisting of a platinum resistance temperature sensor. For detecting the light response, 24 Silicon Photomultipliers (SiPMs) were placed on top of the TPC, composing the readout system[11].

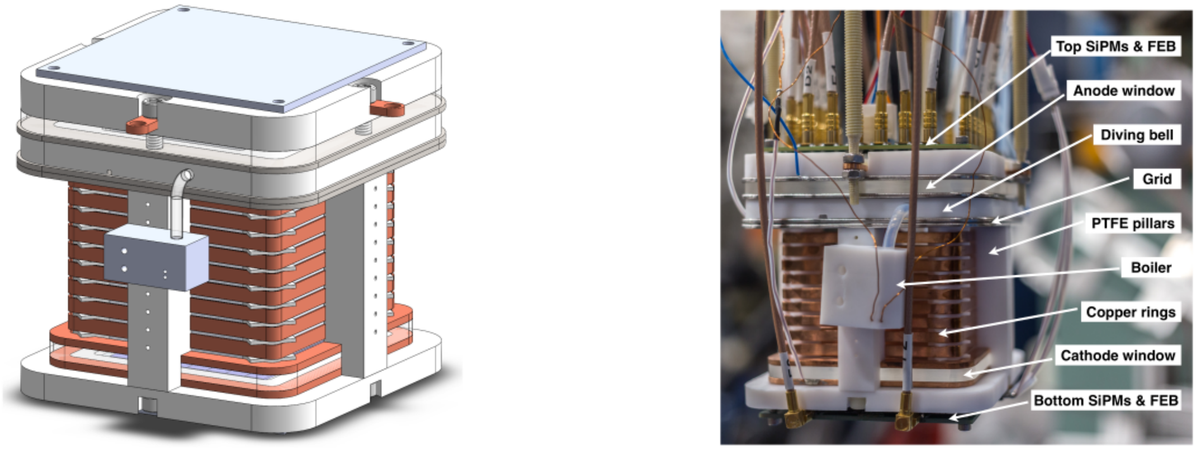

(a) Schematic drawing.

(b) A photograph with the components of the TPC.

FIGURE 4.11 – The ReD TPC. Taken from[11].

4.2.3.2 Experimental data

The measurements of scintillation and ionization were estimated using the models that will be described as follows. The total S_1 and S_2 signals:

$$S_1 = g_1 N_{photons} = g_1\left(\frac{N_{ex}}{N_{ion}} + \mathscr{R}\right)N_{ion} \tag{4.8}$$

and

$$S_2 = g_2(1-\mathscr{R})N_{ion}, \tag{4.9}$$

with g_1 and g_2, the number of photoelectrons detected per scintillation photon emitted and the S_2 gain of the TPC, respectively.

The S_1 and S_2 were expected to be anticorrelated, because of their origin, from scintillation and ionization processes. Then, this work studied these quantities as a function of the deposited energy and the electric field.

For $\mathscr{R}$, the work used the Doke-Birks model, modified to this account for the observance of the dependence on ε_d expressed as

$$\mathscr{R} = \frac{Ae^{-D_1\varepsilon_d}\frac{dE}{dx}}{1+B\frac{dE}{dx}} + Ce^{-D_2\varepsilon_d}, \tag{4.10}$$

where the B constant can be defined as

$$B = \frac{Ae^{-D_1\varepsilon}}{\mathscr{R}\left(\frac{dE}{dx}\to\infty\right) - Ce^{-D_2\varepsilon_d}}, \tag{4.11}$$

considering $\mathscr{R}\to 1$ for highly-ionizing particles ($\frac{dE}{dx}\to\infty$) at any value of ε.

The $S_1/S_1(0)$ measurements were taken in the DP mode of the ReD TPC. The data taken with the ^{241}Am were used as control data and were not used in the fit, like the ^{83m}Kr and ^{133}Ba data, because the energy was out of the range of the eq. 4.10 ($9-32$ keV). However, these data were used to cross-check model predictions of the light yield, represented by fig. 4.12. The modeling of the experiment offered reliable estimates of scintillation and ionization, correlated to different dE/dx values and ε fields.

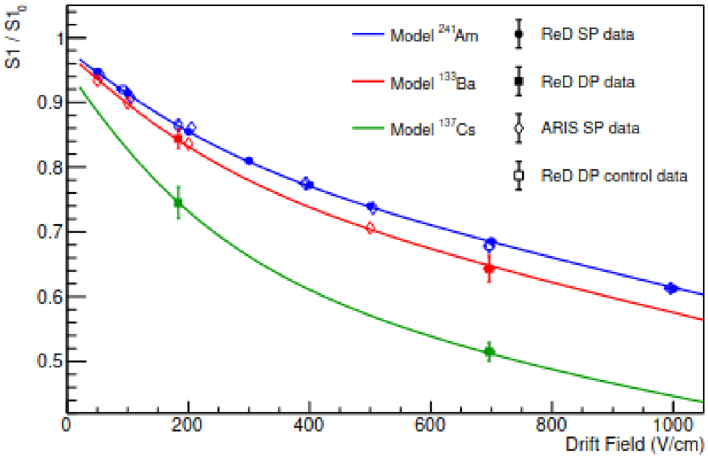

FIGURE 4.12 – The $S_1/S_1(0)$ ratio as a function of the electric field ε_d, from ReD SP and DP TPC measurements with ^{241}Am, ^{133}Ba, and ^{137}Cs sources. Data points from ARIS collaboration were available up to 500 V/cm. The ReD ^{241}Am DP data (blue empty squares) were not used in the fit. Figure taken from[11].

5 Analysis Description

In this chapter the implementation details of the statistical analysis adopted in the work presented in this dissertation are presented. In section 5.1 the LArQL model is described with its main features. In section 5.2 all the data sets organization and implementation of the proposed global fit are discussed.

5.1 The LArQL model

The PDS systems for the next massive LArTPCs experiments, as discussed in sec. 3.5, will have their capacity enhanced to exploit scintillation light detection. That requires an improved description of the scintillation light production mechanism, considering finer details regarding the energy deposits per particle in LAr volume. Recent scintillation data analysis performed in ProtoDUNE-SP, indicates the importance of detailed estimations for light and charge yields, considering the energy deposits per particle in LAr and the simulation for future LArTPCs experiments such as DUNE FD-VD and future DUNE Phase-II Detector modules[71 69 87].

The charges produced from ionization are drifted to anode planes allowing the reconstruction of trajectories (see ch. 3). In order to study the constrained production os scintillation light and ionization charges in LAr a simple phenomenological model is used (LArQL)[4]. It adjusts the Birks' model for charge yield in order to account for the role of escape electrons at lower electric fields but at the same time aligning the model with estimates at higher fields without losing its description quality. As one of its benefits, this model offers estimates at electric field ε values from 0 up to 0.75 kV/cm which was a feature previously limited on other models.

The LArQL model is implemented according to a set of assumptions based on experimental results. To estimate Q and L eq. 3.4 becomes:

$$Q_{LArQL}\left(\varepsilon, \frac{dE}{dx}\right) + L_{LArQL}\left(\varepsilon, \frac{dE}{dx}\right) = N_{ion} + N_{ex}, \tag{5.1}$$

implying they are anticorrelated and depend on dE/dx and ε, as represented by fig. 5.1. This model depends on the average number of produced quanta (N_q):

$$N_q = N_{ion} + N_{ex}, \tag{5.2}$$

and the number of ionization electrons generated per unit of deposited energy is $N_{ion} = 1/W_{ion}$ (dimensionless), where W_{ion} is the energy expended for each ionic separation:

$$W_{ion} = E_{ion} + E_{kin} + \left(\frac{N_{ex}}{N_{ion}} E_{ex}\right) = 23.6\ \pm 0.3\ \mathrm{eV/e^-}, \tag{5.3}$$

where E_{ion} is the average ionization energy, E_{kin} the average kinetic energy per electron, and E_{ex} is the energy released for each exciton formed and N_{ex} the excitations of Ar atoms, with $N_{ex}/N_{ion} = 0.29$ representing the number of excitons per electron-ion pair ionization in LAr[6] [4] [7] [105].

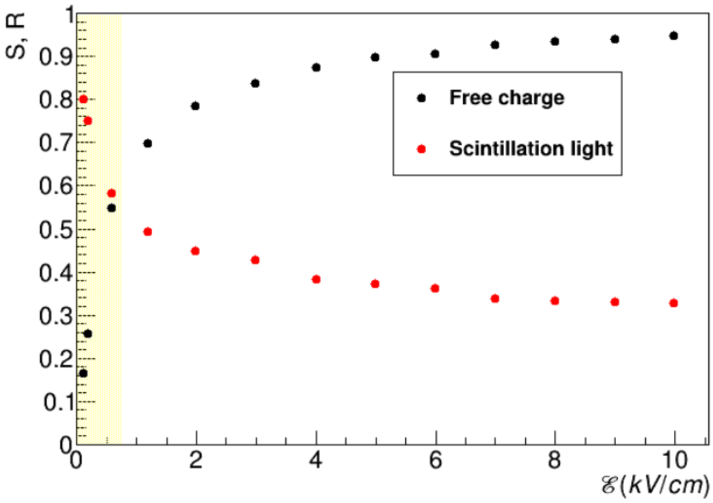

FIGURE 5.1 – The S and R ratios as ε applied in LAr, in kV/cm for *mip*. The yellow band represents the range of interest for LArQL. The red dots represent the scintillation light and the black dots, the free charges. The anti-correlation between the two quantities is mathematically described by 5.1. Figure taken from[6] [4].

The LAr ionization charge chain mechanisms and scintillation light production are represented by fig. 3.2. The fig. 5.1 shows the collection factor R, that is the ratio between the charge collected Q_{coll} at a fixed ε and the maximum charge produced (Q_∞):

$$R\left(\varepsilon, \frac{dE}{dx}\right) = \frac{Q_{coll}\left(\varepsilon, \frac{dE}{dx}\right)}{Q_\infty}. \tag{5.4}$$

S represents the scintillation ratio defined as:

$$S\left(\varepsilon, \frac{dE}{dx}\right) = \frac{L\left(\varepsilon, \frac{dE}{dx}\right)}{L\left(0, \frac{dE}{dx}\right)}, \tag{5.5}$$

where L at a null electric field is the maximum amount of light emitted for a fixed dE/dx.

It is also taken into account the light reduction at $\varepsilon = 0$ for low dE/dx values, attributed to the escaping electrons that do not recombine into Ar_2^* excimers and, as a consequence, reduce the amount of photons produced during the de-excitation of the Argon molecules. The Relative Scintillation Yield at $\varepsilon = 0$ (η_0, see fig. 4.3) is can be written as funcion of dE/dx as:

$$\eta_0 = \frac{1 - \chi_0 + \frac{N_{ex}}{N_{ion}}}{\left(1 + \frac{N_{ex}}{N_{ion}}\right)}, \tag{5.6}$$

where χ_0 represents the fraction of electrons escaping in $\varepsilon \approx 0$ (dimensionless) and contains the dE/dx dependence. It is parameterized in LArQL as:

$$\begin{aligned} \chi_0 &= \left(1 + \frac{N_{ex}}{N_{ion}}\right)(1 - \eta_0) \\ &= \frac{\chi_0 1}{\chi_0 2 + \exp\left(\chi_0 3 + \frac{dE}{dx}\rho_{LAr}\chi_0 4\right)}, \end{aligned} \tag{5.7}$$

where $\chi_0 i$ are fitted constants to the data from [6]. This quantity is used to provide the correction term for additional escaping electrons in lower fields, modifying the Birk's model for the range of interest of LArQL. The charge yield term assumes the form:

$$Q_{LArQL} = Q_{Birks} + Q_{ee}, \tag{5.8}$$

where Q_{LArQL} is the total productions of free charges, Q_{Birks} is the charge production due to the ε applied according to the Birks model and Q_{ee} refers to the charges that would escape even at $\varepsilon = 0$ [102 4]. Combining the eq. 5.8 and eq. 5.7 and introducing an electric field dependent cutoff factor:

$$Q_{LArQL} = \frac{\frac{A_B}{W_{ion}}}{1 + \frac{k_B}{\rho_{LAr}}\frac{1}{\varepsilon}\frac{dE}{dx}} + \chi_0 f_{corr} Q_\infty. \tag{5.9}$$

At $\varepsilon = 0$ and a given dE/dx, the fraction of escaping electrons is $Q_0 = \chi_0 Q_\infty$.

The f_{corr} factor generalizes the escaping electrons term the dependence for $\varepsilon \neq 0$ and is given by:

$$f_{corr} = e^{\overline{\left(\alpha \ln \frac{dE}{dx} + \beta\right)}^{\,-\varepsilon}}, \tag{5.10}$$

where α and β are free parameters[4]. Then, the L term is obtained as:

$$L_{LArQL} = N_{ion} - Q_{LArQL} + N_{ex}. \tag{5.11}$$

represents the production of light scintillation. The model is parameterized with eight constants, which were fitted in the global fit proposed in this work.

The table 5.1 shows the original parameters of the LArQL model that consists of two parameters from the Birks' model k_B and A_B, in eq. 5.9[102], four parameters for χ_0 represented by $\chi_0 1, \chi_0 2, \chi_0 3$ and $\chi_0 4$, present in eq. 5.7, and two free parameters from eq. 5.10.

TABLE 5.1 – Original parameter sets[102] [4] obtained with LArQL.

param.	k_B (g V/cm^3 MeV)	A_B	$\chi_0 1$	$\chi_0 2$	$\chi_0 3$	$\chi_0 4$ (MeV/cm)$^{-1}$	α (V/cm)	β (V/cm)
	48.6	0.8	3.65×10^{-03}	-5.46	1.70	1.94×10^{-04}	3.7×10^{-2}	1.2×10^{-2}

Comparisons of the LArQL model with experimental data from the works developed by[95] [5] and [6], point out to a satisfactory description at[4], as shown in figs. 5.2a, 5.2b and 5.2c. Such quantities as S and the $\mathscr{R}$ or recombination factor and dQ/dx, represented by fig. 5.3, the charge density are described simultaneously by LArQL.

However, it was observed that further improvements on the model could be achieved to optimize the estimations for the data. This approach can be improved in two ways, described in detail in subsequent sections:

- The performing a global statistical fit, weighted by the initially available datasets;
- The inclusion of new data available for more accurate estimates of model parameters;

5.2 Statistical analysis

As already mentioned data available in the literature was used to investigate correlations between detected ionization free charge and scintillation light as function of the applied electric field ε and deposited energy dE/dx.

The analysis for ER utilized data from eight papers containing 15 datasets[5] [95] [11] [6] [10] [72] [9] [8]. The data represented in fig. 4.5b, 4.2a, 4.2b, and 5.1 were used on the development of the LArQL global fit. The remaining datasets were employed to compare the fitted LArQL model with independent measured data shown in fig. 4.5a, 6.19b, 6.19a, 4.10, and 4.12. The global fit developed in this work takes as starting point the original LArQL parameters configuration (tab. 5.1) which renders the curve estimates compared to the data as shown in fig. 5.2c, 5.2b, and 5.2a with original plots from [4].

This section discusses the statistical procedures used for the LArQL model parameters determination and uncertainties assessment methods.

5.2.1 Software framework

The ROOT package[106] [107] was used as main platform for the development of this work's computational analysis as it offers its C++ code interpreter environment which integrates a

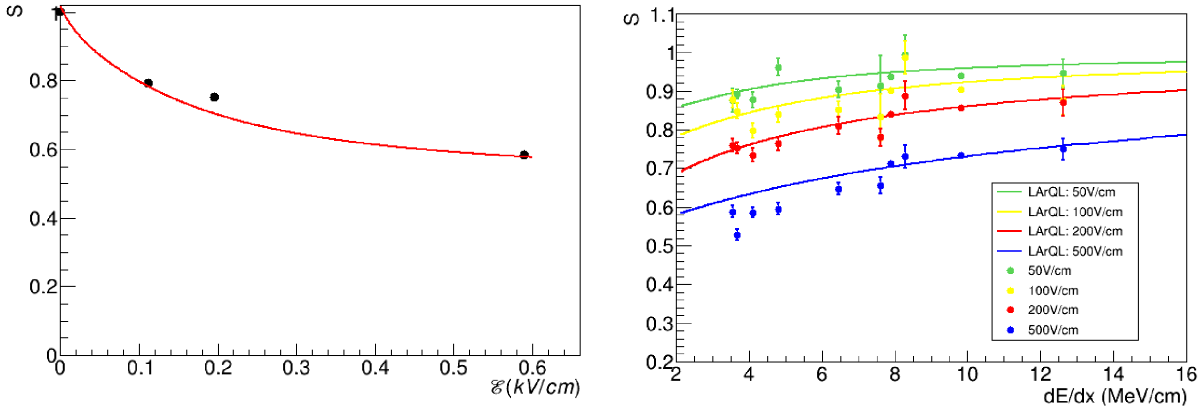

(a) The scintillation ratio S for $dE/dx = mip$ as a function of ε. Data (black dots) from[6] and LArQL curve from[4].

(b) The scintillation S as a function of dE/dx. Data from[95], LArQL curve from[4].

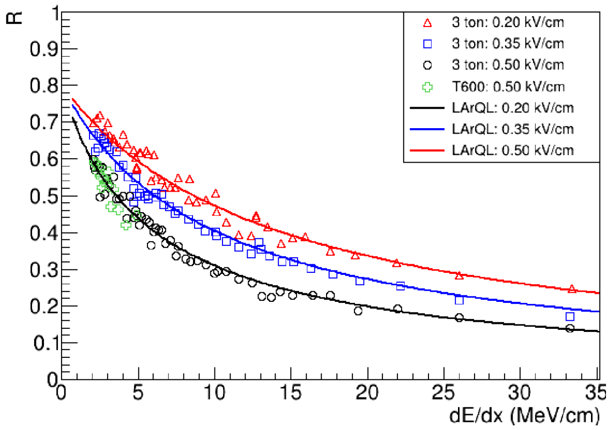

(c) The recombination $\mathscr{R}$ as a function of dE/dx. Data from[102], LArQL curve from[4].

FIGURE 5.2 – Comparative analysis of scintillation, recombination, light, and charge yield under various conditions. Data used in the fit. Figures taken from[4].

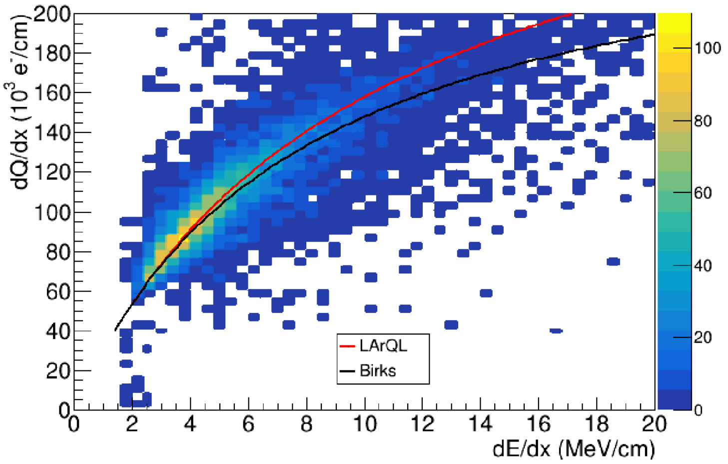

FIGURE 5.3 – The charge production per unit length (dQ/dx) as a function of the dE/dx comparison from Birks' model (black line) and LArQL model (red line). Data taken from[72] and curve estimations from[4].

broad range of libraries and functionalities without requiring code compilation. It is a framework developed at CERN, mainly for particle physics research, to facilitate storage, processing, visualization, and analysis of scientific data.

In these studies the key advantages of using ROOT include:

- **Data handling facilities:** As it was created for large datasets analysis it provides a dedicated library (TTree) to represent columnar data optimized for fast data handling and basic pre-processing;
- **Visualization tools:** Offers a large set of good quality graphic classes for data representation. In particular histograms, scatter graphs and curve plots were used for the data and LArQL studies presented in this dissertation. These classes also provide estimators for typical statistical metrics.
- **Random sampling generators:** Provides random number interface for different generators allowing for sampling of the most common statistical distributions (uniform, gaussian, exponential, binomial, etc). Other distributions can be easily implemented too.

5.2.2 LArQL fit to data

For the LArQL global fit implementation, a set of algorithms was developed in C++ using the ROOT framework[106] to explore variations of the model parameters and perform a better data regression. This implementation was developed in four stages, each aiming at gradually refining the search for a better set of parameters improving the data representation by the LArQL model. In each stage, a suitable search strategy was adopted accordingly.

One of the developed algorithms for global fit generated data files in which each line contained a set of parameters along with the corresponding SSR values for each dataset, organized in columns. The parameter selection algorithm was designed to identify the minimum SSR value for each column using the ROOT framework. This algorithm reads the input data, iterates through all stored entries, and, upon finding the smallest SSR value for each column, records it in an output file along with the associated parameter values.

The first stage consisted of a multidimensional scan on the model parameters, adopting broad ranges of values assumed for those. This early stage aimed to establish regions of interest for searching for good model fits localized in regions beyond the vicinity of the original set of parameters. Each of the parameter values was independently and linearly varied with a fixed step width and within constrained nested loops, such that all combinations of parameters in the multidimensional grid of points could be tried. A total of $N = 10$ different values were assumed per parameter. Therefore, a total of N^8 points were evaluated. For each of these parameter points, figures of merit were evaluated for every dataset used. The ranges adopted for the first stage are listed in tab. 5.2. Notice the ranges adopted for the Birks' parameters were chosen to be $\pm 3\sigma$ limited around the central values provided in[5] in order to keep these within statistically comparable numerical values.

TABLE 5.2 – Intervals utilized for searching the fit parameters for 1^{st} stage.

parameters	$k_B (gV/cm^3 MeV)$	A_B	$\chi_0 1$	$\chi_0 2$
minimum	46.98	0.79	2.67×10^{-03}	-10.96
maximum	50.22	0.81	4.64×10^{-03}	-1.96

parameters	$\chi_0 3$	$\chi_0 4$ $(\mathrm{MeV/cm})^{-1}$	α (V/cm)	β (V/cm)
minimum	1.24	8.92×10^{-05}	0.0104	0.0035
maximum	2.16	2.99×10^{-04}	0.064	0.021

The second stage also consisted on the same type of scan, however, with a much finer grid. The same number N of points per parameter range was used, but all intervals were made much narrower. Only the two ranges regarding the Birks model were kept unchanged with respect to the first stage.

The first and second type of scans were actually performed more than once with minor adjustments in order to guarantee adequate multidimensional parameter spaces were established, containing good candidate values. To determine that, for every fixed parameter set tried, the SSR_i[108] was evaluated between LArQL estimates and the measured points of the *i-th* datasets. These included all the ionization charge and scintillation light datasets intended for the global fit. This way it was possible to establish suitable search regions.

In the third and fourth stages, an additional step was introduced due to the method used to obtain the parameters. In the developed algorithm, a `srand()` command was implemented to generate random datasets within the adopted parameter range for these stages. To prevent unnecessarily large files, a filtering function was applied to save only those parameter sets whose SSR values were less than or equal to the original values listed in Table 6.1. As a result, all stored parameter sets improved the LArQL estimates, and the best-performing results were selected as the output of the fitting stage.

In the third stage it was utilized a random search approach was utilized, where the parameter values were sampled independently around central values listed in tab. 5.1 within defined ranges determined in the previous scan stages. In this stage, the global fit was implemented and a reasonable LArQL parameter set could be achieved through the minimization of a weighted sum of squared residues given by:

$$WSSR = \sum_i \frac{SSR_i}{n_i (RMS^i_{best})^2}, \tag{5.12}$$

where n_i is the number of points for the *i-th* dataset and RMS^i_{best} was calculated with an intermediate fit of the model to each *i-th* dataset individually assuming a very good data representation of the data sets by LArQL. A condition was imposed that the SSR_i should not exceed their equivalent estimates obtained with the original parameters of LArQL according to tab 5.1 .

The fourth and last stage of the LArQL global fit followed the same steps, with the difference being an increased number of draws, enhancing the probability of finding better parameter sets tenfold compared to the third optimization. This step was repeated many times, such that the method uncertainties on the parameters evaluation could be established. Based on these results, a set of histograms was generated to examine the distributions and identify the regions where values tend to cluster. The correlation between the determined parameters was also studied. The results for the parameter sets from each dataset and the global fit obtained from each optimization can be found in ch. 6.

It was also observed that LArQL provides a reasonable description of some of the most recent experimental data, taken from refs.[10] [11] [9] [72] and [8], using the same set of parameters identified in the fourth optimization. To visualize the changes in fit quality, a series of graphs comparing the experimental data with the model curve and the residuals between data and estimates were developed.

6 Analysis Results

The present chapter presents the results from the procedures described in ch. 5. Sec. 6.1 discuss the results obtained for the four stages of integrating the global fit. Sec. 6.2 exhibits the comparison of LArQL estimates with the experimental datasets that were not used in the global fit.

6.1 Results for the fit to the available data

The parameters stage occurs when the SSR_i values evaluated for the nine datasets dedicated to the fit refinement (see ch. 4) reach a satisfactory level, which is when those are all smaller than the calculated with the original LArQL parameter sets and reasonably close to the single dataset model fits. In chapter 5, it was described how the fitting procedures were performed in four stages. The main goal was to have robust proof of concept for the implementation of a multi-dataset fit and statistically determine the best parameter values for the LArQL model.

TABLE 6.1 – Original SSR obtained from original parameters from[4]. Data taken from[5] [95] and [6]. These values are used as a reference for the subsequent stage processes to evaluate the quality of the fit.

Dataset	**SSR**
ICARUS $\mathscr{R}\,(dE/dx)$, $\varepsilon = 200$ kV/cm	4.36×10^{-4}
ICARUS $\mathscr{R}\,(dE/dx)$, $\varepsilon = 350$ kV/cm	3.58×10^{-4}
ICARUS $\mathscr{R}\,(dE/dx)$, $\varepsilon = 500$ kV/cm	5.79×10^{-4}
ICARUS $\mathscr{R}(\varepsilon)$	5.83×10^{-5}
Doke, *et al.*, $S\,(\varepsilon)$	1.70×10^{-3}
ARIS $S\,(dE/dx)$, $\varepsilon = 50$ kV/cm	1.10×10^{-3}
ARIS $S\,(dE/dx)$, $\varepsilon = 100$ kV/cm	2.50×10^{-3}
ARIS $S\,(dE/dx)$, $\varepsilon = 200$ kV/cm	6.67×10^{-4}
ARIS $S\,(dE/dx)$, $\varepsilon = 500$ kV/cm	1.51×10^{-3}

Subsec. 6.1.1 describes the outcomes obtained from the exploratory broad parameter scans performed. The values of parameters were evaluated for each dataset and the minimum SSR_i achieved were evaluated. Comparison plots between data and model estimates are shown. Subsection 6.1.2 presents the second stage results. Studies similar to those performed in the first stage were made and narrow search ranges were proposed. Subsec. 6.1.3 presents the details

of the global fit implementation indicating comparison plots, SSR_i minimal values obtained with individual dataset fits, succeeded $WSSR$ from the global regression and parameters central values. Lastly, in subsec. 6.1.4 the fourth stage is explained as it provides the means for the complete determination model parameter values indicating the sampling choices and uncertainties determination.

The SSR_i values obtained adopting the original set of parameters of LArQL are shown in tab. 6.1. These are used for the global fit improvement evaluation at the last stages.

6.1.1 First stage

In this early stage, the parameters were scanned and used to find the set of parameters that reduces the SSR_i of each dataset compared to the model estimations. The ranges adopted were presented in tab. 5.2, and the coarse segmentation widths were determined by each parameter range divided by the N number of values per parameter.

The obtained SSR_i estimates and their respective parameters set for each dataset fitted are listed in tab. 6.2. The SSR values found for each dataset were, for the ICARUS[5] datasets $\mathscr{R}(dE/dx)$: 3.8×10^{-4} ($\varepsilon = 200$ V/cm), 3.0×10^{-4} ($\varepsilon = 350$ V/cm), 5.4×10^{-4} ($\varepsilon = 500$ V/cm) and for $\mathscr{R}(\varepsilon)$, 6.5×10^{-6} ($dE/dx = m.i.p.$). For Doke *et al.*[6] $S(\varepsilon)$ dataset, 1.6×10^{-2}. For ARIS[11] $S(dE/dx)$: 1.08×10^{-3} ($\varepsilon = 50$ V/cm), 4.1×10^{-3} ($\varepsilon = 100$ V/cm), 5.7×10^{-3} ($\varepsilon = 200$ V/cm) and 3.2×10^{-3} ($\varepsilon = 500$ V/cm). For comparison with the original LArQL configuration, see tab. 6.1.

TABLE 6.2 – Datasets with the parameters obtained in the 1^{st} stage. The graphical results and residuals are presented in figs. 6.1. The reference SSR values are listed in Tab. 6.1.

Dataset	**SSR**	k_B **(g V/cm^3 MeV)**	A_B	$\chi_0 1$	$\chi_0 2$	$\chi_0 3$	$\chi_0 4$ (MeV/cm)$^{-1}$	α **(V/cm)**	β **(V/cm)**
ICARUS 200V	3.80×10^{-4}	46.98	0.79	2.70×10^{-3}	-6.96	1.95	8.90×10^{-5}	6.40×10^{-2}	2.10×10^{-2}
ICARUS 350V	3.03×10^{-4}	50.22	0.81	4.40×10^{-3}	-3.96	1.24	8.90×10^{-5}	6.40×10^{-2}	2.10×10^{-2}
ICARUS 500V	5.40×10^{-4}	48.78	0.81	4.60×10^{-3}	-3.96	1.34	2.50×10^{-4}	6.40×10^{-2}	2.10×10^{-2}
ICARUS $\mathscr{R}(\varepsilon)$	6.50×10^{-6}	46.98	0.80	4.60×10^{-3}	-6.96	1.95	8.90×10^{-5}	6.40×10^{-2}	2.10×10^{-2}
Doke, *et al.*	1.60×10^{-2}	50.22	0.79	4.60×10^{-3}	-6.96	1.95	8.90×10^{-5}	1.04×10^{-2}	3.50×10^{-3}
ARIS 50V	1.10×10^{-3}	50.22	0.79	4.60×10^{-3}	-6.96	1.95	8.90×10^{-5}	1.04×10^{-2}	3.50×10^{-3}
ARIS 100V	4.11×10^{-3}	50.22	0.79	4.60×10^{-3}	-6.96	1.95	8.90×10^{-5}	1.04×10^{-2}	3.50×10^{-3}
ARIS 200V	5.70×10^{-3}	50.22	0.79	4.60×10^{-3}	-6.96	1.95	8.90×10^{-5}	1.04×10^{-2}	3.50×10^{-3}
ARIS 500V	3.20×10^{-3}	50.22	0.79	4.60×10^{-3}	-6.96	1.95	8.90×10^{-5}	1.04×10^{-2}	9.40×10^{-3}

Four out of nine datasets did not have SSRs smaller than their correspondents in tab 6.1 in this particular stage: Doke, *et al.*[6], ARIS datasets for $100, 200$ and 500 V/cm[7]. All of the ICARUS[5] datasets succeeded in this stage. The parameters values found for Doke *et al.*[6], ARIS $\varepsilon = 50, 100$ and 200 V/cm datasets were the same, but only the ARIS $\varepsilon = 50$ V/cm dataset succeeded.

Each of the datasets were compared with predictions performed with LArQL through plots of the S and $\mathscr{R}$ measured quantities as function of dE/dx or ε. The corresponding residuals were also produced and are presented. The dark maroon lines represent the theoretical values

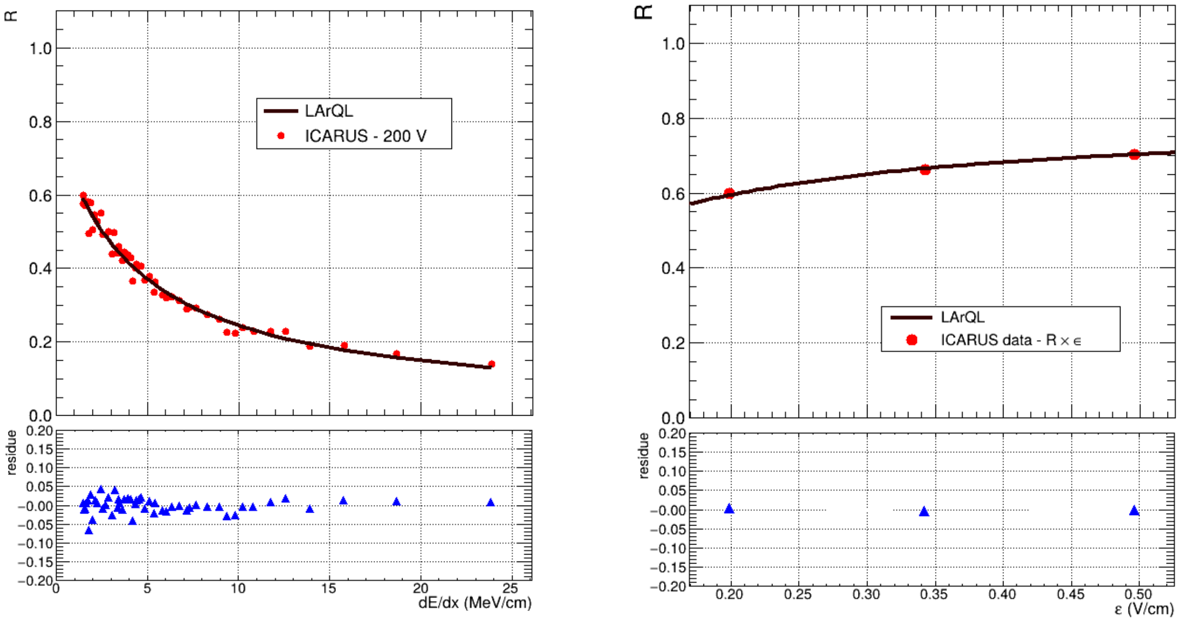

(a) ICARUS data, $\mathscr{R}(dE/dx)$, $\varepsilon = 200\,\text{V/cm}$ (succeeded).

(b) ICARUS data, $\mathscr{R}(\varepsilon)$, $\frac{dE}{dx}$ = mip (succeeded).

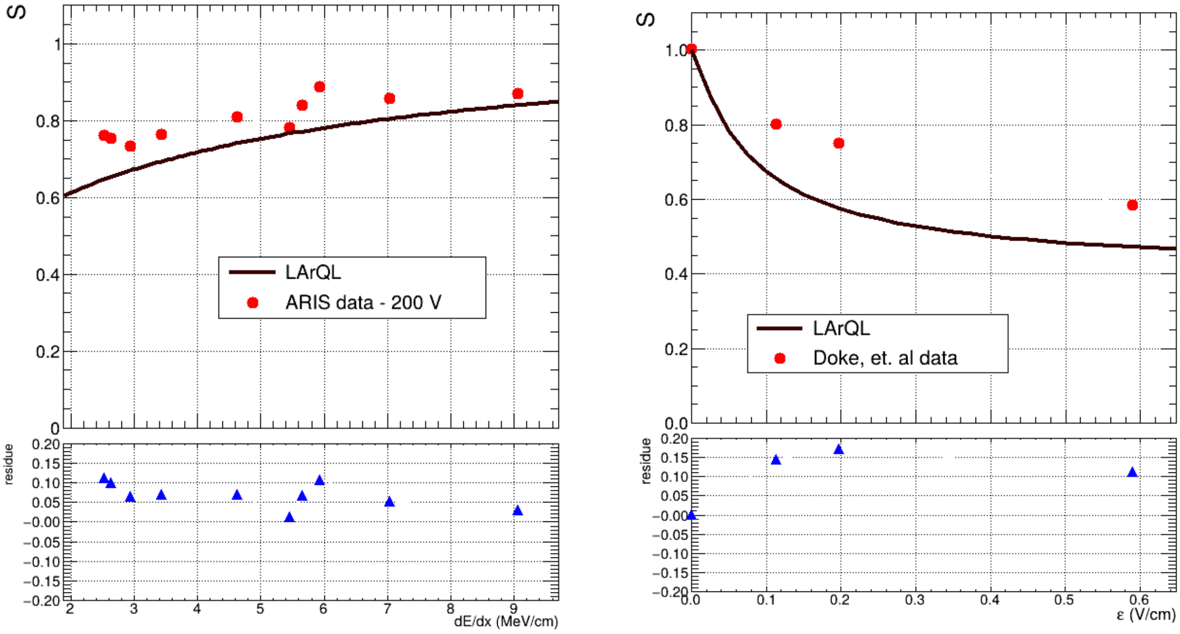

(c) ARIS data, $S(dE/dx)$, $\varepsilon = 200\,\text{V/cm}$ (not succeeded).

(d) Doke, *et al.*, $S(\varepsilon)$, $\frac{dE}{dx}$ = mip (not optmized).

FIGURE 6.1 – Results of the first stage for ICARUS[5], ARIS[11], and Doke, *et al.*[6] datasets at $\varepsilon = 200\,\text{V/cm}$ for ICARUS and ARIS data, and $\frac{dE}{dx}$ = mip.

provided by LArQL. The red dots are the experimental data and the lower graphs are for the visual representation of the residuals, represented by blue triangles. The graphs obtained from the parameter sets from tab. 6.2 are displayed in figs 6.1, representing the adjustment for $S(\varepsilon)$, $\mathscr{R}(\varepsilon)$, $S(dE/dx)$ (both for $dE/dx = m.i.p$) and $\mathscr{R}(dE/dx), \varepsilon$ (both for $\varepsilon = 200$ V/cm). Figs 6.1a and 6.1b show curves for ICARUS $\mathscr{R}$ data which are near the data points as expected. Note in figs. 6.1d and 6.1c the curves are shifted down from the data clusters indicating further degradation as it was also expected based on the obtained values of SSR_i obtained in this stage.

Similar plots were produced for all datasets (used for the fit) and are listed in the appendix A.1.

TABLE 6.3 – Parameter limits adopted on the stages.

parameters	$k_B\,(gV/cm^3MeV)$	A_B	$\chi_0 1$	$\chi_0 2$	$\chi_0 3$	$\chi_0 4$ (MeV/cm)$^{-1}$	$\alpha\,(V/cm)$	$\beta\,(V/cm)$
minimum	46.98	0.79	2.67×10^{-3}	-10.96	1.24	8.92×10^{-2}	1.04×10^{-2}	3.47×10^{-3}
maximum	50.22	0.81	4.64×10^{-3}	-1.96	2.16	2.99×10^{-4}	6.40×10^{-2}	2.13×10^{-2}

The results showed that it was necessary to decrease the scan range to find the best parameters for the dataset description with the global parameters. For that, the second search stage was implemented.

6.1.2 Second stage

The second stage followed the same steps as the first stage, with different parameter ranges. It scanned a parameter for 10 values and kept others constant, repeating the procedure for all possible parameter configurations within the grid of points established, as shown in tab. 6.4.

TABLE 6.4 – Interval utilized for searching the fit parameters for 2^{nd} stage.

parameters	$k_B(gV/cm^3MeV)$	A_B	$\chi_0 1$	$\chi_0 2$	$\chi_0 3$	$\chi_0 4$ (MeV/cm)$^{-1}$	$\alpha\ (V/cm)$	$\beta\ (V/cm)$
minimum	46.98	0.79	3.54×10^{-3}	-5.96	1.65	1.82×10^{-4}	3.4×10^{-2}	1.1×10^{-2}
maximum	50.22	0.81	3.76×10^{-3}	-4.96	1.75	2.06×10^{-4}	4.02×10^{-2}	1.3×10^{-2}

Some parameter ranges were kept the same compared to the 1^{st} stage. The parameters A_B and k_B kept the same intervals, from 4.698×10^1 to 5.022×10^1 and 7.9×10^{-1} and 8.0×10^{-1}, respectively. The range adopted for $\chi_0 1$ was 3.5×10^{-3} to 3.8×10^{-3}, from 5^{th} to 6^{th} steps. The range of $\chi_0 2$ was -5.96 to -4.96, from 6^{th} to 7^{th} steps. The parameters $\chi_0 3, \chi_0 4, \alpha$ and β were varied in the same range steps, from 5^{th} to 6^{th}. The values adopted were from 1.65 to 1.75, from 1.8×10^{-4} to 2.05×10^{-4}, from 3.4×10^{-2} to 4.01×10^{-2} and from 1.1×10^{-2} to 1.3×10^{-2}, respectively, also divided by 10 steps.

It was observed that most of the parameter sets that produced the most significant SSR_i reductions were located in certain ranges, smaller than the ones adopted in the first stage. The results are listed in tab. 6.5. The SSR results of the second stage were, for the ICARUS[5] datasets $\mathscr{R}(dE/dx)$: 3.9×10^{-4} ($\varepsilon = 200$ V/cm), 3.0×10^{-4} ($\varepsilon = 350$ V/cm), 5.4×10^{-4}

($\varepsilon = 500$ V/cm) and for $\mathscr{R}(\varepsilon)$, 1.3×10^{-6} ($dE/dx = m.i.p.$). For Doke *et al.*[6] $S(\varepsilon)$ dataset, 3.4×10^{-3}. For ARIS[11] $S(dE/dx)$: 7.8×10^{-4} ($\varepsilon = 50$ V/cm), 2.2×10^{-3} ($\varepsilon = 100$ V/cm), 6.8×10^{-4} ($\varepsilon = 200$ V/cm) and 8.2×10^{-4} ($\varepsilon = 500$ V/cm).

TABLE 6.5 – Datasets with the parameters, obtained from the 2^{nd} stage, that perform the fit. The graph results and their residuals are depicted in fig. B.1.

Dataset	**SSR**	k_B **(g V/cm^{3}MeV)**	A_B	$\chi_0 1$	$\chi_0 2$	$\chi_0 3$	$\chi_0 4$ (MeV/cm)$^{-1}$	α **(V/cm)**	β **(V/cm)**
ICARUS 200*V*	3.87×10^{-4}	46.98	0.7973	3.66×10^{-3}	-5.31	1.68	1.84×10^{-4}	3.99×10^{-2}	1.33×10^{-2}
ICARUS 350*V*	3.04×10^{-4}	50.22	0.8063	3.55×10^{-3}	-5.91	1.75	2.04×10^{-4}	3.99×10^{-2}	1.33×10^{-2}
ICARUS 500*V*	5.41×10^{-4}	49.14	0.8081	3.75×10^{-3}	-5.51	1.69	1.84×10^{-4}	3.99×10^{-2}	1.33×10^{-2}
ICARUS $\mathscr{R}(\varepsilon)$	1.33×10^{-6}	47.34	0.8027	3.75×10^{-3}	-5.61	1.73	1.84×10^{-4}	3.99×10^{-2}	1.33×10^{-2}
Doke, *et al.*[6]	3.42×10^{-3}	50.22	0.7919	3.75×10^{-3}	-5.21	1.65	1.84×10^{-4}	3.45×10^{-2}	1.15×10^{-2}
ARIS 50*V*	7.80×10^{-4}	50.22	0.7919	3.66×10^{-3}	-5.71	1.75	2.04×10^{-4}	3.99×10^{-2}	1.15×10^{-2}
ARIS 100*V*	2.21×10^{-3}	48.42	0.7919	3.75×10^{-3}	-5.21	1.65	2.04×10^{-4}	3.99×10^{-2}	1.15×10^{-2}
ARIS 200*V*	6.85×10^{-4}	50.22	0.7919	3.75×10^{-3}	-5.21	1.65	1.84×10^{-4}	3.63×10^{-2}	1.15×10^{-2}
ARIS 500*V*	8.22×10^{-4}	50.22	0.8081	3.58×10^{-3}	-5.21	1.65	1.84×10^{-4}	3.45×10^{-2}	1.15×10^{-2}

Some of the graphs representing the LArQL curve adjustments for $S(\varepsilon)$, $\mathscr{R}(\varepsilon)$, $S(dE/dx)$ (both for $dE/dx = m.i.p$) and $\mathscr{R}(dE/dx), \varepsilon$ (both for $\varepsilon = 200$ V/cm) are depicted in figs. 6.2. In this stage, figs 6.2c and 6.2d show curves that are still shifted down from their data points, but less than in the first stage. Compared with the values in tab. 6.1, it was noted that only these two datasets did not succeed at this stage: Doke, *et al.*[6] and ARIS 200 V/cm[7]. The plots produced for all the data sets used in the individual fit procedures are available in appendix B.1.

A multidimensional scan of the model parameters was performed, similar to the first stage, but with different parameter ranges. The results from this stage point the necessity to change the search approach to obtain the individual and global fit parameter sets in the next stage. This change was such to avoid unwanted numerical features such as loss of resolution on the parameters' final determination, which could not be achieved with the simpler fixed-step scan employed in the first two stages. The method performed in the third stage consists on the random sampling sampling of the parameters values within the ranges determined in the second stage.

6.1.3 Third stage

Differently from the first two stages, where were performed scans on the parameters, in the third stage their values were randomly sampled in a total of 10^8 set draws.

An algorithm was developed to filter the outcomes with only parameter sets that offer SSR_i smaller than the original values (tab. 6.1) creating a database and, then, select the best results. The search ranges adopted are the ones obtained in the second stage analysis. The obtained individual and global fit parameter sets are listed in the tabs. 6.6 and 6.7, respectively.

A second set of algorithms was then implemented to scan the database file to search for the model parameter sets that best fitted each dataset individually minimizing their respective SSR_i and finally look for the configuration of parameter set minimizing the $WSSR$ quantity.

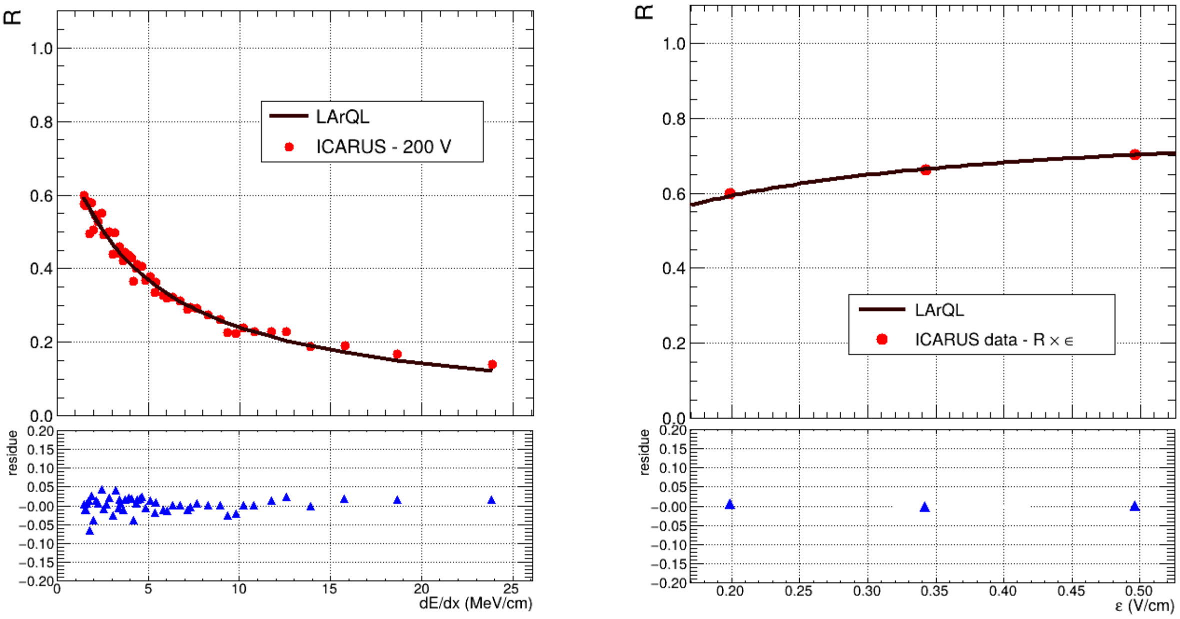

(a) ICARUS data, $\mathscr{R}(dE/dx)$, $\varepsilon = 200\,\mathrm{V/cm}$ (succeeded).

(b) ICARUS data, $\mathscr{R}(\varepsilon)$, $\frac{dE}{dx}$ = mip (succeeded).

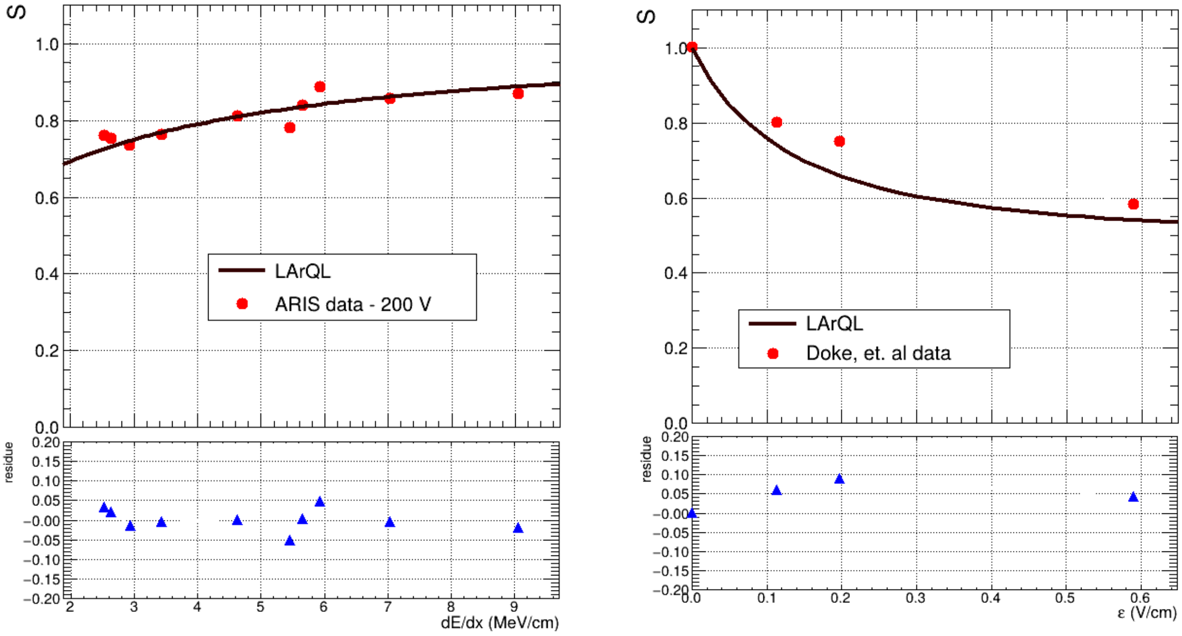

(c) ARIS data, $S(dE/dx)$, $\varepsilon = 200\,\mathrm{V/cm}$ (not succeeded).

(d) Doke, *et al.*, $S(\varepsilon)$, $\frac{dE}{dx}$ = mip (not succeeded).

FIGURE 6.2 – Results of the second stage for ICARUS[5], ARIS[11], and Doke, *et al.*[6] datasets at $\varepsilon = 200\,\mathrm{V/cm}$ for ICARUS and ARIS data, and $\frac{dE}{dx}$ = mip.

Tab. 6.6 lists the obtained individual SSR_i^{min} and the respective parameters. Those values were, for ICARUS[5] $\mathscr{R}(dE/dx)$: 4.1×10^{-4} ($\varepsilon = 200$ V/cm), 3.3×10^{-4} ($\varepsilon = 350$ V/cm), 5.5×10^{-4} ($\varepsilon = 500$ V/cm) and for $\mathscr{R}(\varepsilon)$, 3.3×10^{-5} ($dE/dx = m.i.p.$). For Doke *et al.*[6] $S(\varepsilon)$ dataset, 1.52×10^{-3}. For ARIS[11] $S(dE/dx)$: 9.9×10^{-4} ($\varepsilon = 50$ V/cm), 2.33×10^{-3} ($\varepsilon = 100$ V/cm), 6.3×10^{-4} ($\varepsilon = 200$ V/cm) and 1.42×10^{-3} ($\varepsilon = 500$ V/cm).

Note that, in tab. 6.6, the same parameter sets were found for ICARUS $\varepsilon =$

TABLE 6.6 – Datasets with the parameters, obtained from 3^{rd} stage, that perform the fit. The graph results and their residuals are depicted in fig. C.1.

Dataset	SSR	k_B (g V/cm^{3}MeV)	A_B	$\chi_0 1$	$\chi_0 2$	$\chi_0 3$	$\chi_0 4$ (MeV/cm)$^{-1}$	α (V/cm)	β (V/cm)
ICARUS 200V	4.07×10^{-4}	50.18	0.81	3.69×10^{-3}	-5.73	1.75	2.03×10^{-4}	3.75×10^{-2}	1.34×10^{-2}
ICARUS 350V	3.26×10^{-4}	50.18	0.81	3.69×10^{-3}	-5.73	1.75	2.03×10^{-4}	3.75×10^{-2}	1.34×10^{-2}
ICARUS 500V	5.50×10^{-4}	49.99	0.81	3.61×10^{-3}	-5.63	1.73	2.04×10^{-4}	3.73×10^{-2}	1.34×10^{-2}
ICARUS $\mathscr{R}(\varepsilon)$	3.27×10^{-5}	49.99	0.81	3.61×10^{-3}	-5.63	1.73	2.04×10^{-4}	3.73×10^{-2}	1.34×10^{-2}
Doke, *et al.*	1.52×10^{-3}	49.89	0.81	3.62×10^{-3}	-5.68	1.74	2.05×10^{-4}	3.90×10^{-2}	1.16×10^{-2}
ARIS 50V	9.86×10^{-4}	49.35	0.80	3.59×10^{-3}	-5.63	1.73	2.04×10^{-4}	4.01×10^{-2}	1.22×10^{-2}
ARIS 100V	2.33×10^{-3}	49.35	0.80	3.59×10^{-3}	-5.63	1.73	2.04×10^{-4}	4.01×10^{-2}	1.22×10^{-2}
ARIS 200V	6.31×10^{-4}	49.35	0.80	3.59×10^{-3}	-5.63	1.73	2.04×10^{-4}	4.01×10^{-2}	1.22×10^{-2}
ARIS 500V	1.42×10^{-3}	49.99	0.81	3.61×10^{-3}	-5.63	1.73	2.04×10^{-4}	3.73×10^{-2}	1.34×10^{-2}

200 and 350 V/cm, for ICARUS $\varepsilon = 500$ V/cm, $\mathscr{R}(\varepsilon)$ and ARIS $\varepsilon = 500$ V/cm, and for ARIS $\varepsilon = 50, 100$ and 200 V/cm. These results indicated that the method adopted seemed effective in clustering the parameter values around smaller bounds to find the global parameter set without constraints.

Figs. 6.3 represent the adjustment to data for $S(\varepsilon)$, $\mathscr{R}(\varepsilon)$, $S(dE/dx)$ (both for $dE/dx = m.i.p$) and $\mathscr{R}(dE/dx), \varepsilon$ (both for $\varepsilon = 200$ V/cm). In this case,for all datasets the estimation curves are near the data points, pointing to better results than the first two stages. For all the datasets included on the fit graphic comparisons were produced and are available at appendix C.1.

Global fit final procedure for 3^{rd} stage

For the global fit parameter sets determination, the lowest $WSSR$ was found, calculated with eq. 5.12. The algorithm developed in this step was based on the methods described in ch. 5, and the global parameter set is shown in tab. 6.7.

TABLE 6.7 – Global parameter set from the 3^{rd} stage.

WSSR (sum)	k_B (g V/cm^{3}MeV)	A_B	$\chi_0 1$	$\chi_0 2$	$\chi_0 3$	$\chi_0 4$ (MeV/cm)$^{-1}$	α (V/cm)	β (V/cm)
9.78	49.99	0.81	3.61×10^{-3}	-5.63	1.73	2.04×10^{-4}	3.73×10^{-2}	1.34×10^{-2}

TABLE 6.8 – Individual SSR_i^{min} results, obtained from 3^{rd} stage, global fit.

Dataset	SSR	k_B (g V/cm^{3}MeV)	A_B	$\chi_0 1$	$\chi_0 2$	$\chi_0 3$	$\chi_0 4$ (MeV/cm)$^{-1}$	α (V/cm)	β (V/cm)
ICARUS 200V	4.16×10^{-4}	49.99	0.81	3.61×10^{-3}	-5.63	1.73	2.04×10^{-4}	3.73×10^{-2}	1.34×10^{-2}
ICARUS 350V	3.43×10^{-4}								
ICARUS 500V	5.50×10^{-4}								
ICARUS $\mathscr{R}(\varepsilon)$	3.27×10^{-5}								
Doke, *et al.*	1.69×10^{-3}								
ARIS 50V	1.10×10^{-3}								
ARIS 100V	2.48×10^{-3}								
ARIS 200V	6.57×10^{-4}								
ARIS 500V	1.42×10^{-3}								

The SSR_i in this stage were, for ICARUS[5] $\mathscr{R}(dE/dx)$: 4.16×10^{-4} ($\varepsilon = 200$ V/cm), 3.43×10^{-4} ($\varepsilon = 350$ V/cm), 5.5×10^{-4} ($\varepsilon = 500$ V/cm) and for $\mathscr{R}(\varepsilon)$, 3.27×10^{-5} ($dE/dx = m.i.p.$). For Doke *et al.*[6] $S(\varepsilon)$ dataset, 1.69×10^{-3}. For ARIS[11] $S(dE/dx)$: 1.1×10^{-3} ($\varepsilon =$

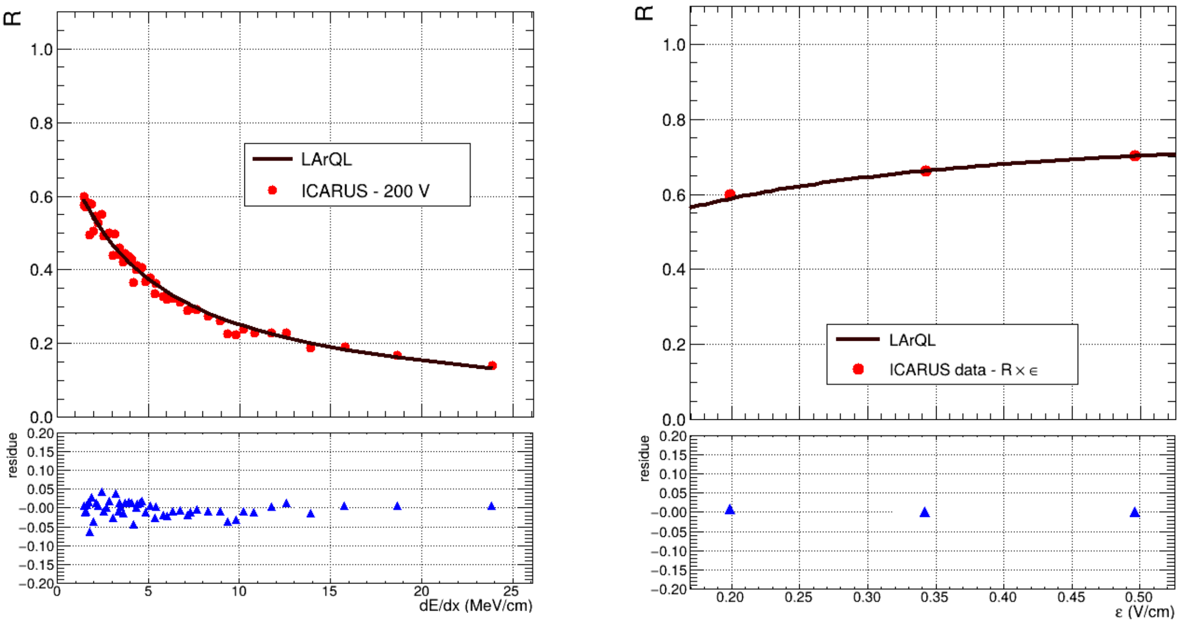

(a) ICARUS data, $\mathscr{R}(dE/dx)$, $\varepsilon = 200\,\mathrm{V/cm}$ (succeeded).

(b) ICARUS data, $\mathscr{R}(\varepsilon)$, $\frac{dE}{dx}$ = mip (succeeded).

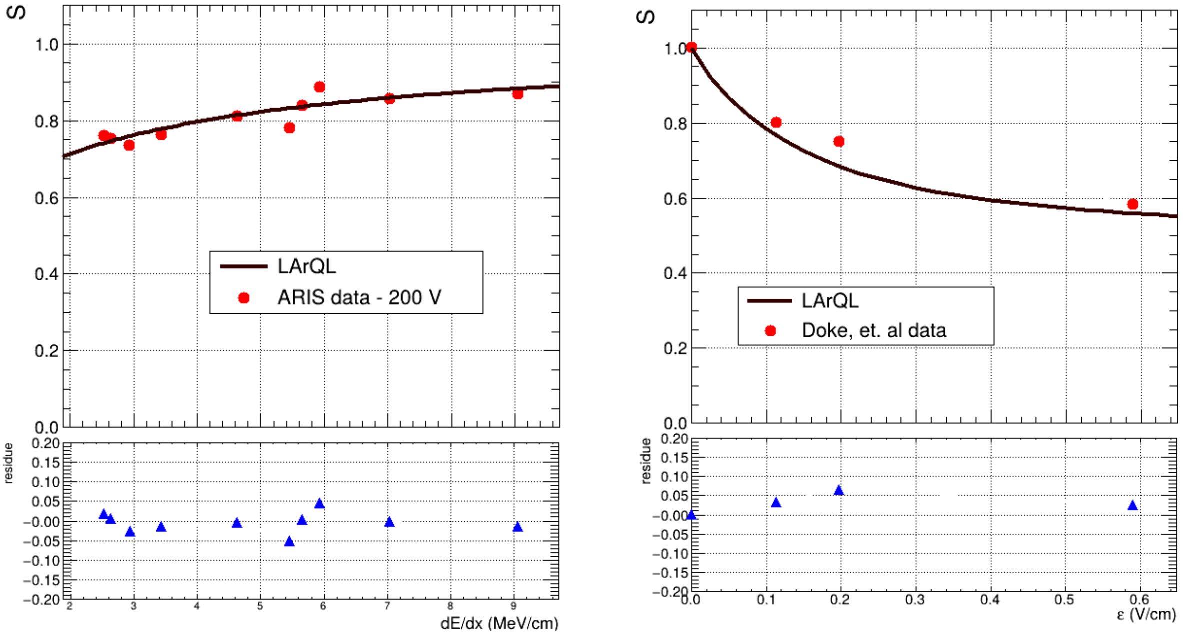

(c) ARIS data, $S(dE/dx)$, $\varepsilon = 200\,\mathrm{V/cm}$ (succeeded).

(d) Doke, *et al.*, $S(\varepsilon)$, $\frac{dE}{dx}$ = mip (succeeded).

FIGURE 6.3 – Results of the third stage for ICARUS[5], ARIS[11], and Doke, *et al.*[6] datasets at $\varepsilon = 200\,\mathrm{V/cm}$ for ICARUS and ARIS data, and $\frac{dE}{dx}$ = mip, individually.

50 V/cm), 2.48×10^{-3} ($\varepsilon = 100$ V/cm), 6.57×10^{-4} ($\varepsilon = 200$ V/cm) and 1.42×10^{-3} ($\varepsilon = 500$ V/cm), as shown in tab. 6.8.

Figs. 6.4 were obtained with the parameter set from tab. 6.7. As mentioned, this searching approach points to the parameter values in which they are clustered. Notice the similarity between figs 6.3 and 6.4 suggest a good quality and simultaneous description of all datasets can be achieved with a single set of parameters. In addition, the global set found in this stage

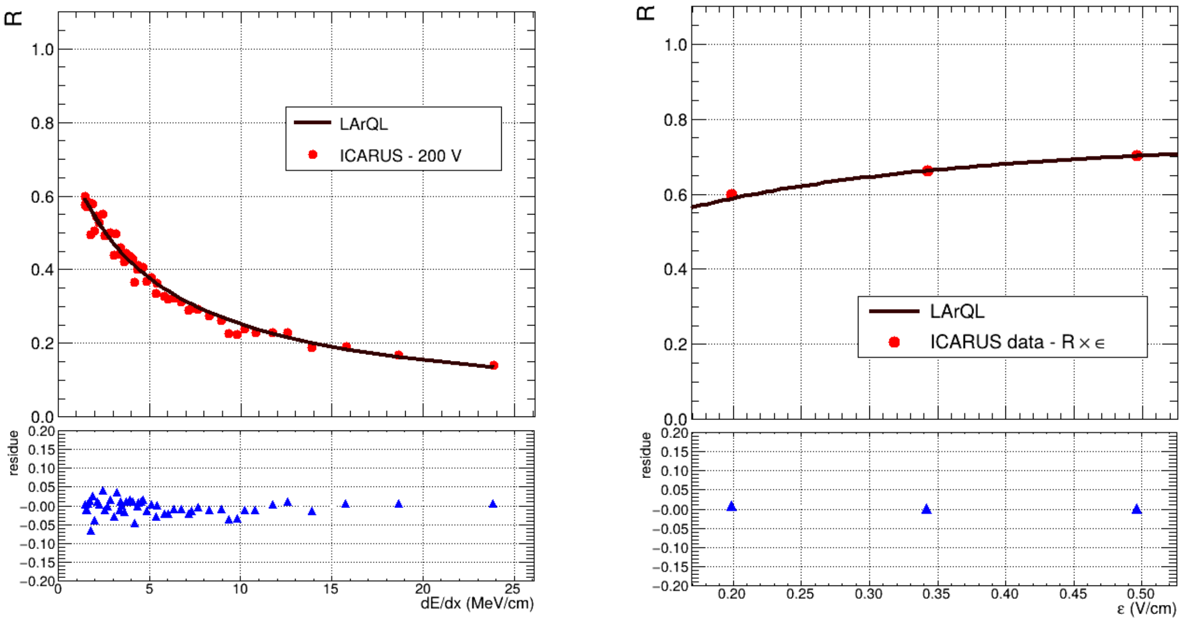

(a) ICARUS data, $\mathscr{R}(dE/dx)$, $\varepsilon = 200\,\text{V/cm}$ (succeeded).

(b) ICARUS data, $\mathscr{R}(\varepsilon)$, $\frac{dE}{dx} = \text{mip}$ (succeeded).

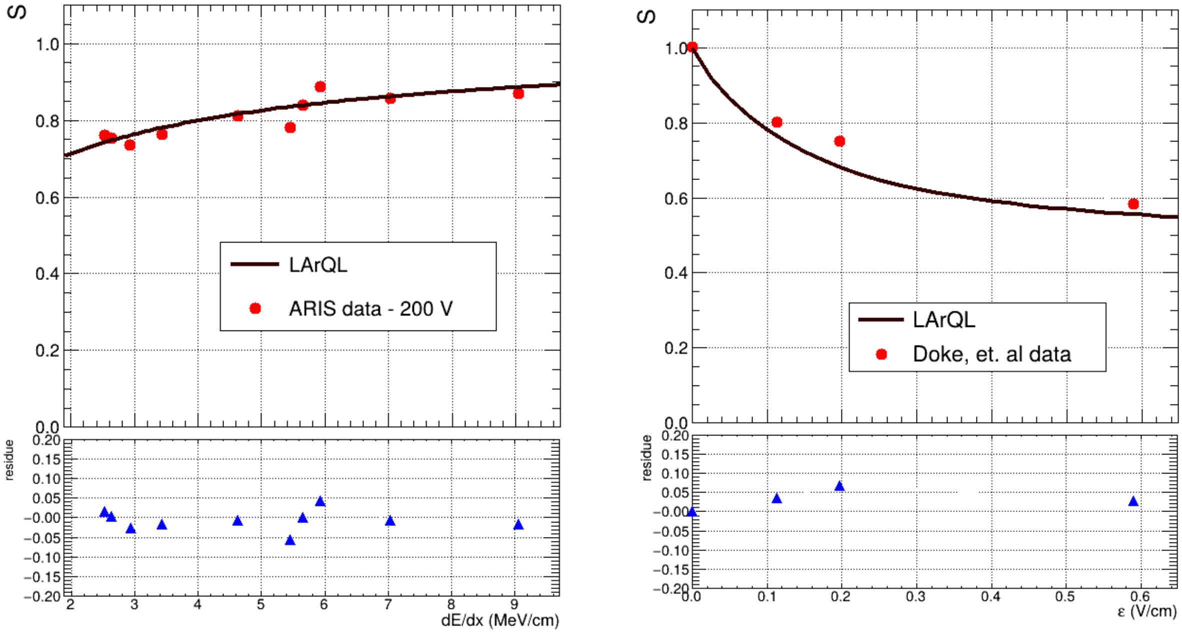

(c) ARIS data, $S(dE/dx)$, $\varepsilon = 200\,\text{V/cm}$ (succeeded).

(d) Doke, *et al.*, $S(\varepsilon)$, $\frac{dE}{dx} = \text{mip}$ (succeeded).

FIGURE 6.4 – Results of the third stage for ICARUS[5], ARIS[11], and Doke, *et al.*[6] datasets at $\varepsilon = 200\,\text{V/cm}$ for ICARUS and ARIS data, and $\frac{dE}{dx} = \text{mip}$, global fit.

is the same that fits the ICARUS $\varepsilon = 500$ V/cm, ICARUS $\mathscr{R}(\varepsilon)$ and ARIS $\varepsilon = 500$ V/cm datasets, individually.

Because of the algorithm developed, the increment of the parameter random samples would also increase the probability of finding better parameter sets that perform the fit to the data, once each run offers different results.

The comparison plots for all data sets used for the individual fitting in the third stage are available in appendix C.1 and the plots using the global fit parameters are show in appendix C.2.

6.1.4 Fourth stage

The fourth stage consisted of the same steps as the third stage, but with an increment in the number of draws up to 10^9. The individual parameter sets that fit the data are listed in tab. 6.9, the global parameters obtained for this stage are shown in tab. 6.11. However, to get a better estimate for the parameters (central values) and their uncertainties, this stage was repeated 30 times.

TABLE 6.9 – Datasets with the parameters, obtained from 4^{th} stage, that perform the individual fit. The graph results and their residuals are depicted in fig. D.1.

Dataset	**SSR**	k_B **(g V/cm^{3}MeV)**	A_B	$\chi_0 1$	$\chi_0 2$	$\chi_0 3$	$\chi_0 4$ (MeV/cm)$^{-1}$	α **(V/cm)**	β **(V/cm)**
ICARUS 200*V*	4.09×10^{-4}	49.95	0.81	3.58×10^{-3}	-5.65	1.73	2.04×10^{-4}	3.76×10^{-2}	1.31×10^{-2}
ICARUS 350*V*	3.29×10^{-4}	49.95	0.81	3.58×10^{-3}	-5.65	1.73	2.04×10^{-4}	3.76×10^{-2}	1.31×10^{-2}
ICARUS 500*V*	5.50×10^{-4}	49.76	0.81	3.57×10^{-3}	-5.52	1.71	2.05×10^{-4}	3.81×10^{-2}	1.20×10^{-2}
ICARUS $\mathscr{R}(\varepsilon)$	2.84×10^{-5}	49.67	0.81	3.60×10^{-3}	-5.70	1.74	2.04×10^{-4}	3.83×10^{-2}	1.31×10^{-2}
Doke, *et al.*	1.49×10^{-3}	49.98	0.81	3.60×10^{-3}	-5.73	1.75	2.03×10^{-4}	3.98×10^{-2}	1.27×10^{-2}
ARIS 50*V*	9.86×10^{-4}	49.78	0.80	3.59×10^{-3}	-5.65	1.73	2.05×10^{-4}	3.98×10^{-2}	1.34×10^{-2}
ARIS 100*V*	2.34×10^{-3}	49.78	0.80	3.59×10^{-3}	-5.65	1.73	2.05×10^{-4}	3.98×10^{-2}	1.34×10^{-2}
ARIS 200*V*	6.30×10^{-4}	49.14	0.80	3.60×10^{-3}	-5.73	1.75	2.05×10^{-4}	3.84×10^{-2}	1.33×10^{-2}
ARIS 500*V*	1.41×10^{-3}	48.92	0.80	3.60×10^{-3}	-5.72	1.75	2.05×10^{-4}	3.67×10^{-2}	1.16×10^{-2}

The same procedure is described in subsec. 6.1.3 of filtering and storing the best results for individual and global parameter sets is applied, and all of the parameter sets found in this stage perform the fit to the data. Table 6.9 shows the SSR_i^{min} per individual dataset obtained for the first instance of the fourth stage. The values found were, for ICARUS[5] $\mathscr{R}(dE/dx)$: 4.1×10^{-4} ($\varepsilon = 200$ V/cm), 3.3×10^{-4} ($\varepsilon = 350$ V/cm), 5.5×10^{-4} ($\varepsilon = 500$ V/cm) and for $\mathscr{R}(\varepsilon)$, 2.8×10^{-5} ($dE/dx = m.i.p.$). For Doke *et al.*[6] $S(\varepsilon)$ dataset, 1.5×10^{-3}. For ARIS[11] $S(dE/dx)$: 9.8×10^{-4} ($\varepsilon = 50$ V/cm), 2.3×10^{-3} ($\varepsilon = 100$ V/cm), 6.3×10^{-4} ($\varepsilon = 200$ V/cm) and 1.4×10^{-3} ($\varepsilon = 500$ V/cm). Note that the same parameter values were found for ICARUS $\varepsilon = 200$ and 350 V/cm, and ARIS $\varepsilon = 50$

In this first instance of this stage, all datasets provided improved SSR_i^{min} when compared to their counterparts evaluated with the original LArQL model set of parameters. The comparison graphs in figs. 6.4 shows the curve estimates offering small residues concerning the data. The graphs for all datasets included on the fit are depicted in figs. D.1.

Global fit for 4^{th} stage

The same procedures described in subsection 6.1.3 were performed to the global fit of the first instance. The $WSSR$ value evaluated for this stage was of 9.68 and the SSR_i^{min}, represented by tab. 6.10 per dataset were, for $\mathscr{R}(dE/dx)$: 4.31×10^{-4} ($\varepsilon = 200$ V/cm), 3.56×10^{-4} ($\varepsilon =$

TABLE 6.10 – Individual SSR_i^{min} results, obtained from 4th stage, global fit (single sample).

Dataset	**SSR**	k_B **(g V/cm^{3}MeV)**	A_B	$\chi_0 1$	$\chi_0 2$	$\chi_0 3$	$\chi_0 4$ (MeV/cm)$^{-1}$	α **(V/cm)**	β **(V/cm)**
ICARUS 200V	4.31×10^{-4}	49.67	0.81	3.60×10^{-3}	-5.70	1.74	2.04×10^{-4}	3.83×10^{-2}	1.31×10^{-2}
ICARUS 350V	3.56×10^{-4}								
ICARUS 500V	5.51×10^{-4}								
ICARUS $\mathscr{R}(\varepsilon)$	2.84×10^{-5}								
Doke, *et al.*	1.69×10^{-3}								
ARIS 50V	1.05×10^{-3}								
ARIS 100V	2.40×10^{-3}								
ARIS 200V	6.39×10^{-4}								
ARIS 500V	1.41×10^{-3}								

350 V/cm), 5.51×10^{-4} ($\varepsilon = 500$ V/cm) and for $\mathscr{R}(\varepsilon)$, 2.84×10^{-5} ($dE/dx = m.i.p.$) for ICARUS[5]. For Doke *et al.*[6] $S(\varepsilon)$ dataset, 1.69×10^{-3}. For ARIS[11] $S(dE/dx)$: 1.05×10^{-3} ($\varepsilon = 50$ V/cm), 2.40×10^{-3} ($\varepsilon = 100$ V/cm), 6.39×10^{-4} ($\varepsilon = 200$ V/cm) and 1.41×10^{-3} ($\varepsilon = 500$ V/cm).

The parameter result is listed in tab. 6.11. The global and the individual parameter sets found for the ICARUS $\mathscr{R}(\varepsilon)$ dataset were the same. Note that the $WSSR$ ratios had a decrement of $\sim 1\%$ from 3rd to 4th, indicating that the probability of obtaining the better parameter sets increases with the number of draws performed by the algorithm. The quality of the adjustment can be seen in figs 6.5, where can be seen the small residues between theoretical values and data. For all datasets included on the fit graph results, see appendix D.2.

TABLE 6.11 – Global parameter set from the 4th stage (single sample).

WSSR_i	k_B (g V/cm^{3}MeV)	A_B	$\chi_0 1$	$\chi_0 2$	$\chi_0 3$	$\chi_0 4$ (MeV/cm)$^{-1}$	α (V/cm)	β (V/cm)
9.68	49.67	0.81	3.60×10^{-3}	-5.70	1.74	2.04×10^{-4}	3.83×10^{-2}	1.31×10^{-2}

Results from multiple samples from 4th stage

It was noted that for each instance of the fourth stage performed varying results due to different parameter sets obtained were observed. Consequently, an algorithm was developed to repeat this full procedure to establish a good and statistically well defined set of global fit parameters (i.e. parameters defined with central values and correspondent uncertainties). In order to have reasonable results a total of 30 instances of the fourth stage were reproduced. Notice the initial seeds of the random number generators were always adequately set at the beginning of each instance run to avoid introducing biases.

The minimum $WSSR$ was estimated for each of these 30 iterations. All these values and their associated sets of parameters were stored. The central values for the parameters are taken as those from the instance providing the lowest $WSSR$, which are the most probable parameters value estimates.

After completing the 30 iterations, the distributions of the obtained values for each P pa-

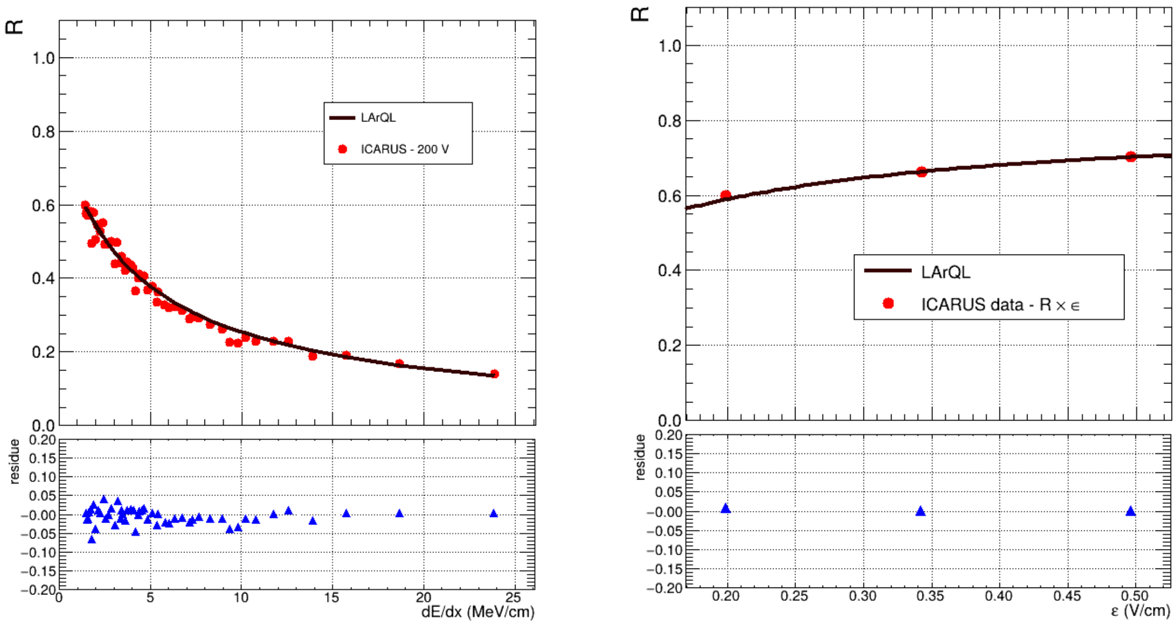

(a) ICARUS data, $\mathscr{R}(dE/dx)$, $\varepsilon = 200\,\mathrm{V/cm}$ (succeeded).

(b) ICARUS data, $\mathscr{R}(\varepsilon)$, $\frac{dE}{dx} = \mathrm{mip}$ (succeeded).

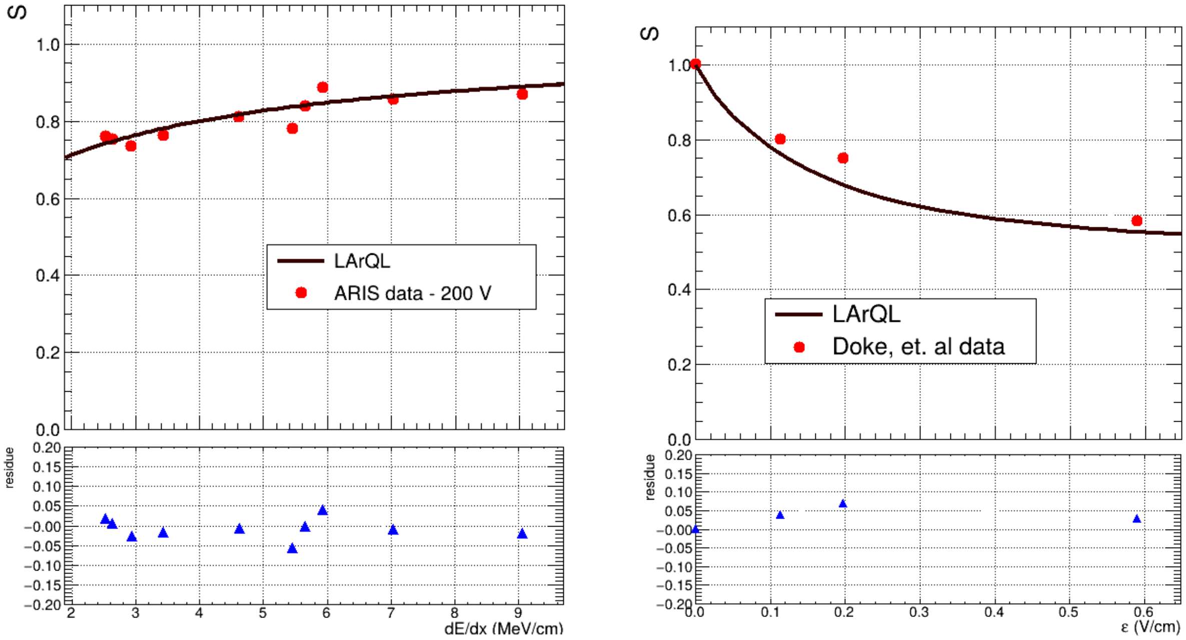

(c) ARIS data, $S(dE/dx)$, $\varepsilon = 200\,\mathrm{V/cm}$ (succeeded).

(d) Doke, *et al.*, $S(\varepsilon)$, $\frac{dE}{dx} = \mathrm{mip}$ (succeeded).

FIGURE 6.5 – Results of the fourth stage for ICARUS[5], ARIS[11], and Doke, *et al.*[6] datasets at $\varepsilon = 200\,\mathrm{V/cm}$ for ICARUS and ARIS data, and $\frac{dE}{dx} = \mathrm{mip}$, global fit (single sample).

rameter were created. The standard deviations[109] [110]:

$$\sigma = \sqrt{\frac{\sum_{j=1}^{N}\left(P_j - \overline{P}\right)^2}{N-1}} \tag{6.1}$$

were taken as metric for accessing the precision of the estimated parameters.

It is expected an estimator quality improvement with the larger possible number of entry values per histogram. However, the number of instances adopted was limited by the computational resources available. Although in fig 6.6 it is possible to notice the distributions clustering for all parameters, but with a not so clear exception for β. This parameter's distribution might be clearer if over 30 runs were conducted during the 4^{th} stage.

TABLE 6.12 – Global parameter set with uncertainties from the 4^{th} stage (selected from 30 samples and chosen by its smallest WSSR).

WSSR (sum)	k_B **(g V/cm^{3}MeV)**	A_B	$\chi_0 1$	$\chi_0 2$
9.59	49.73 ± 1.02	$(8.10 \pm 0.03) \times 10^{-1}$	$(3.60 \pm 0.24) \times 10^{-3}$	-5.68 ± 0.03

$\chi_0 3$	$\chi_0 4\ (\mathrm{MeV/cm})^{-1}$	α **(V/cm)**	β **(V/cm)**
1.74 ± 0.57	$(2.01 \pm 0.19) \times 10^{-4}$	$(3.90 \pm 0.07) \times 10^{-2}$	$(1.30 \pm 0.44) \times 10^{-2}$

As a result, the minimum WSSR ratio found was 9.59, offering an average SSR_i reduction for the datasets of $\sim 6.64\%$, which implies an overall reduction in the difference between the estimation curves and data. Tab 6.14 shows the percentage reduction of the SSR_i obtained for each dataset. All curves are better described than with the original set of parameters. Notice that most datasets had an SSR_i reduction lower than $\sim 15\%$. Fig. 6.7 shows the comparison graphs for the final global fit set of parameters. The comparison graphs for all datasets included in the fit are depicted in appendix D.3.

TABLE 6.13 – Individual SSR_i^{min} results, obtained from 4^{th} stage, global fit from 30 samples.

Dataset	**SSR**	k_B **(g V/cm^{3}MeV)**	A_B	$\chi_0 1$	$\chi_0 2$	$\chi_0 3$	$\chi_0 4\ (\mathrm{MeV/cm})^{-1}$	α **(V/cm)**	β **(V/cm)**
ICARUS 200*V*	4.09×10^{-4}	49.73	0.81	3.61×10^{-3}	-5.68	1.74	2.01×10^{-4}	3.87×10^{-2}	1.28×10^{-2}
ICARUS 350*V*	3.26×10^{-4}								
ICARUS 500*V*	5.49×10^{-4}								
ICARUS $\mathscr{R}(\varepsilon)$	2.69×10^{-5}								
Doke, *et al.*	1.44×10^{-3}								
ARIS 50*V*	9.90×10^{-4}								
ARIS 100*V*	2.34×10^{-3}								
ARIS 200*V*	6.33×10^{-4}								
ARIS 500*V*	1.42×10^{-3}								

The final SSR_i were (see tab. 6.13), for ICARUS[5] $\mathscr{R}(dE/dx)$: 4.36×10^{-4} ($\varepsilon = 200$ V/cm), 3.58×10^{-4} ($\varepsilon = 350$ V/cm), 5.50×10^{-4} ($\varepsilon = 500$ V/cm) and for $\mathscr{R}(\varepsilon)$, 2.80×10^{-5} ($dE/dx = m.i.p.$). For Doke *et al.*[6] $S(\varepsilon)$ dataset, 1.65×10^{-3}. For ARIS[11] datasets, $S(dE/dx)$: 1.06×10^{-3} ($\varepsilon = 50$ V/cm), 2.42×10^{-3} ($\varepsilon = 100$ V/cm), 6.47×10^{-4} ($\varepsilon = 200$ V/cm) and 1.44×10^{-3} ($\varepsilon = 500$ V/cm).

TABLE 6.14 – Succeeded results and percentage decrease, compared to original SSR values, of the 30th sample.

	ICARUS			
Dataset	$\mathscr{R}(dE/dx)$, $\varepsilon = 200$ kV/cm	$\mathscr{R}(dE/dx)$, $\varepsilon = 350$ kV/cm	$\mathscr{R}(dE/dx)$, $\varepsilon = 500$ kV/cm	$\mathscr{R}(\varepsilon)$
SSR_i	4.09×10^{-4}	3.26×10^{-4}	5.49×10^{-4}	2.69×10^{-5}
Result	succeeded	succeeded	succeeded	succeeded
Decrease (%)	6.31%	8.92%	5.19%	53.88%

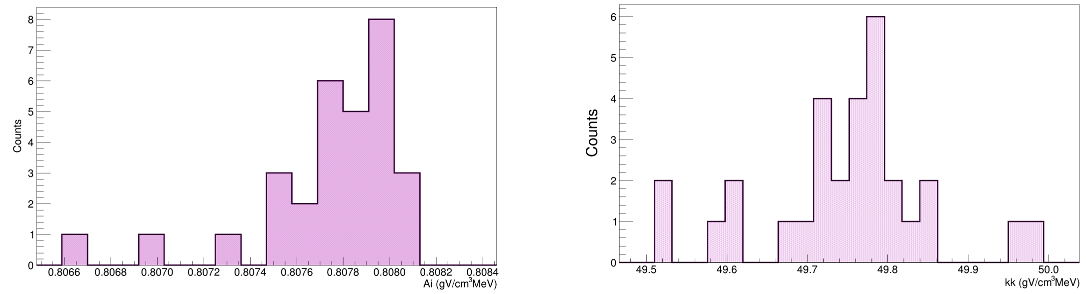

(a) Distribution of A_B

(b) Distribution of k_B

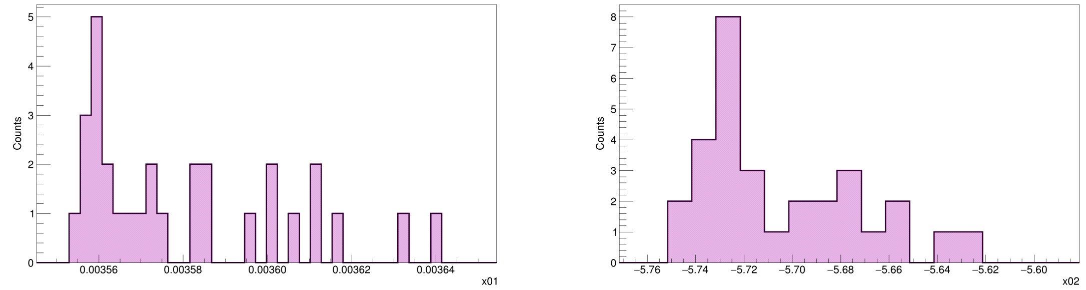

(c) Distribution of $\chi_0 1$

(d) Distribution of $\chi_0 2$

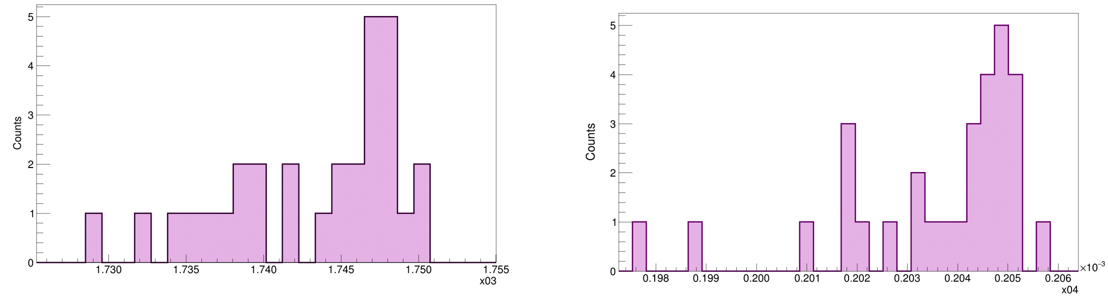

(e) Distribution of $\chi_0 3$

(f) Distribution of $\chi_0 4$

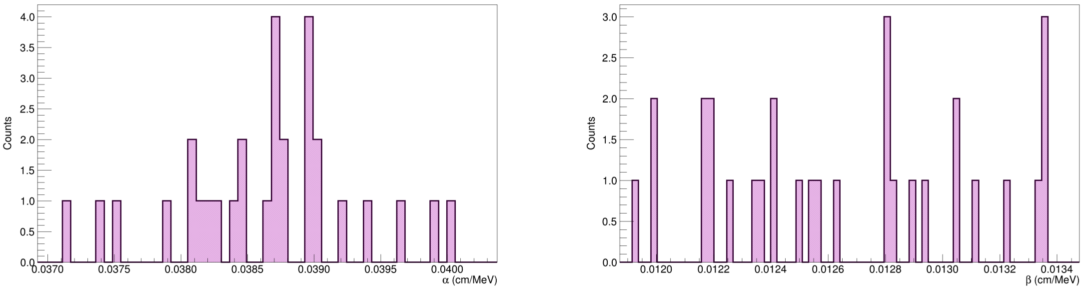

(g) Distribution of α

(h) Distribution of β

FIGURE 6.6 – Parameters distributions and their respective ranges they that tend to be clustered.

Fig 6.8 shows a compilation of all datasets used in the global fit compared to their respective LArQL estimates using the final parameters set al.l the curves have a slightly better fit to data.

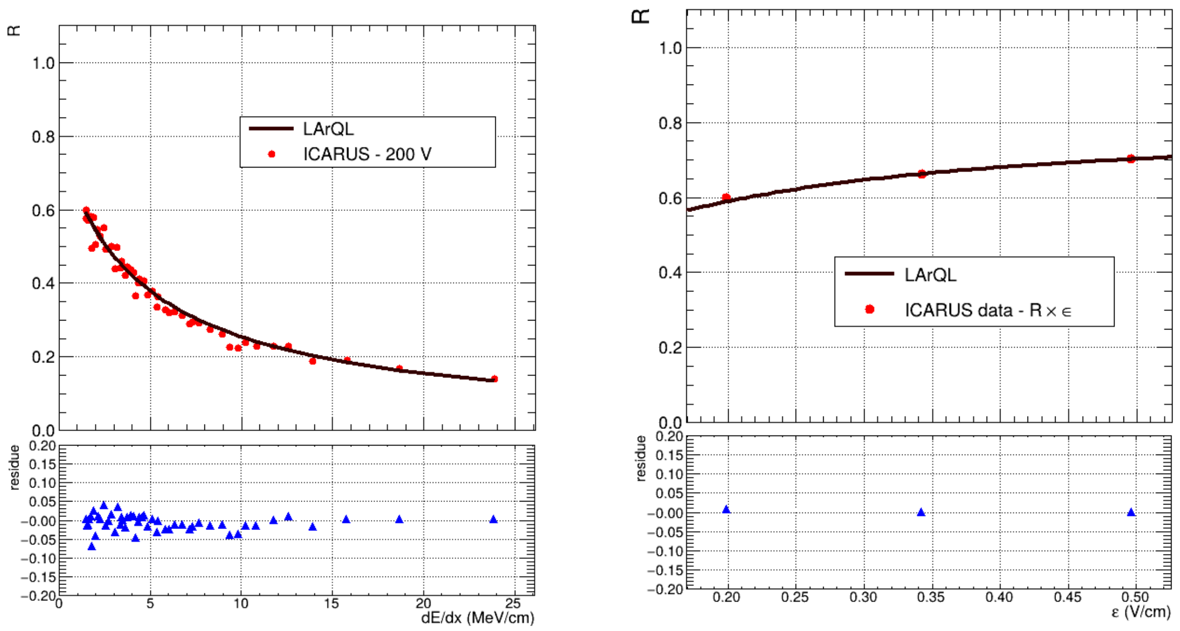

(a) ICARUS data, $\mathscr{R}\,(dE/dx)$, $\varepsilon = 200\,\mathrm{V/cm}$.

(b) ICARUS data, $\mathscr{R}\,(\varepsilon)$, $\frac{dE}{dx}$ = mip.

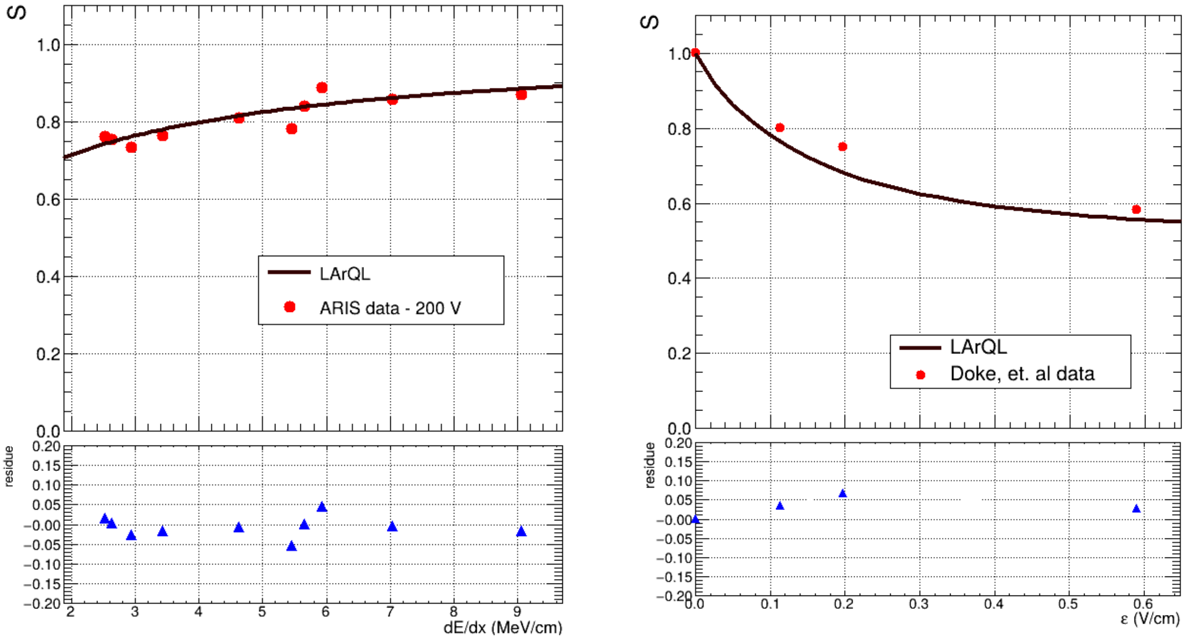

(c) ARIS data, $S\,(dE/dx)$, $\varepsilon = 200\,\mathrm{V/cm}$.

(d) Doke, *et al.*, dataset at $\frac{dE}{dx}$ = mip.

FIGURE 6.7 – Results of the fourth stage for ICARUS[5], ARIS[11], and Doke, *et al.*[6] datasets at $\varepsilon = 200\,\mathrm{V/cm}$ for ICARUS and ARIS data, and $\frac{dE}{dx}$ = mip, global fit from 30 samples.

Doke, *et al.*, $S\,(\varepsilon)$	
SSR_i	1.44×10^{-3}
Result	succeeded
Decrease (%)	15.37%

Correlation factor results

The correlations between the LArQL model parameters were also investigated. The typical procedure to do so is by means of arrangements of parameters in pairs and evaluation of their

		ARIS, $S\left(\frac{dE}{dx}\right)$		
Dataset	$\varepsilon = 50\,\mathrm{kV/cm}$	$\varepsilon = 100\,\mathrm{kV/cm}$	$\varepsilon = 200\,\mathrm{kV/cm}$	$\varepsilon = 500\,\mathrm{kV/cm}$
SSR_i	9.90×10^{-4}	2.34×10^{-3}	6.33×10^{-4}	1.42×10^{-3}
Result	succeeded	succeeded	succeeded	succeeded
Decrease (%)	10.41%	6.64%	5.10%	6.04%

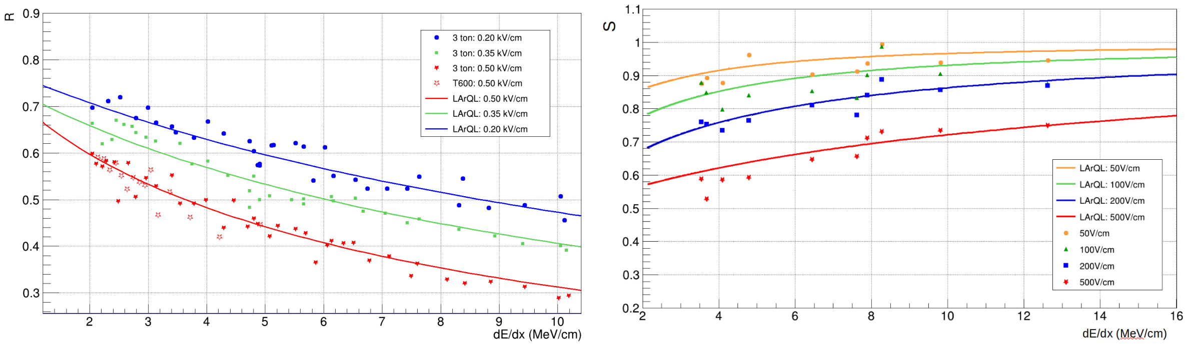

(a) ICARUS data: $\mathscr{R}(dE/dx)$.

(b) ARIS data: $S(dE/dx)$

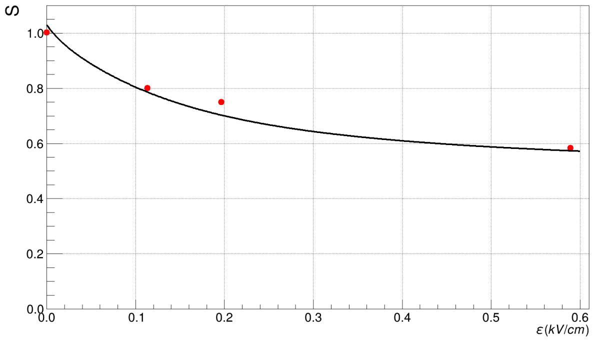

(c) The Doke, *et al.* data: $S(\varepsilon)$.

FIGURE 6.8 – The LArQL fit results for (a) ICARUS[5], (b) ARIS[7] data, and (c) the Doke, *et al.*[6] data, with the parameters from tab. 6.12.

correlation. This can be done via 2D parameter scatter plots and correlation coefficient calculations. In order, to gather a significantly large amount of reasonably constrained parameter sets these were selected by the requirement of all SSR_i values being lower than those obtained from the original LArQL parameters.

The *correlation coefficient* indicates the relationship between two variables, with possible values $-1 \leq \mathbf{c} \leq 1$. The correlation coefficient $\mathbf{c}$, also known as the *linear correlation coefficient* is:

$$\mathbf{c} = \frac{\sum_{j=1}^{N}(X_j - \overline{X})(Y_j - \overline{Y})}{\sqrt{\sum_{j=1}^{N}(X_j - \overline{X})^2 \sum_{j=1}^{N}(Y_j - \overline{Y})^2}} \tag{6.2}$$

where X and Y are the parameters. The histograms representing the correlation factor are presented in appendices F.1, F.4, F.5, F.6 and F.7 and the correlation results are listed in tab. 6.15. The dark blue regions represent low correlations between parameter values. Yellow regions represent high frequencies between parameter values. Green regions represent medium frequency.

TABLE 6.15 – Correlation factors for all parameters. The results are depicted in 4^{th} histograms.

	$k_B(gV/cm^3MeV)$	A_B	$\chi_0 1$	$\chi_0 2$	$\chi_0 3$	$\chi_0 4$ (MeV/cm)$^{-1}$	α **(V/cm)**	β **(V/cm)**
$k_B(gV/cm^3MeV)$	1	8.80×10^{-1}	-1.33×10^{-2}	-1.20×10^{-2}	1.20×10^{-2}	5.88×10^{-2}	6.94×10^{-1}	4.85×10^{-2}
A_B	8.80×10^{-1}	1	-6.96×10^{-2}	-3.02×10^{-2}	2.98×10^{-2}	7.61×10^{-2}	5.29×10^{-1}	-1.16×10^{-2}
$\chi_0 1$	-1.33×10^{-2}	-6.96×10^{-2}	1	-9.20×10^{-2}	9.49×10^{-2}	1.46×10^{-1}	3.78×10^{-2}	2.97×10^{-2}
$\chi_0 2$	-1.20×10^{-2}	-3.02×10^{-2}	-9.20×10^{-2}	1	-1	2.12×10^{-1}	3.72×10^{-2}	5.47×10^{-3}
$\chi_0 3$	1.20×10^{-2}	2.98×10^{-2}	9.49×10^{-2}	-1	1	-2.12×10^{-1}	-3.74×10^{-2}	-4.79×10^{-3}
$\chi_0 4$	5.88×10^{-2}	7.61×10^{-2}	1.46×10^{-1}	2.12×10^{-1}	-2.12×10^{-1}	1	-6.10×10^{-2}	2.56×10^{-2}
α **(V/cm)**	6.94×10^{-1}	5.29×10^{-1}	3.78×10^{-2}	3.72×10^{-2}	-3.74×10^{-2}	-6.10×10^{-2}	1	-2.06×10^{-1}
β **(V/cm)**	4.85×10^{-2}	-1.16×10^{-2}	2.97×10^{-2}	5.47×10^{-3}	-4.79×10^{-3}	2.56×10^{-2}	-2.06×10^{-1}	1

The A_B and k_B parameters strongly correlate with a value of 0.88, as shown in fig. 6.9. Notice that a well-defined and positively inclined band shows these parameter constraints. However these parameters show weak correlations with all $\chi_0 1, \chi_0 2, \chi_0 3$ and $\chi_0 4$. Figures 6.10a and 6.10b show the correlation plots for the (A_B, $\chi_0 1$) and (k_B, $\chi_0 1$) pairs as examples which indicate their 2D scattering plots aspect being very similar to a product of two independent unidimensional distributions of the parameters. Similar plots can be seen for all possible parameter pairs between these two groups in appendix F. The parameter α exhibits a moderate correlation with the parameters k_B and A_B, with correlation factors of 0.69 and 0.53, respectively, as shown in figs. 6.11a and 6.11b. Bands similar to fig. 6.9 but somewhat not as strongly constrained are observed. This is probably due to the α influence on the ε dependence of the f_{corr} factor (eq. 5.10) in the escaping electrons term. No noticeable correlation between α and any other parameter was observed. All correlation plots regarding α are available in appendix F. The β parameter seems to be uncorrelated with all parameters. This behavior was already expected considering its flat distribution in fig. 6.12, indicating no apparent impact of its value on the global fit within the adopted search range. For example, the correlation between β and $\chi_0 2$, represented by fig. 6.12, has a value of 5.47×10^{-3}. The ($\chi_0 1, \chi_0 2, \chi_0 3$, $\chi_0 4$) subset of parameters are in general quite independent of the other model parameters and do not present very strong correlation factors among themselves except the ($\chi_0 2, \chi_0 3$). However, some broad limitations are seen in their 2D scatter plots' external contour. Fig. 6.13 shows an example, while all the remaining pair plots are in appendix F. The pair ($\chi_0 2, \chi_0 3$) presents an absolute anti-correlation as can be verified through the evaluated factor and fig 6.14. In these 2D histograms, blue regions indicate low event density, green regions correspond to intermediate frequencies, and yellow regions highlight areas where the parameter distribution is more concentrated.

An overview of the stage results shown in tab. 6.16 indicates that in the first stage, which consisted of a coarse multidimensional scan of the parameters, no particular new search region of parameter values was found besides the one around the original LArQL parameters, where the SSR_i values for five out of nine datasets improved. In the second stage, where a scan was also performed with a smaller range compared to the first stage, seven individual SSR_is improved out of nine datasets. In the third stage, which consisted of 10^8 random samplings of parameter sets within the same range of values from the second stage, LArQL model regressions were performed in all datasets individually and globally. All SSR_is and the WSSR improved when

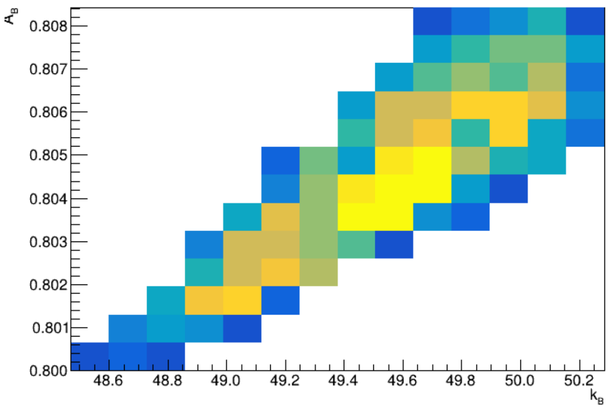

FIGURE 6.9 – $A_B \times k_B$ correlation 2D histogram.

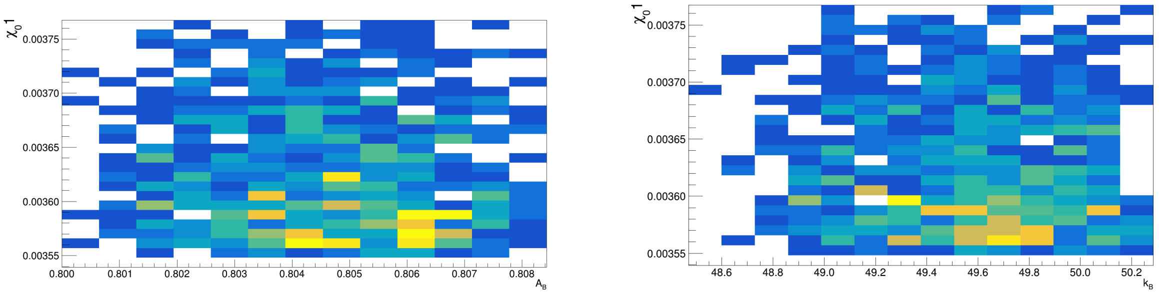

(a) $\chi_0 1 \times A_B$

(b) $\chi_0 1 \times k_B$

FIGURE 6.10 – 2D histograms for the $\chi_0 1$ parameter.

compared to the original LArQL parameters configuration. Then, the fourth stage of the analysis, which adopted the same procedures of the third stage with 10^9 samples per instance, was replicated 30 times to provide satisfactory estimates of the parameter uncertainties. This last stage also provided improved parameter sets that fit the data individually and globally. The correlation studies indicated which and how the model parameters are related. It is clearly shown that the parameters related to the ε field are interdependent while the $\chi_0(dE/dx)$ parameters are only constrained among themselves. Also, the not-so-large number of strong correlations observed supports the notion that the number of random draws adopted in the fourth stage of the fit is suitable, as many parameters are not strongly correlated to others.

6.2 Additional datasets for model comparison

This section compares the measurements provided by the experiments described in section 4.2 and the estimates obtained with the LArQL model evaluated with the parameters obtained with the global fit procedure introduced. This exercise aims to evaluate if good descriptions of new data can be achieved with this LArQL parameters configuration. Figs. 6.15, 6.16,

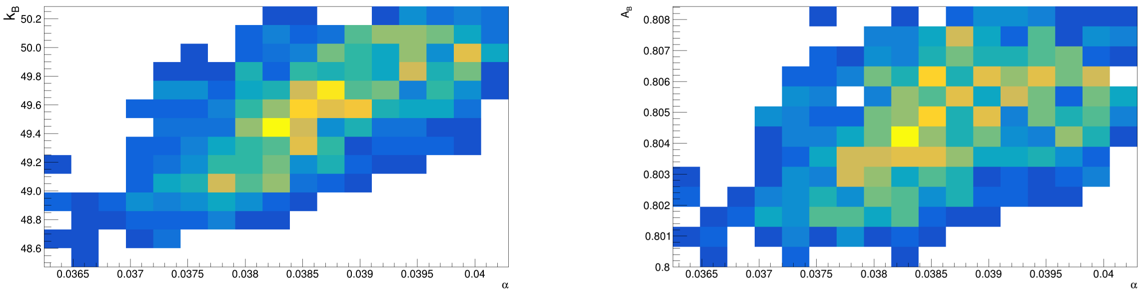

(a) $k_B \times \alpha$

(b) $A_B \times \alpha$

FIGURE 6.11 – 2D histograms for the α parameter.

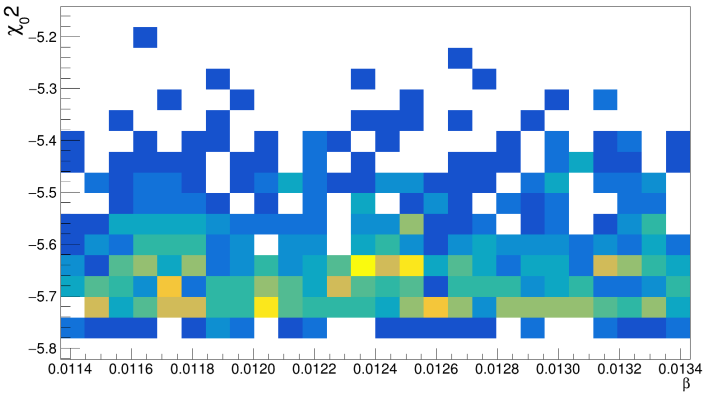

FIGURE 6.12 – $\chi_0 2 \times \beta$ correlation 2D histogram.

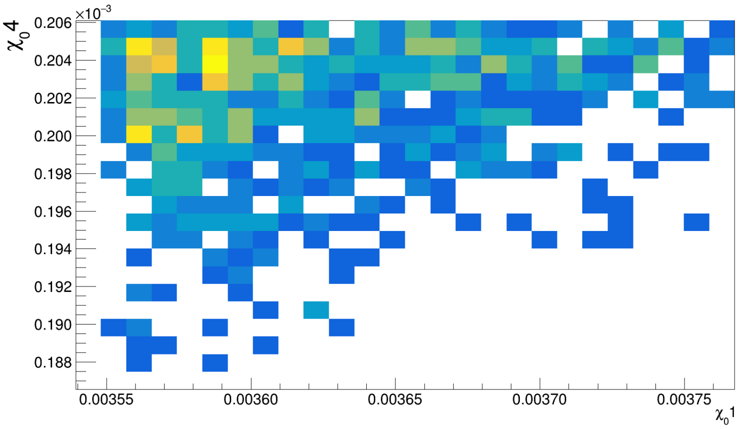

FIGURE 6.13 – $\chi_0 4 \times \chi_0 1$ correlation 2D histogram.

6.17, 6.18, 6.19a and 6.19b show the estimates for such datasets.

The MicroBooNE $dQ/dx\,(dE/dx)$ measurements[72] are exhibited in fig. 6.15 and compared to some model configurations, in which the red line represents LArQL with the parameters from tab. 5.1. The black line represents the estimation for the Birks' model alone, and the teal line, the estimations of LArQL with the parameters from tab. 6.12. The background color map in the histogram represents the density of the data points: blue regions correspond to

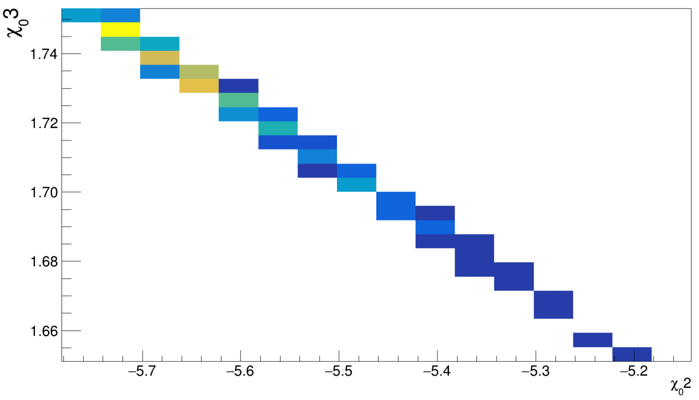

FIGURE 6.14 – $\chi_0 2 \times \chi_0 3$ correlation 2D histogram.

TABLE 6.16 – Overview of the data ranges, and procedures performed in each stage of parameter sets.

stage	Interval	$k_B\left(g\ \mathrm{V/cm^3MeV}\right)$	A_B	$\chi_0 1$	$\chi_0 2$	$\chi_0 3$	$\chi_0 4\ (\mathrm{MeV/cm})^{-1}$	$\alpha\ (\mathrm{V/cm})$	$\beta\left(\text{-}cm/MeV\right)$
1°	min	46.98	0.79	2.67×10^{-3}	-10.96	1.24	8.92×10^{-2}	0.0104	0.0035
	max	50.22	0.81	4.64×10^{-3}	-1.96	2.16	2.99×10^{-4}	0.064	0.0213
Description			Multidimensional scan of model parameters (10 steps/parameter)						
2°	min	46.98	0.79	3.54×10^{-3}	-5.96	1.65	1.82×10^{-4}	0.0342	0.0114
	max	50.22	0.81	3.76×10^{-3}	-4.96	1.75	2.06×10^{-4}	4.02×10^{-2}	0.0134
Description			Multidimensional scan of model parameters (10 steps/parameter)						
3°	min	46.98	0.79	3.54×10^{-3}	-5.96	1.65	1.82×10^{-4}	0.0342	0.0114
	max	50.22	0.81	3.76×10^{-3}	-4.96	1.75	2.06×10^{-4}	4.02×10^{-2}	0.0134
Description			Parameters randomly sampled in a homogeneous way (10^8 draws)						
4°	min	46.98	0.79	3.54×10^{-3}	-5.96	1.65	1.82×10^{-4}	0.0342	0.0114
	max	50.22	0.81	3.76×10^{-3}	-4.96	1.75	2.06×10^{-4}	4.02×10^{-2}	0.0134
Description			Parameters randomly sampled in a homogeneous way (10^9 draws)						

lower densities, green to intermediate, and yellow to high-density regions, indicating where the measured distributions are more concentrated. Note that above $dE/dx = 6$ MeV/cm, both LArQL configurations present slightly better dQ/dx descriptions of the data than the Birks' model.

In comparison to the measurements of $S(\varepsilon)$ from the ReD experiment[95] and presented in fig. 6.16, LArQL provided very adequate data descriptions in a broad range of ε field. Data were extracted and reproduced in fig. 6.16 exactly as presented in the reference listed in section 4.2. The comparison between LArQL model and the data plots are made directly. The ReD experiment presents scintillation data S_1 for different dE/dx, with the sources used being ^{137}Cs, ^{241}Am, and ^{137}Ba. Both possible LArTPC configurations were used for data acquisition in the latter, namely DP and SP. As shown in table 6.18, the SSR_i values ranged between 2.59×10^{-3} and 1.01×10^{-6}.

A comparison made with S_1 and S_2 data from ANKOK prototype (Washimi, *et al.*)[10] can be seen in fig. 6.17, where the black curve represents the LArQL estimates for $S(\varepsilon)$ and the red dots, the S_1 measurements. The magenta line represents the LArQL estimatives for $S_2(\varepsilon)$ and the green full triangles represent the S_2 measurements. Note that between $\varepsilon = 0$ kV/cm to $\varepsilon = 1000$ kV/cm, the LArQL model also provides satisfactory estimates for light and charge

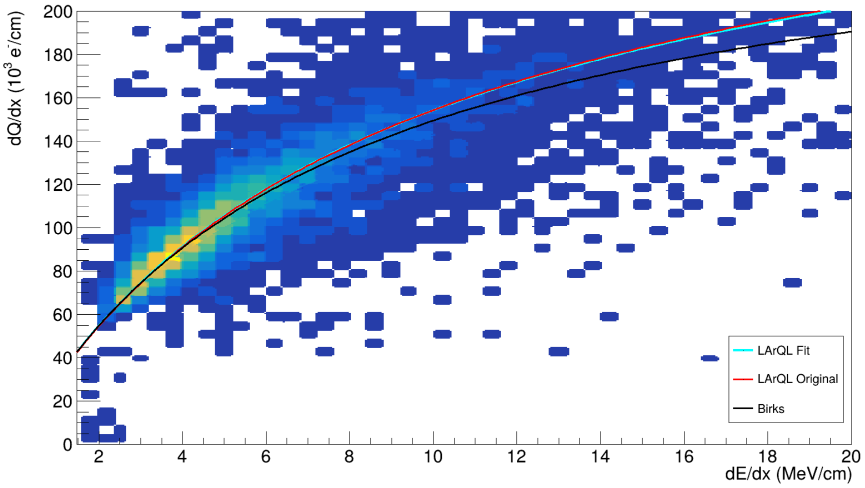

FIGURE 6.15 – LArQL fit (teal line) results for MicroBooNE $dQ/dx(dE/dx)$ data[72] compared to Birks' model (black line) and LArQL with the parameters from tab. 5.1 (red line).

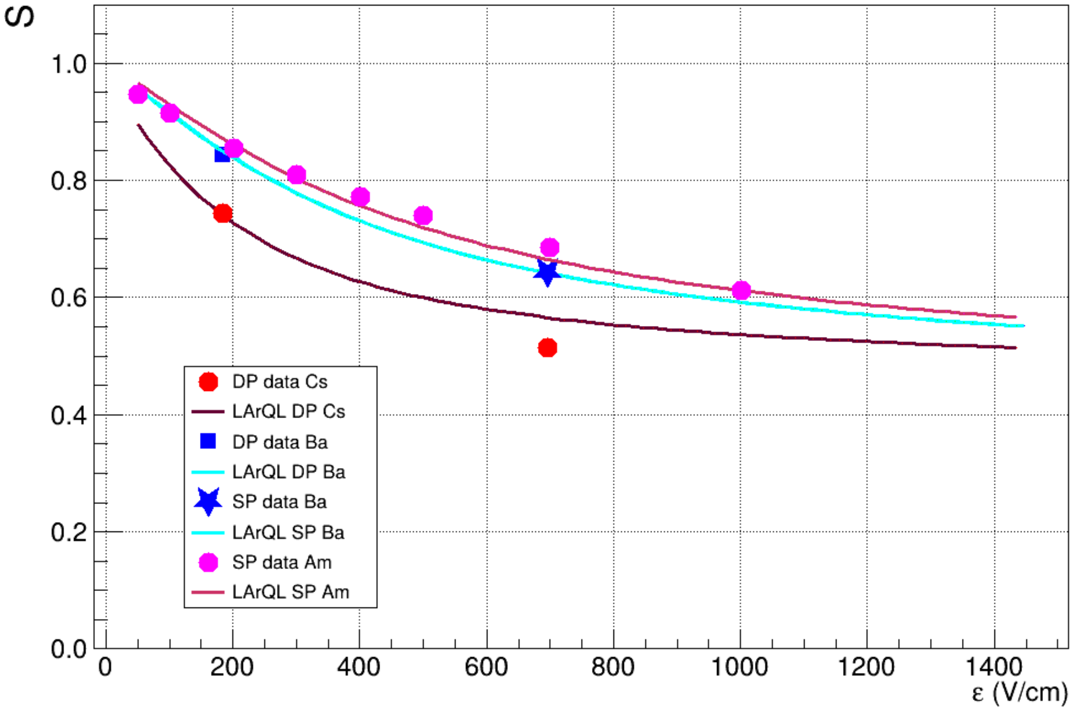

FIGURE 6.16 – Fit results for ReD data[11]. The pink curve represents the LArQL estimates for the SP LArTPC, with a ^{241}Am source, and magenta dots represent the data. The teal curve represents both LArQL for DP and SP LArTPC with a ^{137}Ba source. The blue full squares represent the DP LArTPC data and the stars, the SP LArTPC data. The dark red curve represents the LArQL for DP LArTPC with an ^{137}Cs source, and the red dots, the data.

data with small residuals.

It was also performed a comparison between LArQL and another independent ARIS dataset[11], which was not included in the original LArQL work, and also in the global fit. Figure 6.18 shows the ratio between the scintillation measurement at $\varepsilon = 0$ V/cm for different dE/dx values divided by the average of all measured values ($\bar{S}_0$). These were measure-

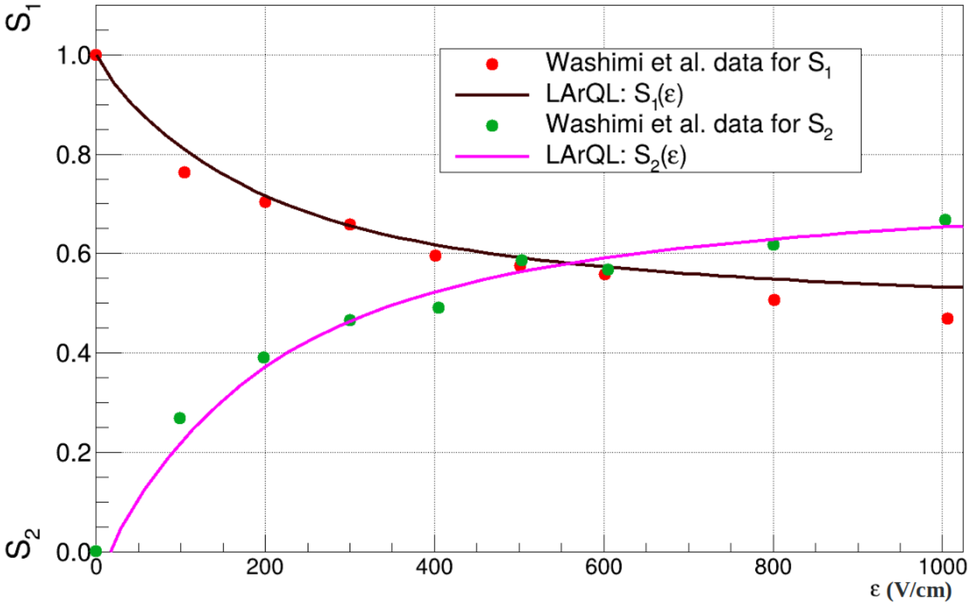

FIGURE 6.17 – Fit results for Washimi *et al.* (ANKOK prototype) data[10]. The blue curve represents the LArQL estimatives for $S(\varepsilon)$ and the red dots, the $S(\varepsilon)$ data, obtained from S_1 measurements. The magenta line represents the LArQL estimates for $S_2(\varepsilon)$ and the green full triangles represent the recombination data obtained from S_2 measurements.

ments with multiple radioactive sources, which allowed covering the dE/dx range from 2 to 9 MeV/cm. The equivalent LArQL calculation for these quantities was obtained for each dE/dx value, and the $\bar{S}_0$ was also estimated from the model. The Y-axis represents the relative S_0 and the X-axis, the dE/dx. Note that, with the increment of the dE/dx, the $S_0/\bar{S}_0$ ratio increases. This behavior was also observed by the ARIS authors[11], but performing a simple straight line fit while it is a prediction from LArQL. The parameters obtained in this work provided SSR results of ~ 0.012.

LArQL comparisons plots with the $\mathscr{R}$ measurements from the Aprile *et al.*[8] and Scalettar *et al.*[9] were made, represented by figs. 6.19a and 6.19b, respectively. These are earlier measurements of this kind, and although their dependence on the ε field follows the expected general trends, a good agreement is not found. According to[5], it is attributed a 7% common systematic error to all Aprile *et al* data points and this is not enough to account for the differences observed concerning LArQL calculations. Regarding Scalettar *et al* data, systematic negative residues are also obtained. This can probably be partially attributed to an error of ±0.02 fC for electron data, according to[5]. More details are needed for a fair comparison to be made with these two samples. Further investigation is also needed to understand why these datasets differ as much from the newer datasets, and not only from LArQL. If this is done at some point, then it should be possible to include these datasets in future fit procedures if a more elaborate regression model including systematics effects is developed. Figure 6.19a presents an SSR of 0.1. In the case of fig. 6.19b, note that below $\varepsilon = 800$ V/cm, the model provides estimations for the data, with an offset too.

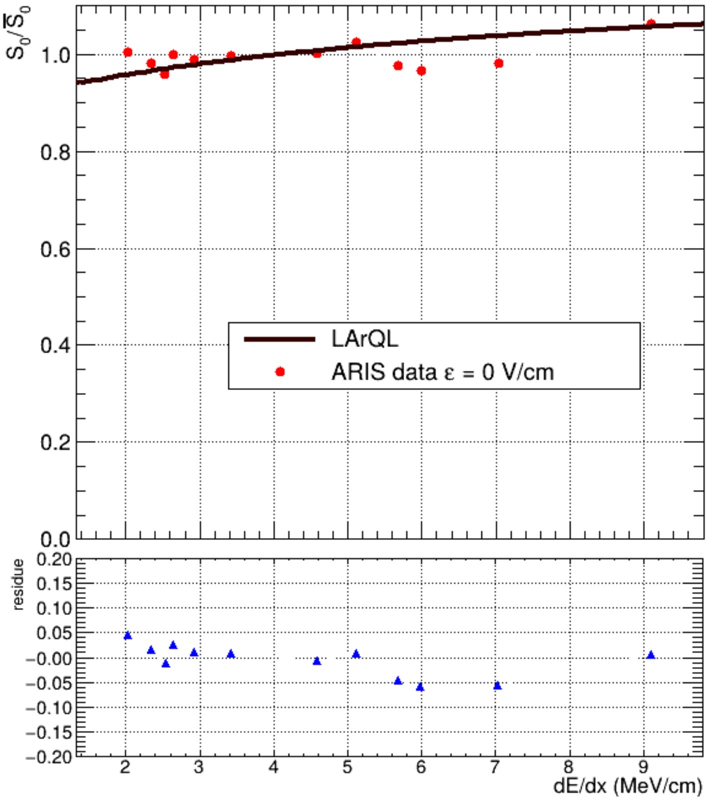

FIGURE 6.18 – Fit results for ARIS data[7], $\varepsilon = 0$ kV/cm. The blue curve represents the LArQL estimates, and the red dots represent the $\frac{S_0}{\bar{S}_0}\left(\frac{dE}{dx}\right)$ data. The light green triangles indicate the residuals between the data and theoretical values.

TABLE 6.17 – SSR results for datasets not included in the fit.

	Scalettar, et al.	**ARIS $\varepsilon = 0$ kV/cm**	**ANKOK prototype $S_2(\varepsilon)$**	**ANKOK prototype $S_1(\varepsilon)$**	**Aprile, et al.**
SSR	2.53×10^0	1.24×10^{-2}	1.05×10^0	3.45×10^{-1}	1.04×10^{-1}

TABLE 6.18 – SSR results for the ReD datasets, not included in the fit.

	ReD-DP Cs source	**ReD-DP Ba source**	**ReD-SP Ba source**	**ReD-SP Am source**
SSR	2.59×10^{-3}	3.30×10^{-5}	1.01×10^{-6}	1.79×10^{-3}

The SSR results for the datasets utilized in this section are exhibited in tab. 6.17, and 6.18 for the ReD datasets. In this section, comparisons were conducted with the datasets described in Section 4.2. As demonstrated by the plots presented throughout this section, datasets not employed on the fitting procedure are adequately described by the LArQL model. This agreement suggests that these datasets could potentially be incorporated into future fitting workflows. However, such integration was not pursued in this study due to limitations in available computational resources.

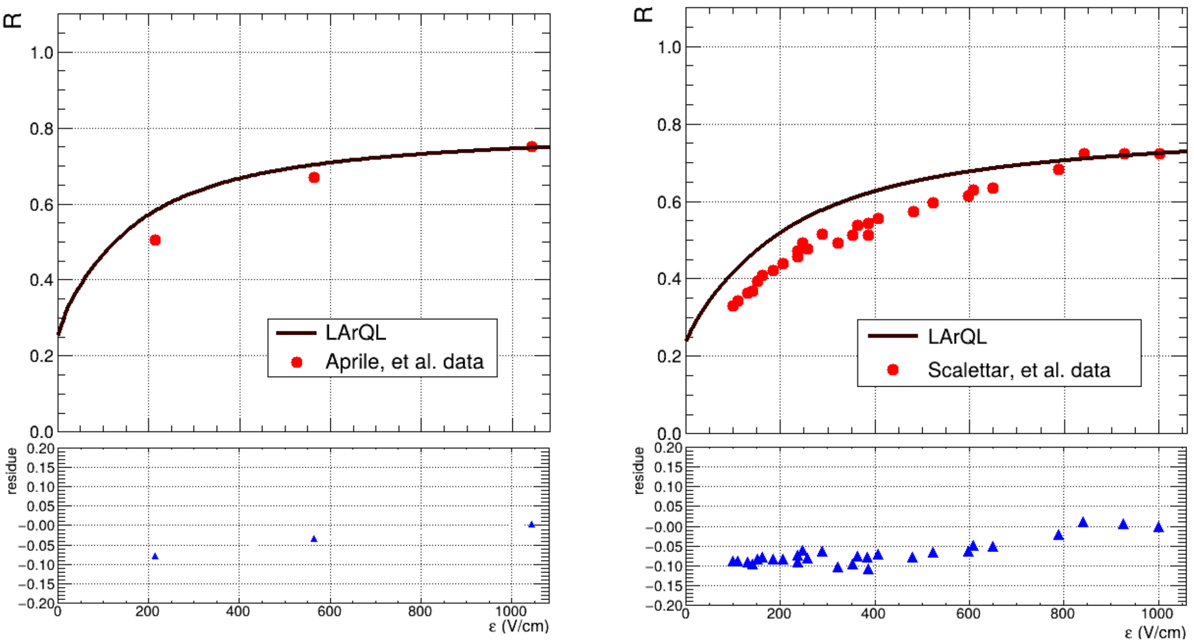

(a) Results for Aprile *et al.*[8] data.

(b) Results for[9]

FIGURE 6.19 – Comparison of LArQL estimates (dark maroon curves) and experimental data (red dots) from Aprile *et al.*[8], with an 976 keV e^- source, and Scalettar *et al.*, with an 364 keV e^- source[9]. The blue triangles represent the residuals.

7 Conclusions

The study aimed at improving the correlated evaluation of L and Q production as a function of the applied electric field ε and the charge particle energy deposited per path unit dE/dx in LAr was developed. For it, the phenomenological LArQL model was used as it provides an anticorrelation between light and charge yields for ε fields varying between 0 and 750 $\mathrm{V/cm}$ and dE/dx ranging from 2 to 40 $\mathrm{MeV/cm}$. This model relies on the Birks' term for charge production, and an additional term takes into account the escaping electrons' contribution. It generalizes the model for lower fields (down to a few V/cm) and yields a continuous description for both charge and scintillation light. The model contains 8 parameters. Two regard the Birks' term formula, four are related to the parametrization of the light yield curve as a function of dE/dx at null field, accounting for escaping electrons, and two free parameters from the exponential correction factor, which generalizes the escaping electrons term according to the ε field.

In this work, a literature review was conducted, which involved understanding and describing the experiments of interest, their collected data and particular models used in the respective fit procedure for each experiment. The first part of the work was divided into two main steps. The first step consisted on the review of the 9 datasets, published between 1988 and 2021, and which were used in the LArQL global fit developed for this dissertation. The second step of the review involved curating 9 new datasets of scintillation light and ionization charge measurements from LArTPC experiments, from papers published between 1982 and 2019. Similarly to the experiments whose data were used in the fit, the TPCs and models employed for data collection and posterior analysis were also described. In all the analyses presented in these papers no dedicated attempt to correlate data from different experiments within the range of interest for LArQL has been discussed thoroughly.

The first part of the work focused on developing and refining the global fit procedures for the LArQL model, starting from the parameter sets presented in the work of Marinho *et al.* [4]. The ROOT framework was used for data handling, visualization and comparison as for the implementation of all functionalities necessary for the fit procedures. This part was carried out in four stages: The first two involved multidimensional parameters scans for determining their searching ranges. These were finally updated as the results from the second phase improved upon the previous one. These studies indicated only one region on the vicinity of the original parameters used in LArQL as adequate for the search of a satisfactory single set of parameters for the model to describe all datasets simultaneously. This means the possibility for reduction of all SSR_i with respect to their corresponding values from the reference configuration and minimization of the $WSSR$. The third and fourth stages consisted of the actual minimization where independent random samplings of the parameters values were performed and the set of parameters giving the lowest $WSSR$ was taken as the most probable, according with the range results from second stage. The third stage served as a test to fine tune the number of iterations needed to achieve finer estimates and the fourth allowed the establishment of the final values for the parameters and their correspondent uncertainties. The parameters found were those listed in table 6.12. This was the first time the LArQL parameters were fixed through a statistical method. The parameters found were 49.73 ± 1.02 for A_B, $(8.10 \pm 0.03) \times 10^{-1}$ for k_B, $(3.60 \pm 0.24) \times 10^{-3}$ for $\chi_0 1$, $(-5.68 \pm 0.33) \times 10^{-2}$ for $\chi_0 2$, 1.74 ± 0.57 for $\chi_0 3$, $(2.01 \pm 0.19) \times 10^{-4}$ for $\chi_0 4$, $(3.90 \pm 0.07) \times 10^{-2}$ for α, $(1.30 \pm 0.44) \times 10^{-2}$ for β.

The second part of this research consisted of comparing LArQL's predictions with datasets not included in the fit to assess the robustness of the optimization. It was also plotted the datasets included in the fit to verify the quality of the fit. It was concluded that the LArQL model provides reliable estimates for different experiments, as literature indicates that each experiment was previously fitted with distinct corrections to the Birks' model.

Correlations between the parameters were also studied and only four pairs of parameters indicated strong interdependence. The results showed that the parameters A_B and k_B from Birks' term have a correlation factor of 8.8×10^{-1}, α from the correction factor correlates with A_B and k_B, with values 6.9×10^{-1} and 5.3×10^{-1}, respectively. The other values pointed to weak correlation factors, below 5×10^{-1}.

The results indicate a notable improvement in LArQL's ability to estimate light and charge data compared to the original parameters from Marinho *et al.* [4], with an average SSR decrease of approximately 6.64%. Datasets not included in the fit also demonstrated a good agreement with the model's estimations using the new parameters, suggesting the potential inclusion of these and other datasets, if available, in future fitting procedures.

References

1 ACCIARRI, R et al. Design and construction of the MicroBooNE detector. **Journal of Instrumentation**, IOP Publishing, v. 12, n. 02, p02017, Feb. 2017. DOI: `10.1088/1748-0221/12/02/P02017`.

2 ABI, B et al. Volume IV. The DUNE far detector single-phase technology. **Journal of Instrumentation**, IOP Publishing, v. 15, n. 08, t08010, 2020. DOI: `10.1088/1748-0221/15/08/T08010`.

3 ABI, B et al. **The DUNE Far Detector Interim Design Report, Volume 2: Single-Phase Module**. [S.l.], 2018. Available at: https://arxiv.org/abs/1807.10327. Accessed on: 3 Jun. 2023.

4 MARINHO, F et al. LArQL: a phenomenological model for treating light and charge generation in liquid argon. **Journal of Instrumentation**, IOP Publishing, v. 17, n. 07, p. c07009, 2022. DOI: `10.1088/1748-0221/17/07/C07009`.

5 AMORUSO, S et al. Study of electron recombination in liquid argon with the ICARUS TPC. **Nuclear Instruments and Methods in Physics Research Section A: Accelerators, Spectrometers, Detectors and Associated Equipment**, Elsevier, v. 523, n. 3, p. 275–286, 2004. DOI: `10.1016/j.nima.2003.11.423`.

6 DOKE, T et al. Absolute scintillation yields in liquid argon and xenon for various particles. **Japanese journal of applied physics**, IOP Publishing, v. 41, 3R, p. 1538, 2002. DOI: `10.1143/JJAP.41.1538`.

7 AGNES, P et al. Measurement of the liquid argon energy response to nuclear and electronic recoils. **Physical Review D**, APS, v. 97, n. 11, p. 112005, 2018. DOI: `10.1103/PhysRevD.97.112005`.

8 APRILE, E et al. Energy resolution studies of liquid argon ionization detectors. **Nuclear Instruments and Methods in Physics Research Section A: Accelerators, Spectrometers, Detectors and Associated Equipment**, Elsevier, v. 261, n. 3, p. 519–526, 1987. DOI: `10.1016/0168-9002(87)90362-7`.

9 SCALETTAR, R et al. Critical test of geminate recombination in liquid argon. **Physical Review A**, APS, v. 25, n. 4, p. 2419, 1982. DOI: `10.1103/PhysRevA.25.2419`.

10 WASHIMI, T et al. Study of the low-energy ER/NR discrimination and its electric-field dependence with liquid argon. **Journal of Instrumentation**, IOP Publishing, v. 13, n. 02, p. c02026, 2018. DOI: `10.1088/1748-0221/13/02/C02026`.

11 AGNES, P et al. Performance of the ReD TPC, a novel double-phase LAr detector with silicon photomultiplier readout. **The European Physical Journal C**, Springer, v. 81, n. 11, p. 1–19, 2021. DOI: `10.1140/epjc/s10052-021-09801-6`.

12 BECQUEREL, AH On Radioactivity, a New Property of Matter. **Nobel Lecture**, 1903. Available at: https://www.nobelprize.org/prizes/physics/1903/becquerel/lecture. Accessed on: 11 Feb. 2025.

13 CURIE, M **Radium and the New Concepts in Chemistry**. [S.l.: s.n.], 1903. Nobel Lecture. Available at: https://www.nobelprize.org/prizes/physics/1903/marie-curie/lecture/. Accessed on: 11 Feb. 2025.

14 THOMSON, JJ Carriers of negative electricity. **Nobel Lecture, December**, v. 11, n. 1906, p. 1901–1921, 1906. Available at: https://www.nobelprize.org/prizes/physics/1906/thomson/lecture/. Accessed on: 11 Feb. 2025.

15 RUTHERFORD, E **The Chemical Nature of the Alpha Particles from Radioactive Substances**. [S.l.: s.n.], 1908. Nobel Lecture. Available at: https://www.nobelprize.org/prizes/chemistry/1908/rutherford/lecture/. Accessed: 2025-02-11.

16 CURIE, I; JOLIOT, F Un nouveau type de radioactivité. **Comptes rendus des seances de l'Academie des sciences (CRAS)**, v. 198, p. 254–256, 1934. Available at: https://www.nobelprize.org/prizes/chemistry/1935/joliot-curie/lecture/. Accessed on: 18 Nov. 2024.

17 ECKER, G James Chadwick: ahead of his time. **arXiv preprint arXiv:2007.06926**, 2020. DOI: `10.48550/arXiv.2007.06926`.

18 PAULI, W Pauli letter collection: letter to Lise Meitner. Available at: https://cds.cern.ch/record/83282. Accessed on: 18 Nov. 2024. [S.l.].

19 FERMI, E Tentativo di una teoria dei raggi β. **Il Nuovo Cimento (1924-1942)**, Springer, v. 11, n. 1, p. 1–19, 1934. DOI: `10.1007/BF02959820`.

20 REINES, F The neutrino: From poltergeist to particle. **Reviews of Modern Physics**, APS, v. 68, n. 2, p. 317, 1996. DOI: `10.1103/RevModPhys.68.317`.

21 DANBY, G et al. Observation of high-energy neutrino reactions and the existence of two kinds of neutrinos. **Physical Review Letters**, APS, v. 9, n. 1, p. 36, 1962. DOI: `10.1103/PhysRevLett.9.36`.

22 NOBEL PRIZE OUTREACH AB **The hunt for the muon neutrino**. [S.l.: s.n.], 2024. Available at: https://www.nobelprize.org/prizes/physics/1988/9557-the-hunt-for-the-muon-neutrino/. Accessed on: 5 Nov. 2024.

23 PERL, ML et al. Evidence for anomalous lepton production in e+- e- annihilation. **Physical Review Letters**, APS, v. 35, n. 22, p. 1489, 1975. DOI: `10.1103/PhysRevLett.35.1489`.

24 DONUT COLLABORATION et al. A first measurement of the interaction cross-section of the tau neutrino. **arXiv preprint arXiv:0711.0728**, 2007. DOI: `10.1103/PhysRevD.78.052002`.

25 PATZAK, T First direct observation of the tau neutrino. **Europhysics News**, EDP Sciences, v. 32, n. 2, p. 56–57, 2001. DOI: `10.1051/epn:2001205`.

26 THOMSON, M **Modern particle physics**. [S.l.]: Cambridge University Press, 2013.

27 FUKUDA, Y et al. Measurements of the solar neutrino flux from Super-Kamiokande’s first 300 days. **Physical Review Letters**, v. 81, n. 6, p. 1158, 1998. DOI: `10.1103/PhysRevLett.81.1158`.

28 AHMAD, QR et al. Direct evidence for neutrino flavor transformation from neutral-current interactions in the Sudbury Neutrino Observatory. **Physical Review Letters**, APS, v. 89, n. 1, p. 011301, 2002. DOI: `10.1103/PhysRevLett.89.011301`.

29 WU, CS et al. Experimental test of parity conservation in beta decay. **Physical review**, APS, v. 105, n. 4, p. 1413, 1957. DOI: `10.1103/PhysRev.105.1413`.

30 ZUBER, K **Neutrino physics**. [S.l.]: Taylor & Francis, 2020.

31 GERSHON, T; NIR, Y CP Violation in the Quark Sector. Particle Data Group, 2023. Available at: https://pdg.lbl.gov/2024/web/viewer.html?file=../reviews/rpp2024-rev-cp-violation.pdf. Accessed on: 18 Nov. 2024.

32 CHRISTENSON, JH et al. Evidence for the 2 π Decay of the K 2 0 Meson. **Physical Review Letters**, APS, v. 13, n. 4, p. 138, 1964. DOI: `10.1103/PhysRevLett.13.138`.

33 BARGER, V; MARFATIA, D; WHISNANT, K **The physics of neutrinos**. [S.l.]: Princeton University Press, 2012.

34 ULLMAN, J Measurement of the solar electron neutrino flux with the Homestake chlorine detector. **The Astrophysical Journal**, v. 496, p. 505–526, 1998. DOI: `10.1086/305343`.

35 PEÑA-GARAY, C; SERENELLI, AM Solar neutrinos and the solar composition problem. **arXiv preprint**, v. 0811.2424, 2008. Available at: https://arxiv.org/abs/0811.2424. Accessed on: 5 Nov 2024.

36 CLEVELAND, BT et al. Measurement of the Solar Electron Neutrino Flux with the Homestake Chlorine Detector. **The Astrophysical Journal**, v. 496, n. 1, p. 505, Mar. 1998. DOI: `10.1086/305343`. Available from: <`https://dx.doi.org/10.1086/305343`>.

37 SAGE COLLABORATION Measurement of the solar neutrino capture rate with gallium metal. **arXiv preprint astro-ph/9907113**, 1999. DOI: `10.1103/PhysRevC.60.055801`.

38 (PARTICLE DATA GROUP), SN et al. Neutrino Mixing. **Physical Review D**, v. 110, p. 030001, 2024. DOI: `10.1103/PhysRevD.110.030001`.

39 ALTMANN, M et al. Complete results for five years of GNO solar neutrino observations. **Physics Letters B**, v. 616, n. 3-4, p. 174–190, 2005. DOI: `10.1016/j.physletb.2005.04.068`.

40 VIGNAUD, D The GALLEX solar neutrino experiment. **Nuclear Physics B-Proceedings Supplements**, Elsevier, v. 60, n. 3, p. 20–29, 1998. DOI: `10.1016/S0920-5632(97)00498-2`.

41 ________. The Gallium Solar Neutrino Experiment GALLEX. In: NUCLEOSYNTHESIS and Its Implications on Nuclear and Particle Physics. Heidelberg: D. Reidel Publishing Company, 1986. Accessed on: 11 Oct 2024. P. 453–461. Available from: <`https://s3.cern.ch/inspire-prod-files-4/4edd15ac774248e58d6d3e1e77d0ed3a`>.

42 THE UNIVERSITY OF TOKYO **35 Years after the Detection of SN1987A Neutrinos**. Hida-City: [s.n.], 2022. Available at: https://www-sk.icrr.u-tokyo.ac.jp/en/news/detail/324. Accessed on: 21 Nov. 2024.

43 HIRATA, K et al. Observation of a neutrino burst from the supernova SN1987A. **Physical Review Letters**, APS, v. 58, n. 14, p. 1490, 1987. DOI: `10.1103/PhysRevLett.58.1490`.

44 HIRATA, KS et al. Observation of ^{8}B solar neutrinos in the Kamiokande-II detector. **Physical Review Letters**, v. 63, n. 1, p. 16, 1989. DOI: `10.1103/PhysRevLett.63.16`.

45 THE NOBEL PRIZE ORGANIZATION **The Nobel Prize in Physics 2002: Summary**. Amsterdam: [s.n.], 2002. Available at: https://www.nobelprize.org/prizes/physics/2002/summary/. Accessed on: 21 Nov. 2024.

46 OKUMURA, K Highlights from Super-Kamiokande. In: EDP SCIENCES. EPJ Web of Conferences. [S.l.: s.n.], 2016. v. 126, p. 02023. DOI: `10.1051/epjconf/201612602023`.

47 SUDBURY NEUTRINO OBSERVATORY **SNO Projects**. Ontario, CA: [s.n.], 2024. Available at: https://sno.phy.queensu.ca/. Accessed on: 15 Nov. 2024.

48 AHARMIM, B et al. Combined analysis of all three phases of solar neutrino data from the Sudbury Neutrino Observatory. **Physical Review C—Nuclear Physics**, APS, v. 88, n. 2, p. 025501, 2013. DOI: `10.1103/PhysRevC.88.025501`.

49 SNO COLLABORATION Electron Energy Spectra, Fluxes, and Day-Night Asymmetries of 8B Solar Neutrinos from the 391-Day Salt Phase SNO Data Set. Ithaca, NY, 2005. Available at: https://arxiv.org/abs/nucl-ex/0502021. Accessed on: 15 Nov. 2024.

50 MAKI, Z; NAKAGAWA, M; SAKATA, S Remarks on the unified model of elementary particles. **Progress of Theoretical Physics**, Oxford University Press, v. 28, n. 5, p. 870–880, 1962. DOI: `10.1143/PTP.28.870`.

51 PONTECORVO, B Neutrino Experiments and the Problem of Conservation of Leptonic Charge. **Zh. Eksp. Teor. Fiz.**, v. 53, p. 1717–1725, 1967.

52 TANABASHI, M et al. Review of Particle Physics. **Phys. Rev. D**, v. 98, n. 3, p. 030001, 2018. DOI: `10.1103/PhysRevD.98.030001`.

53 GIUNTI, C; KIM, CW **Fundamentals of neutrino physics and astrophysics**. [S.l.]: Oxford university press, 2007.

54 AKHMEDOV, EK; SMIRNOV, AY Paradoxes of neutrino oscillations. **Physics of Atomic Nuclei**, Springer, v. 72, p. 1363–1381, 2009. DOI: `10.1134/S1063778809080122`.

55 THOMSON, M **Neutrino Oscillations**. Cambridge: [s.n.], 2009. Lecture Notes. Available at: `https://www.hep.phy.cam.ac.uk/~thomson/lectures/partIIIparticles/Handout11_2009.pdf`. Accessed on: 20 Feb. 2025.

56 ABI, B et al. Deep Underground Neutrino Experiment (DUNE), far detector technical design report, volume II: DUNE physics. **arXiv preprint arXiv:2002.03005**, 2020. DOI: `10.48550/arXiv.2002.03005`.

57 DE SALAS, PF et al. Neutrino mass ordering from oscillations and beyond: 2018 status and future prospects. **Frontiers in Astronomy and Space Sciences**, Frontiers Media SA, v. 5, p. 36, 2018. DOI: `10.3389/fspas.2018.00036`.

58 VOGEL, P; PIEPKE, A Neutrino Properties. **Physical Review D**, v. 110, n. 3, p. 341–397, 2024. Available at: https://pdg.lbl.gov/2024/reviews/rpp2024-rev-intro-neutrino-prop.pdf. Accessed on: 10 Oct. 2024.

59 DE BERNARDIS, F et al. Determining the neutrino mass hierarchy with cosmology. **Phys. Rev. D**, American Physical Society, v. 80, p. 123509, 12 Dec. 2009. DOI: `10.1103/PhysRevD.80.123509`. Available from: <`https://link.aps.org/doi/10.1103/PhysRevD.80.123509`>.

60 T2K COLLABORATION **About T2K**. Tokai: [s.n.], 2024. Available at: https://t2k-experiment.org/t2k/. Accessed on: 20 Dec. 2024.

61 NOVA COLLABORATION **NOvA Experiment Official Website**. [S.l.: s.n.], 2024. Available at: https://novaexperiment.fnal.gov/. Accessed: 2024-12-20.

62 JIĀNGMÉN UNDERGROUND NEUTRINO OBSERVATORY **Homepage**. Kaiping City: [s.n.], 2024. Available at: http://juno.ihep.cas.cn/. Accessed on: 20 Dec. 2024.

63 BAUDIS, L et al. Review of particle physics. **Progress of Theoretical and Experimental Physics**, Oxford University Press, v. 2020, n. 8, p. 083c01, 2020. DOI: `10.1093/ptep/ptaa104`.

64 PUTNAM, G Calibrating for Precision Calorimetry in LArTPCs at ICARUS and SBN. In: MDPI, 1. PHYSICAL Sciences Forum. [S.l.: s.n.], 2023. v. 8, p. 15. DOI: `10.3390/psf8010015`.

65 SCARPELLI, A ProtoDUNE and a Dual-phase LArTPC. Ithaca, NY, 2019. Available at: https://arxiv.org/pdf/1902.04780. Accessed on: 15 Nov. 2024.

66 ABI, B et al. Volume I. Introduction to DUNE. **Journal of Instrumentation**, IOP Publishing, v. 15, n. 08, t08008, 2020. DOI: `10.48550/arXiv.2002.02967`.

67 ABI, B et al. The DUNE far detector interim design report volume 1: physics, technology and strategies. Ithaca, NY, 2018. Available at: https://arxiv.org/pdf/1807.10334/. Accessed on: 20 Nov. 2023.

68 ________. The DUNE far detector interim design report, Volume 3: dual-phase module. Ithaca, NY, 2018. Available at: https://www.research.unipd.it/retrieve/e14fb26b-5d91-3de1-e053-1705fe0ac030/1807.10340.pdf. Accessed on: 20 Nov. 2023.

69 ABUD, AA et al. DUNE Phase II: Scientific Opportunities, Detector Concepts, Technological Solutions. **arXiv preprint arXiv:2408.12725**, 2024. DOI: `10.48550/arXiv.2408.12725`.

70 DUNE SCIENCE COLLABORATION Deep Underground Neutrino Experiment (DUNE): Far detector technical design report. Volume III. DUNE far detector technical coordination. **Journal of Instrumentation**, IOP Publishing, v. 15, n. 8, 2020. DOI: `10.1088/1748-0221/15/08/T08010`.

71 ________. The DUNE Far Detector Vertical Drift Technology. Technical Design Report. **Journal of Instrumentation**, IOP Publishing, v. 19, n. 8, t08004, 2024. DOI: `10.1088/1748-0221/19/08/T08004`.

72 ADAMS, C et al. Calibration of the charge and energy loss per unit length of the MicroBooNE liquid argon time projection chamber using muons and protons. **Journal of Instrumentation**, IOP Publishing, v. 15, n. 03, p03022, 2020. DOI: `10.1088/1748-0221/15/03/P03022`.

73 HITACHI, A et al. Scintillation and ionization yield for α particles and fission fragments in liquid argon. **Physical Review A**, APS, v. 35, n. 9, p. 3956, 1987. DOI: `10.1103/PhysRevA.35.3956`.

74 BRIZZOLARI, C et al. Enhancement of the X-Arapuca photon detection device for the DUNE experiment. **Journal of Instrumentation**, IOP Publishing, v. 16, n. 09, p09027, 2021. DOI: `10.1088/1748-0221/16/09/P09027`.

75 RUBBIA, C **The Liquid-Argon Time Projection Chamber: A New Concept for Neutrino Detectors**. Geneva, 1977. Available at: https://cds.cern.ch/record/117852. Accessed on: 10 Aug. 2024.

76 MAJUMDAR, K; MAVROKORIDIS, K Review of liquid argon detector technologies in the neutrino sector. **Applied Sciences**, MDPI, v. 11, n. 6, p. 2455, 2021. DOI: `10.3390/app11062455`.

77 VIEHHAUSER, G; WEIDBERG, T **Detectors in Particle Physics: A Modern Introduction**. [S.l.]: Taylor & Francis, 2024.

78 FORMAGGIO, JA; ZELLER, GP From eV to EeV: Neutrino Cross-Sections Across Energy Scales. **Reviews of Modern Physics**, American Physical Society, v. 84, n. 3, p. 1307–1341, 2013. DOI: `10.1103/RevModPhys.84.1307`.

79 SOTO OTON, JA **Scintillation light detection techniques in a 750-ton liquid argon TPC for the Deep Underground Neutrino Experiment**. 2022. PhD thesis – Centro de Investigaciones Energéticas Medioambientales y Tec.(ES).

80 SEGRETO, E Properties of liquid argon scintillation light emission. **Physical Review D**, APS, v. 103, n. 4, p. 043001, 2021. DOI: `10.1103/PhysRevD.103.043001`.

81 ABRAHAM, Y et al. Wavelength-shifting performance of polyethylene naphthalate films in a liquid argon environment. **Journal of Instrumentation**, IOP Publishing, v. 16, n. 07, p07017, 2021. DOI: `10.1088/1748-0221/16/07/P07017`.

82 PAULUCCI, L et al. A complete simulation of the X-ARAPUCA device for detection of scintillation photons. **Journal of Instrumentation**, v. 15, n. 01, p. c01047, 2020. DOI: `10.1088/1748-0221/15/01/C01047`. Available from: <`https://dx.doi.org/10.1088/1748-0221/15/01/C01047`>.

83 JONES, B et al. A measurement of the absorption of liquid argon scintillation light by dissolved nitrogen at the part-per-million level. **Journal of Instrumentation**, IOP Publishing, v. 8, n. 07, p07011, 2013. DOI: `10.1088/1748-0221/8/07/P07011`.

84 ABRATENKO, P et al. Convolutional neural network for multiple particle identification in the MicroBooNE liquid argon time projection chamber. **Physical Review D**, APS, v. 103, n. 9, p. 092003, 2021. DOI: `10.1103/PhysRevD.103.092003`.

85 DUNE SCIENCE COLLABORATION **An International Experiment for Neutrino Science**. Geneva: [s.n.], 2020. Available at: https://www.dunescience.org/. Accessed on: 23 Sep. 2024.

86 MCCONKEY, N; SBND COLLABORATION, et al. Sbnd: Status of the fermilab short-baseline near detector. In: IOP PUBLISHING, 1. JOURNAL of Physics: Conference Series. [S.l.: s.n.], 2017. v. 888, p. 012148. DOI: `10.1088/1742-6596/888/1/012148`.

87 ABI, B et al. First results on ProtoDUNE-SP liquid argon time projection chamber performance from a beam test at the CERN Neutrino Platform. **Journal of Instrumentation**, IOP Publishing, v. 15, n. 12, p12004, 2020. DOI: `10.1088/1748-0221/15/12/P12004`.

88 DOKE, T Fundamental Properties of Liquid Argon, Krypton and Xenon as Radiation Detector Media. **Portugaliae Physica**, v. 12, p. 9–48, 1981. Available at: https://www.spf.pt/magazines/Portugaliae$phy/496/article/1979/pdf.Accessedon$: $8Mar.$2023.

89 DOKE, T et al. Let dependence of scintillation yields in liquid argon. **Nuclear Instruments and Methods in Physics Research Section A: Accelerators, Spectrometers, Detectors and Associated Equipment**, Elsevier, v. 269, n. 1, p. 291–296, 1988. DOI: `10.1016/0168-9002(88)90892-3`.

90 HITACHI, A et al. Effect of ionization density on the time dependence of luminescence from liquid argon and xenon. **Physical Review B**, APS, v. 27, n. 9, p. 5279, 1983. DOI: `10.1103/PhysRevB.27.5279`.

91 HITACHI, A; DOKE, T; MOZUMDER, A Luminescence quenching in liquid argon under charged-particle impact: Relative scintillation yield at different linear energy transfers. **Physical Review B**, APS, v. 46, n. 18, p. 11463, 1992. DOI: `10.1103/PhysRevB.46.11463`.

92 CANCI, N The ICARUS T600 detector at LNGS underground laboratory. **Physics Procedia**, Elsevier, v. 37, p. 1257–1265, 2012. DOI: `10.1016/j.phpro.2012.02.466`.

93 UNITED STATES DEPARTMENT OF ENERGY OFFICE OF SCIENCE, FERMI NATIONAL ACCELERATOR LABORATORY **ICARUS Experiment: About**. Batavia, IL: [s.n.], 2017. Available at: https://icarus.fnal.gov/about/. Accessed on: 25 Sep. 2024.

94 WILSON, J et al. The LICORNE neutron source and measurements of prompt γ-rays emitted in fission. **Physics Procedia**, Elsevier, v. 59, p. 31–36, 2014. DOI: `10.1016/j.phpro.2014.10.005`.

95 AGNES, P et al. Simulation of argon response and light detection in the DarkSide-50 dual phase TPC. **Journal of Instrumentation**, IOP Publishing, v. 12, n. 10, p10015, 2017. DOI: `10.1088/1748-0221/12/10/P10015`.

96 ADAMS, C et al. Ionization electron signal processing in single phase LArTPCs. Part I. Algorithm Description and quantitative evaluation with MicroBooNE simulation. **Journal of Instrumentation**, IOP Publishing, v. 13, n. 07, p07006, 2018. DOI: `10.1088/1748-0221/13/07/P07006`.

97 CONRAD, J et al. The photomultiplier tube calibration system of the MicroBooNE experiment. **Journal of Instrumentation**, IOP Publishing, v. 10, n. 06, t06001, 2015. DOI: `10.1088/1748-0221/10/06/T06001`.

98 MALENSEK, AJ **Neutrino Beams Using the Main Injector**. Batavia, IL, 1995. Available at: https://inspirehep.net/files/f94726b4c2bf6043bbb959dd27b5175b. Accessed on: 13 Oct. 2024.

99 ABRATENKO, P **First measurement of differential cross sections for muon neutrino charged current interactions on argon with a two-proton final state in the MicroBooNE detector**. [S.l.], 2022. DOI: `10.48550/arXiv.2211.03734`.

100 KARAGIORGI, G MicroBooNE and the Road to Large Liquid Argon Neutrino Detectors. **Physics Procedia**, v. 37, p. 1319–1323, Dec. 2012. DOI: `10.1016/j.phpro.2012.02.469`.

101 RIESSELMANN, K **A Boon for Physicists: New Insights into Neutrino Interactions**. Batavia, IL: [s.n.], 2018. Available at: https://news.fnal.gov/2018/06/a-boon-for-physicists-new-insights-into-neutrino-interactions/. Accessed on: 21 Sep. 2024.

102 ACCIARRI, R et al. A study of electron recombination using highly ionizing particles in the ArgoNeuT Liquid Argon TPC. **Journal of Instrumentation**, IOP Publishing, v. 8, n. 08, p08005, 2013. DOI: `10.1088/1748-0221/8/08/P08005`.

103 KIMURA, M; TANAKA, M; YORITA, K Low Energy Response on Liquid Argon Scintillation and Ionization Process for Dark Matter Search. In: PROCEEDINGS of International Symposium on Radiation Detectors and Their Uses (ISRD2016). [S.l.: s.n.], 2016. P. 040003. Available from: <`10.7566/JPSCP.11.040003`>.

104 ________. Status and prospect of the ANKOK project: Low mass WIMP dark matter search using double phase argon detector. **Journal of Physics: Conference Series**, IOP Publishing, v. 1342, n. 1, p. 012069, Jan. 2020. DOI: `10.1088/1742-6596/1342/1/012069`. Available from: <`https://dx.doi.org/10.1088/1742-6596/1342/1/012069`>.

105 MIYAJIMA, M et al. Average energy expended per ion pair in liquid argon. **Physical Review A**, APS, v. 9, n. 3, p. 1438, 1974. DOI: `10.1103/PhysRevA.9.1438`.

106 ANTCHEVA, I et al. ROOT—A C++ framework for petabyte data storage, statistical analysis and visualization. **Computer Physics Communications**, Elsevier, v. 182, n. 6, p. 1384–1385, 2011. DOI: `10.1016/j.cpc.2011.02.008`.

107 CERN **ROOT: Data Analysis Framework**. Geneva: [s.n.], 2025. Available at: https://root.cern/about/. Accessed on: 28 Oct. 2023.

108 VUOLO, JH **Fundamentos da teoria de erros**. [S.l.]: Editora Blucher, 1996.

109 SPIEGEL, MR; SRINIVASAN, RA; SCHILLER, JJ **Schaum's outline of theory and problems of probability and statistics**. [S.l.]: Erlangga, 2000.

110 TAYLOR, JR **An Introduction to Error Analysis: The Study of Uncertainties in Physical Measurements**. [S.l.]: University Science Books, 1997.

Appendix A - First stage graphs

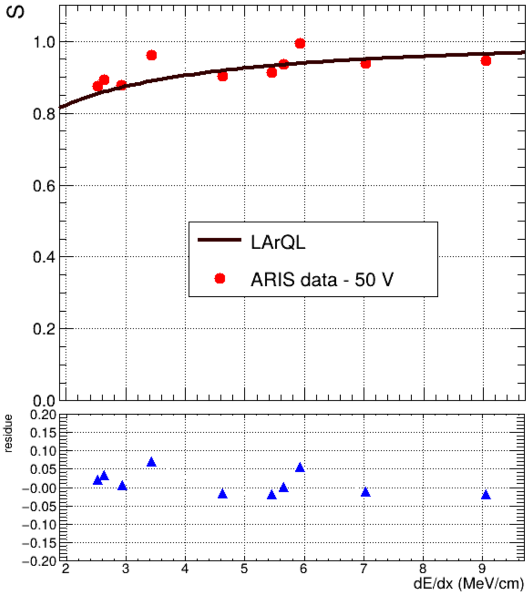

(a) ARIS data, $\varepsilon = 50\,\mathrm{V/cm}$

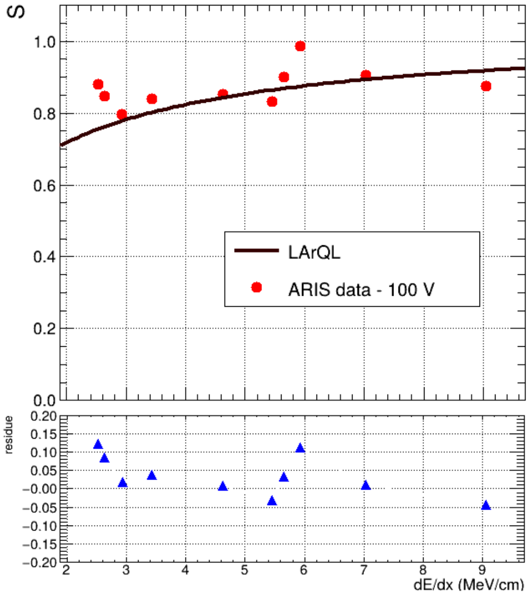

(b) ARIS data, $\varepsilon = 100\,\mathrm{V/cm}$

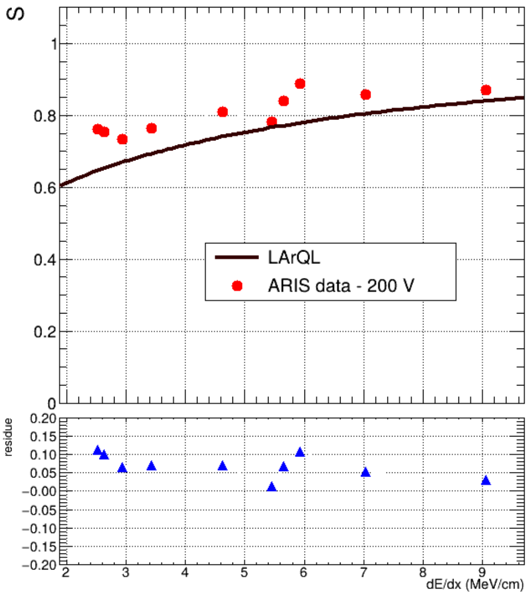

(c) ARIS data, $\varepsilon = 200\,\mathrm{V/cm}$

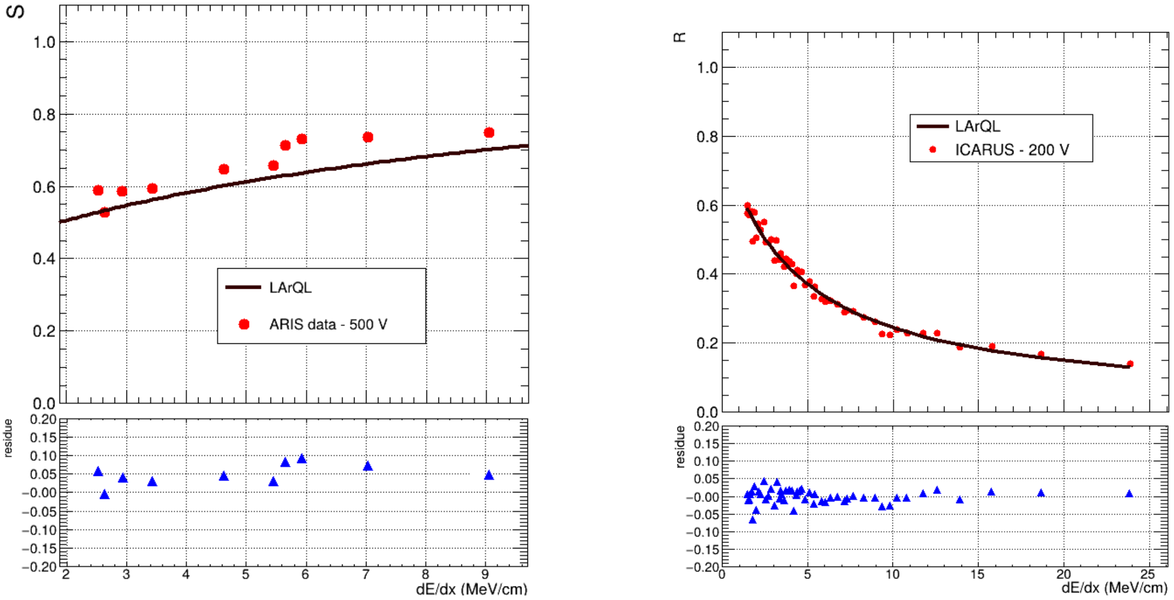

(d) ARIS data, $\varepsilon = 500\,\mathrm{V/cm}$

(e) ICARUS data, $\varepsilon = 200\,\mathrm{V/cm}$

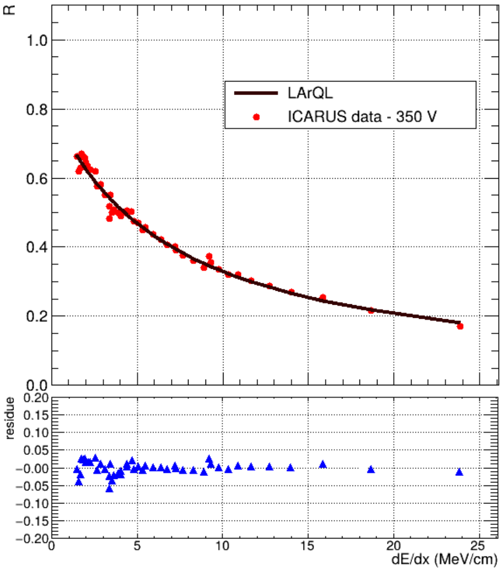

(f) ICARUS data, $\varepsilon = 350\,\mathrm{V/cm}$

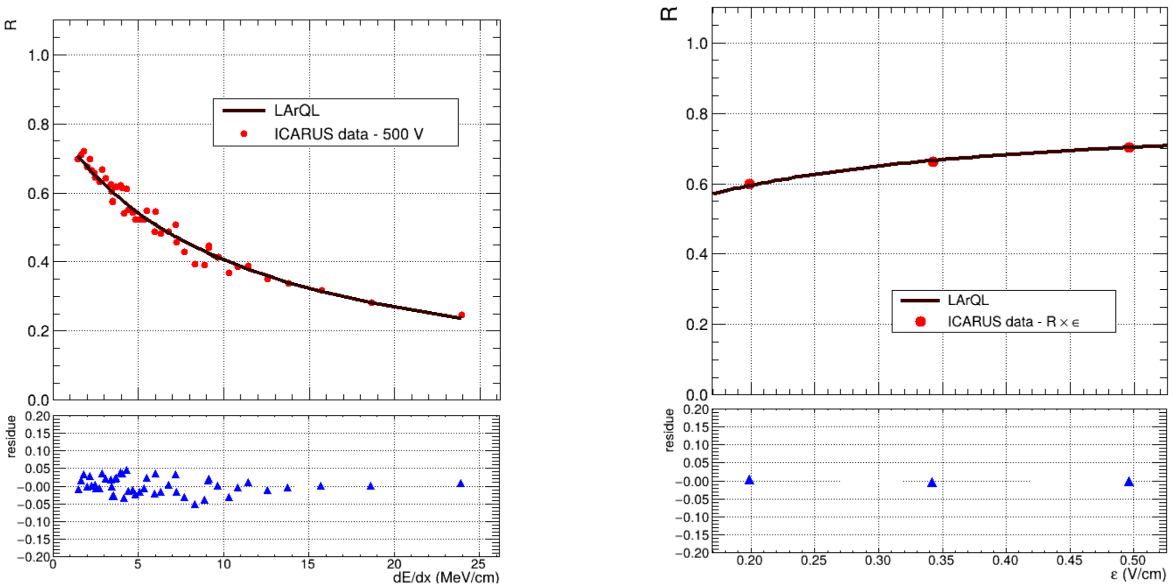

(g) ICARUS data, $\varepsilon = 500\,\mathrm{V/cm}$

(h) ICARUS data, $\frac{dE}{dx} = \mathrm{mip}$

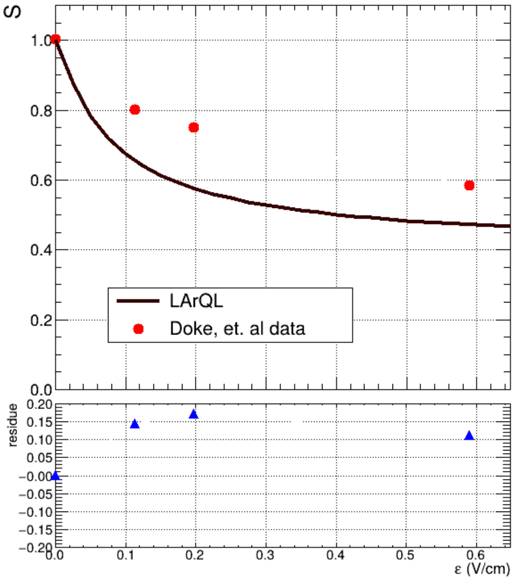

(i) Doke, *et al.*, $\frac{dE}{dx} = \mathrm{mip}$

FIGURE A.1 – Results for the 1^{st} optimization for the individual fit, with the parameters listed in Tab. 6.2. The red dots represent the experimental data, the dark maroon line, the estimation from the LArQL model, and the blue triangles, the residues. The graphs (a), (b), (c), and (d) show $S\left(\frac{dE}{dx}\right)$ correlations with fixed ε field. (e), (f), and (g) display $\mathscr{R}\left(\frac{dE}{dx}\right)$ correlations with fixed ε field. (h) shows $\mathscr{R}(\varepsilon)$, and (i) $S(\varepsilon)$ correlations.

Appendix B - Second stage graphs

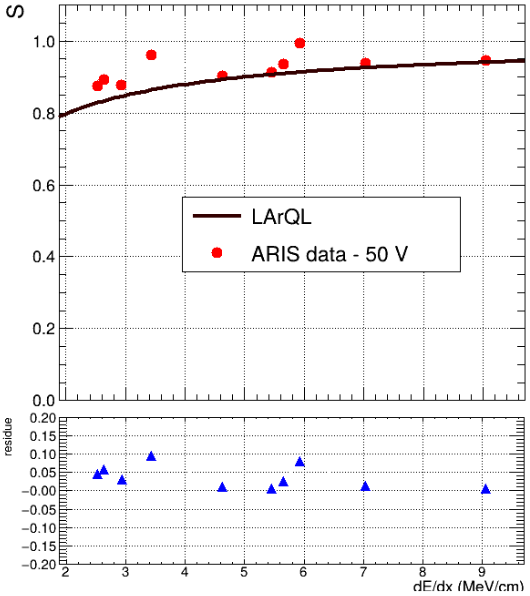

(a) ARIS data, $\varepsilon = 50\,\mathrm{V/cm}$

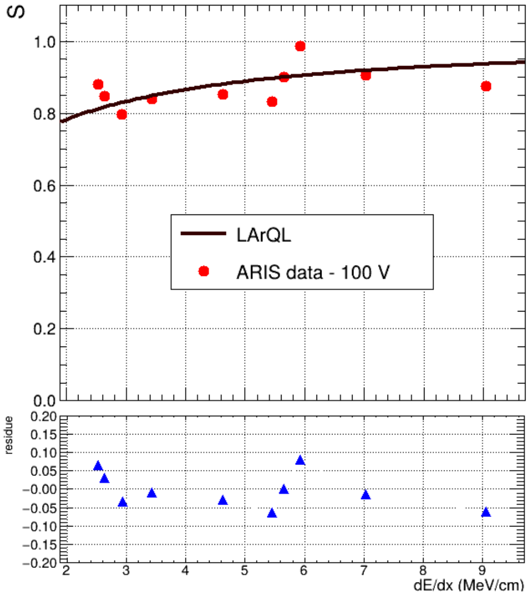

(b) ARIS data, $\varepsilon = 100\,\mathrm{V/cm}$

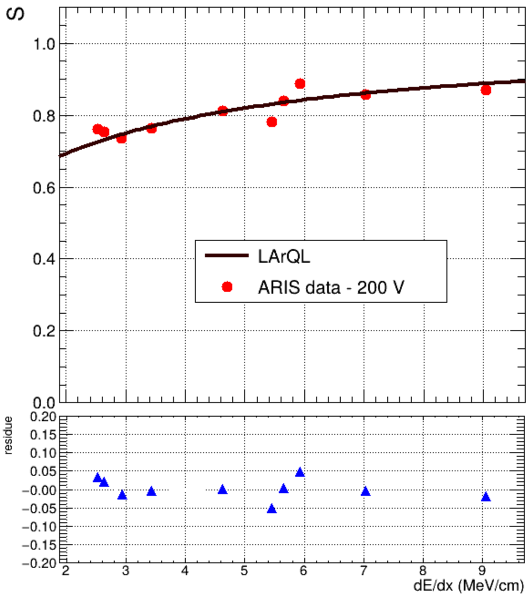

(c) ARIS data, $\varepsilon = 200\,\mathrm{V/cm}$

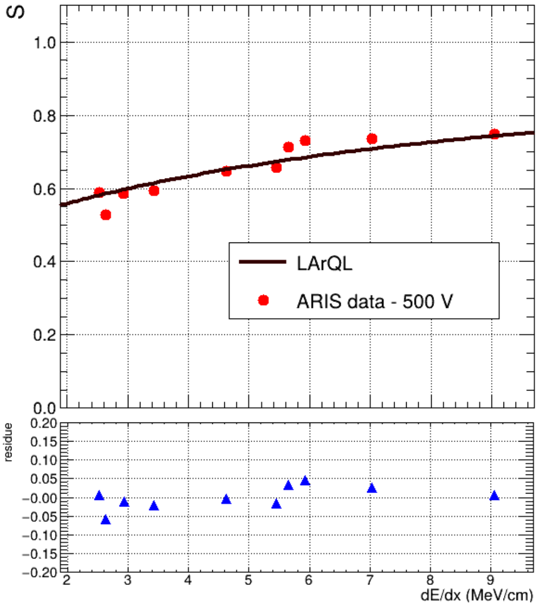

(d) ARIS data, $\varepsilon = 500\,\mathrm{V/cm}$

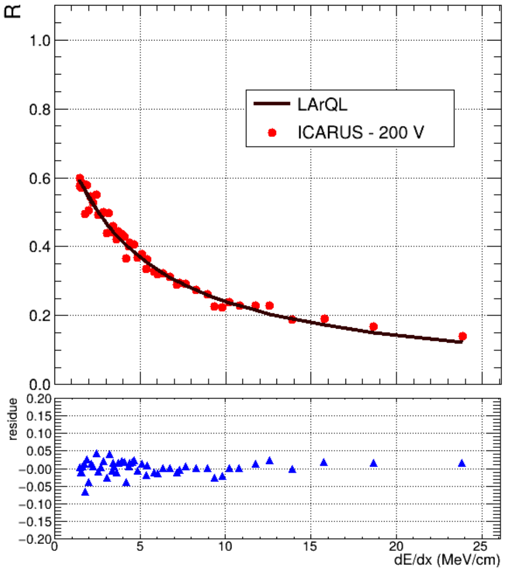

(e) ICARUS data, $\varepsilon = 200\,\mathrm{V/cm}$

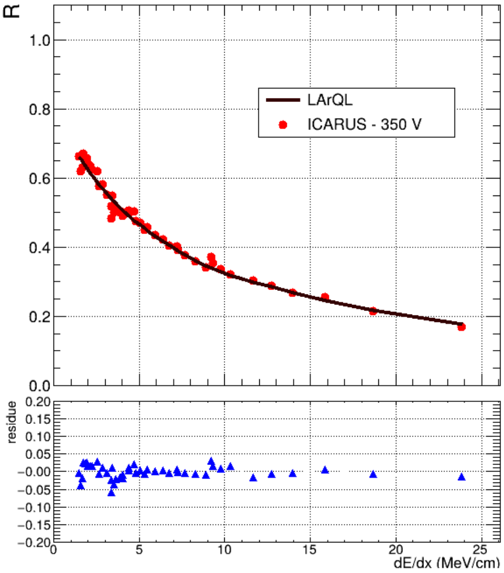

(f) ICARUS data, $\varepsilon = 350\,\mathrm{V/cm}$

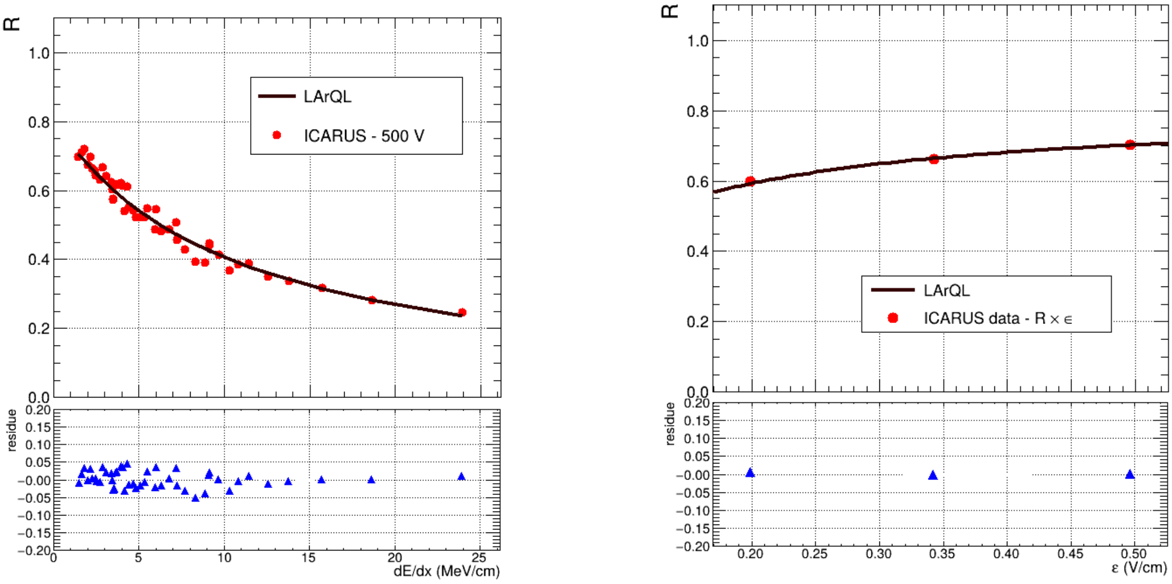

(g) ICARUS data, $\varepsilon = 500\,\mathrm{V/cm}$

(h) ICARUS data, $\frac{dE}{dx} = \mathrm{mip}$

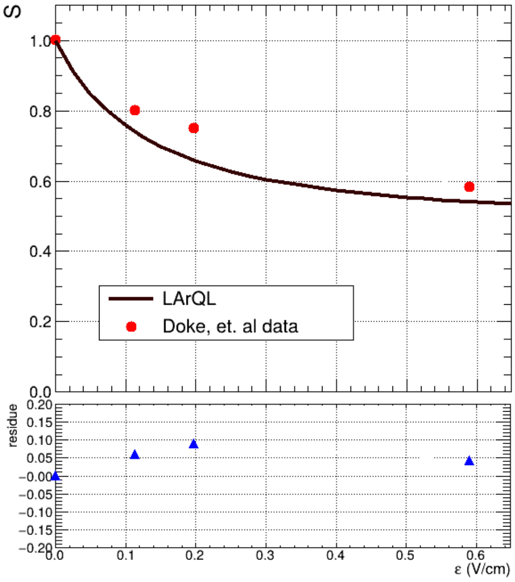

(i) Doke, *et al.*, $\frac{dE}{dx} = \mathrm{mip}$

FIGURE B.1 – Results for the 2^{nd} optimization for individual fit, with the parameters listed in tab. 6.5. The red dots represent the experimental data, the dark maroon line is the estimation from the LArQL model, and the blue triangles represent the residues.

Appendix C - Third stage graphs

Individual fit

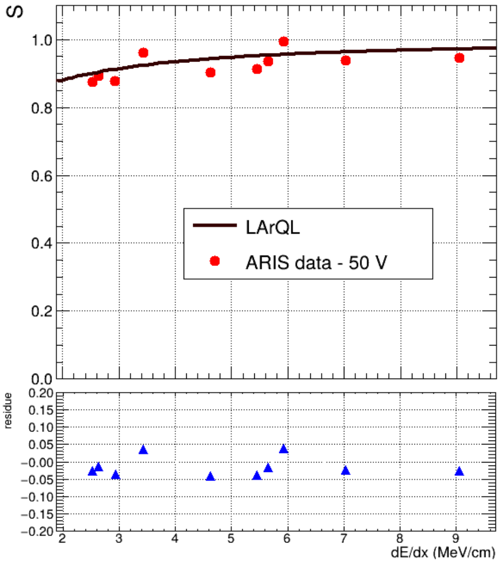

(a) ARIS data, $\varepsilon = 50\,\mathrm{V/cm}$

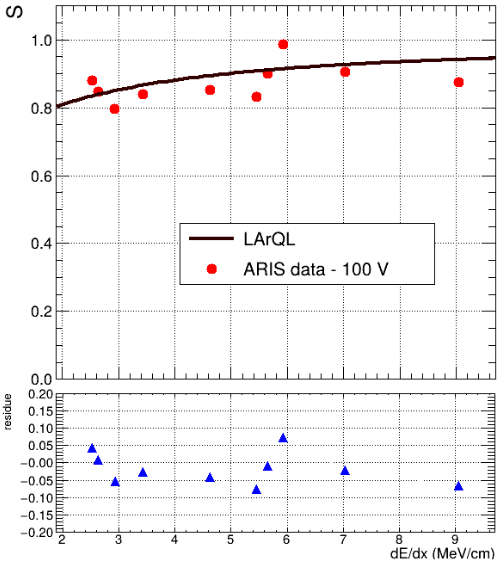

(b) ARIS data, $\varepsilon = 100\,\mathrm{V/cm}$

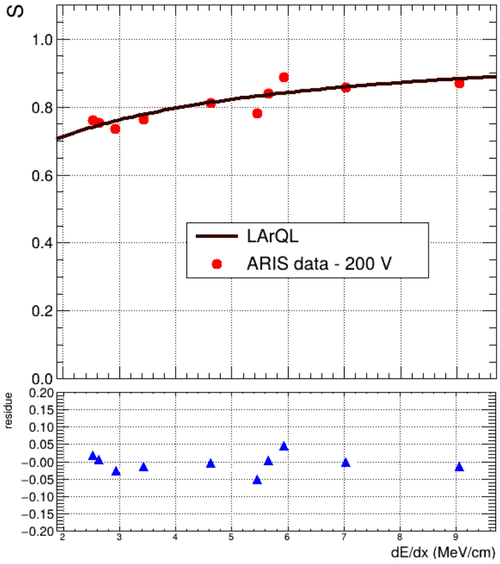

(c) ARIS data, $\varepsilon = 200\,\mathrm{V/cm}$

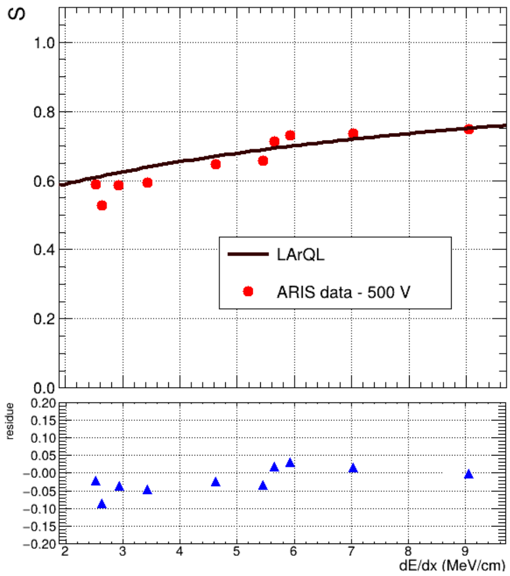

(d) ARIS data, $\varepsilon = 500\,\mathrm{V/cm}$

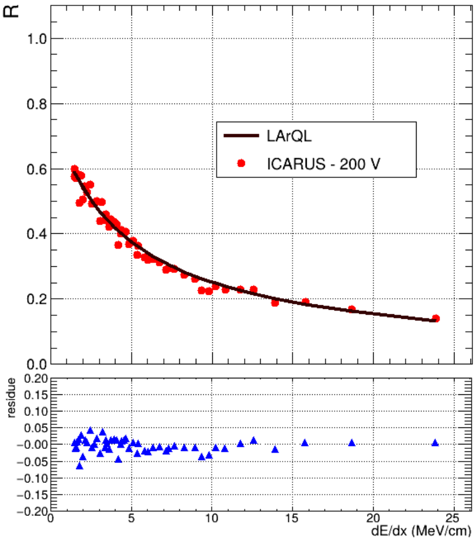

(e) ICARUS data, $\varepsilon = 200\,\mathrm{V/cm}$

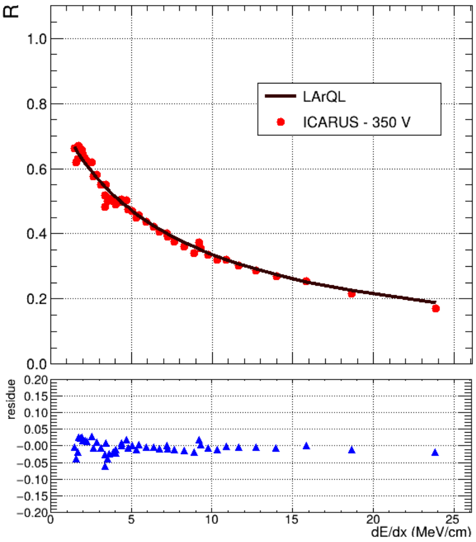

(f) ICARUS data, $\varepsilon = 350\,\mathrm{V/cm}$

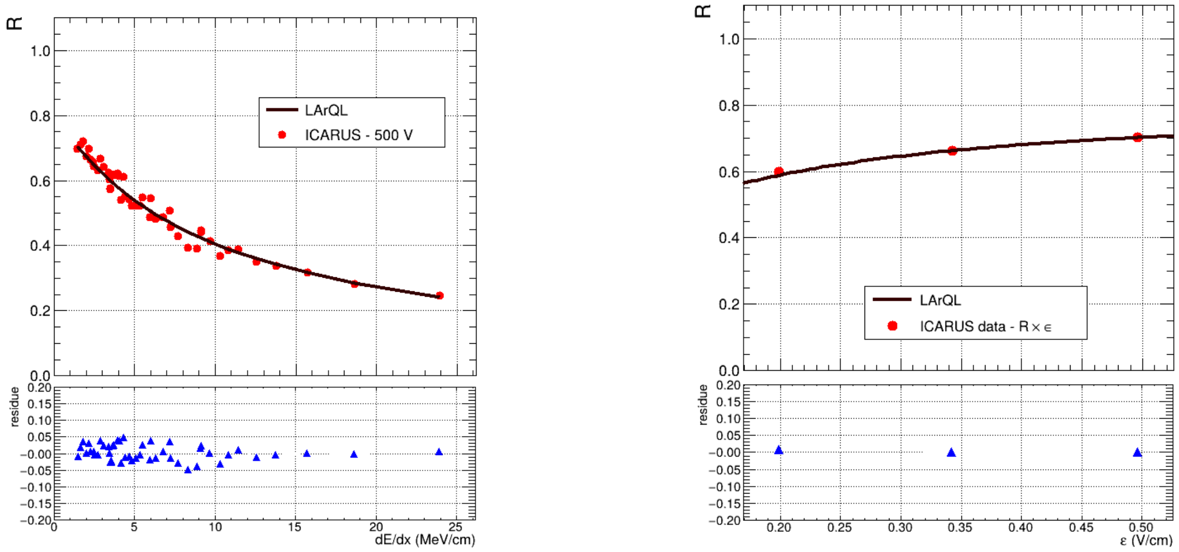

(g) ICARUS data, $\varepsilon = 500\,\mathrm{V/cm}$

(h) ICARUS data, $\frac{dE}{dx} = \text{mip}$

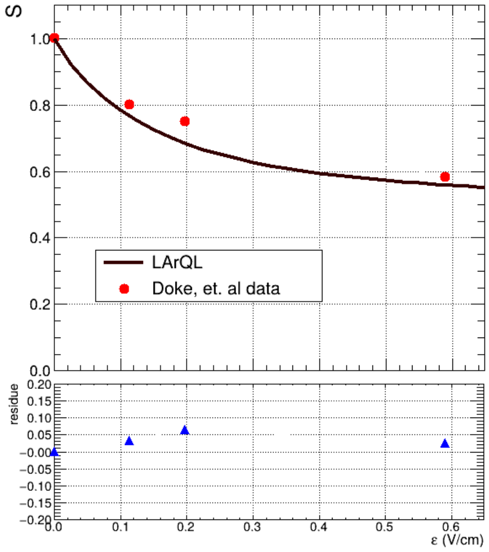

(i) Doke, *et al.*, $\frac{dE}{dx} = \text{mip}$

FIGURE C.1 – Results for the 3^{rd} optimization for the individual fit, with the parameters listed in tab. 6.6. The red dots represent the experimental data, the dark maroon line is the estimation from the LArQL model, and the blue triangles represent the residues.

Global fit

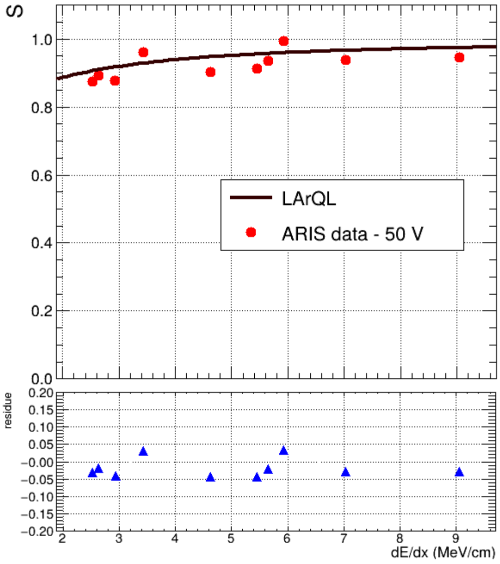

(a) ARIS data, $\varepsilon = 50\,\mathrm{V/cm}$

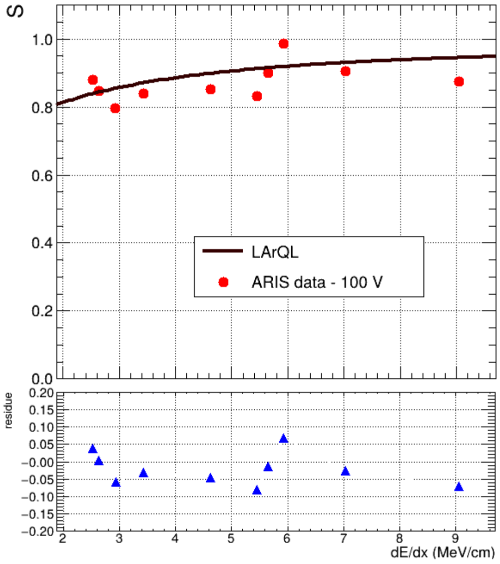

(b) ARIS data, $\varepsilon = 100\,\mathrm{V/cm}$

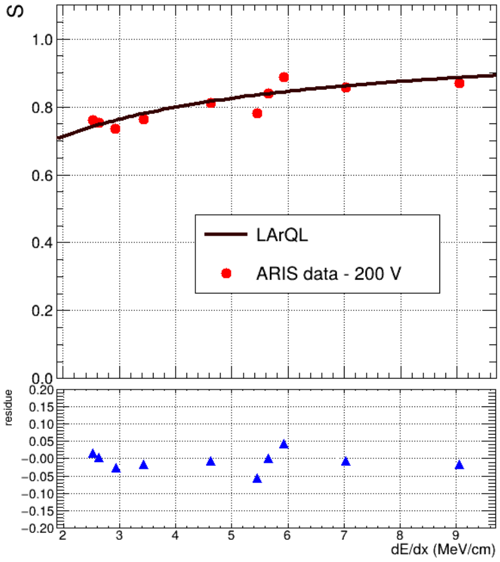

(c) ARIS data, $\varepsilon = 200\,\mathrm{V/cm}$

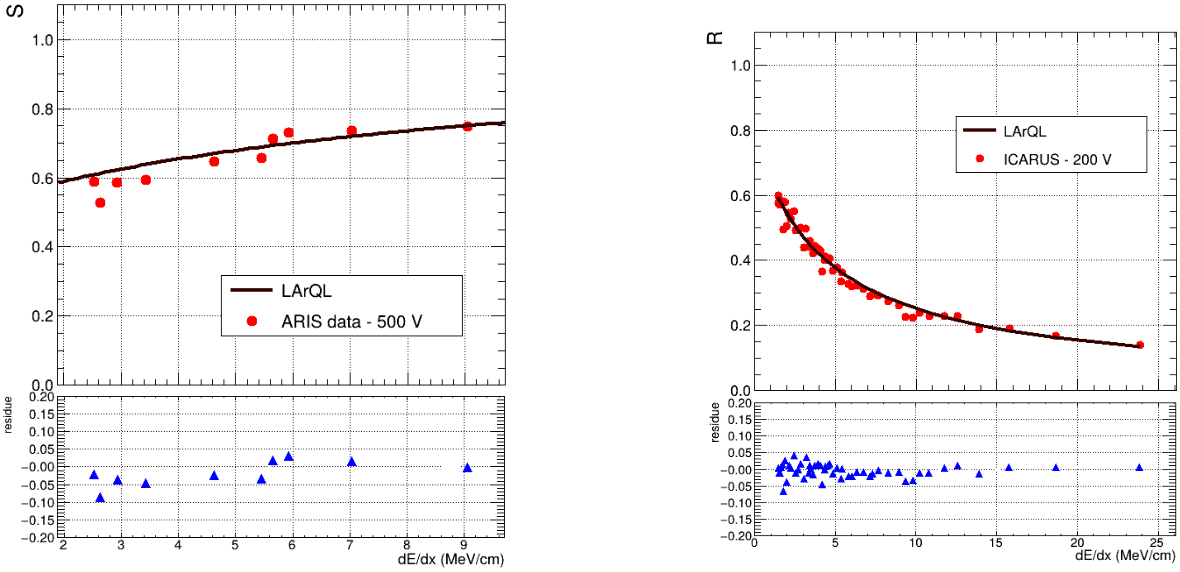

(d) ARIS data, $\varepsilon = 500\,\mathrm{V/cm}$

(e) ICARUS data, $\varepsilon = 200\,\mathrm{V/cm}$

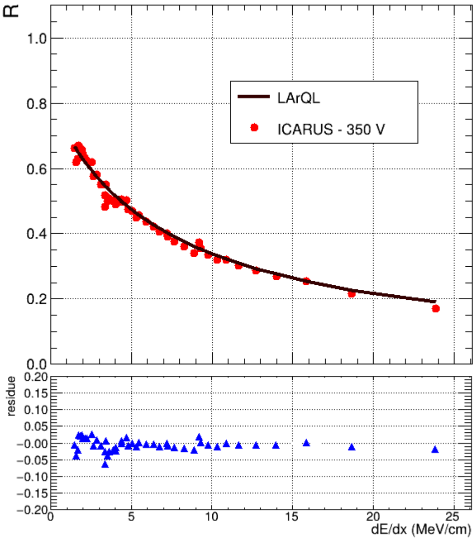

(f) ICARUS data, $\varepsilon = 350\,\mathrm{V/cm}$

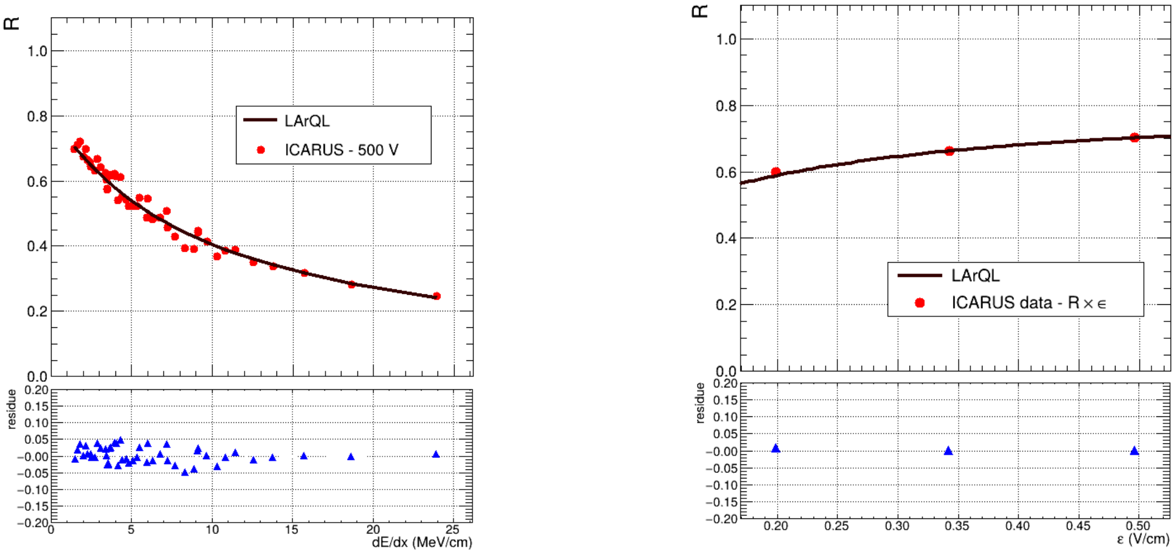

(g) ICARUS data, $\varepsilon = 500\,\mathrm{V/cm}$ (h) ICARUS data, $\frac{dE}{dx} = \mathrm{mip}$

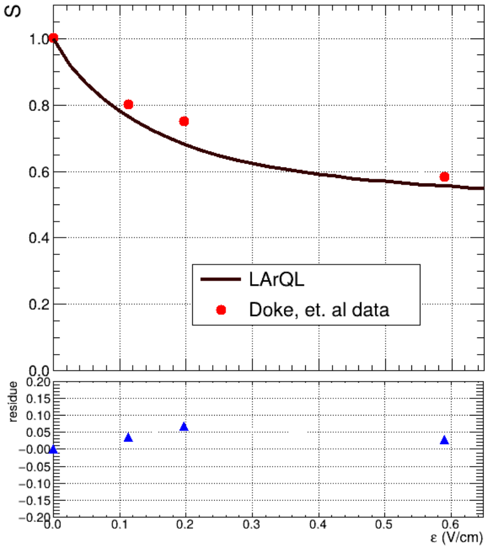

(i) Doke, *et al.*, $\frac{dE}{dx} = \mathrm{mip}$

FIGURE C.2 – Results for the 3^{rd} optimization for the global fit, with the parameters listed in tab. 6.7. The red dots represent the experimental data, the dark maroon line is the estimation from the LArQL model, and the blue triangles represent the residues.

Appendix D - Fourth stage graphs

Individual fit

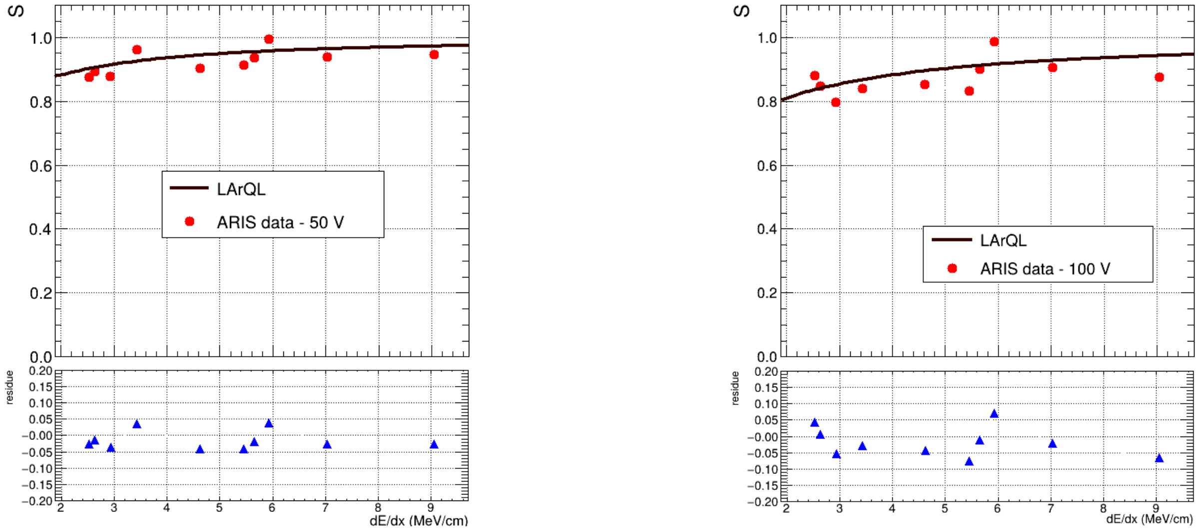

(a) ARIS data, $\varepsilon = 50\,\mathrm{V/cm}$

(b) ARIS data, $\varepsilon = 100\,\mathrm{V/cm}$

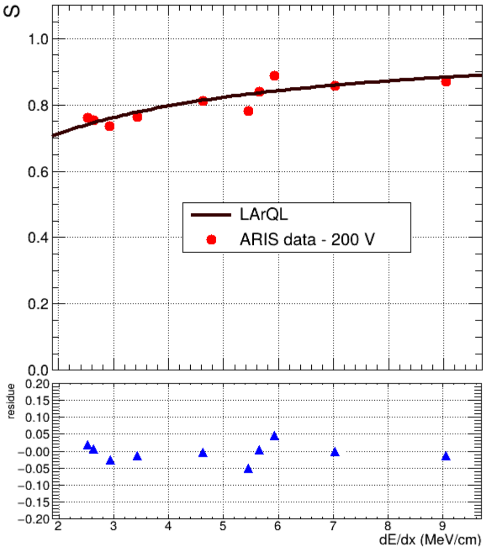

(c) ARIS data, $\varepsilon = 200\,\mathrm{V/cm}$

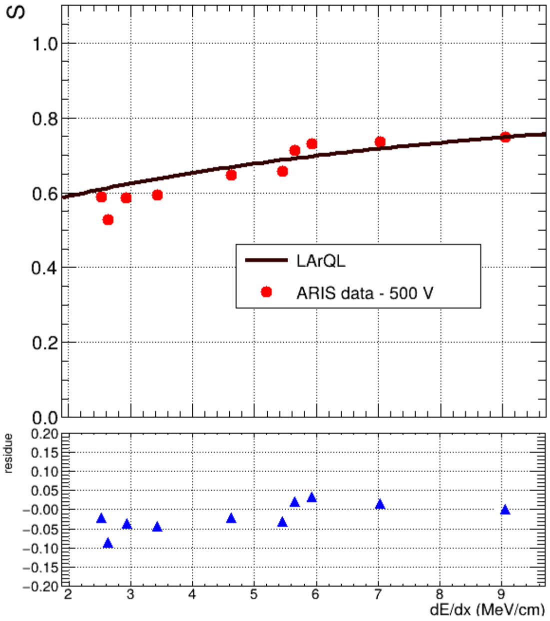

(d) ARIS data, $\varepsilon = 500\,\mathrm{V/cm}$

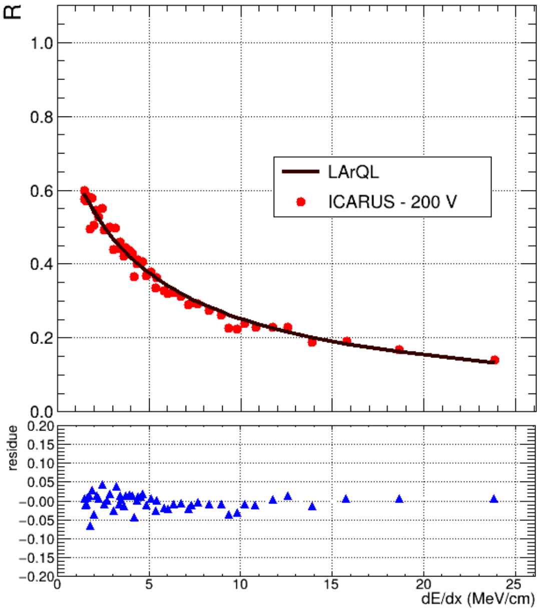

(e) ICARUS data, $\varepsilon = 200\,\mathrm{V/cm}$

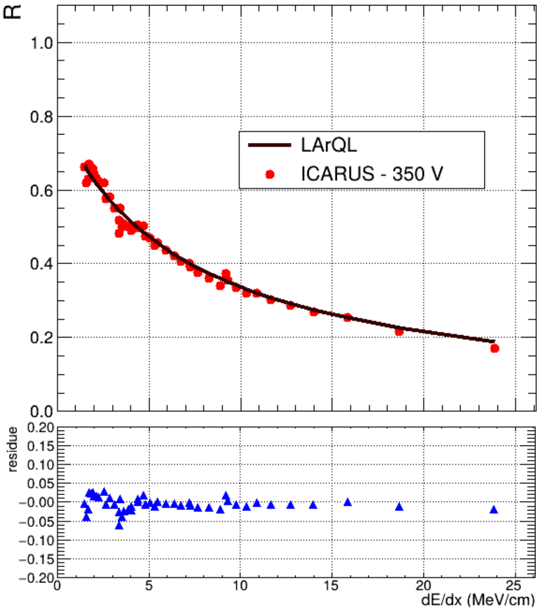

(f) ICARUS data, $\varepsilon = 350\,\mathrm{V/cm}$

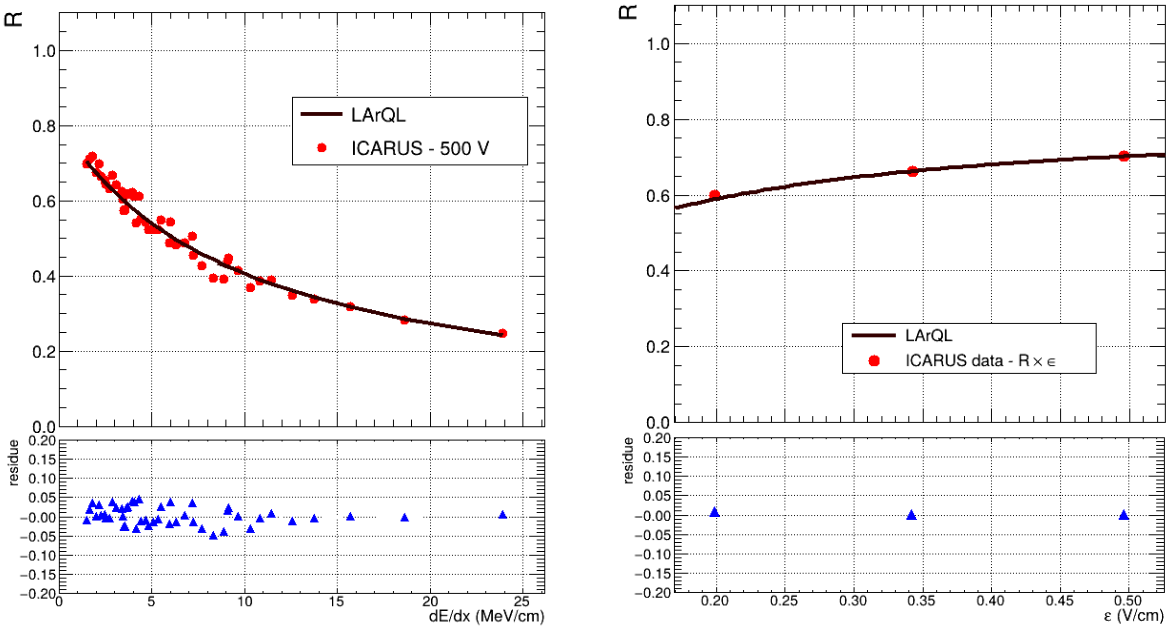

(g) ICARUS data, $\varepsilon = 500\,\mathrm{V/cm}$

(h) ICARUS data, $\frac{dE}{dx} = \mathrm{mip}$

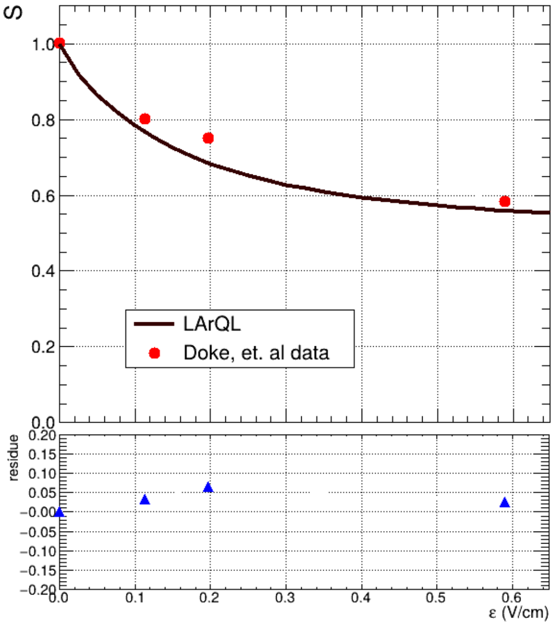

(i) Doke, *et al.*, $\frac{dE}{dx} = \mathrm{mip}$

FIGURE D.1 – Results for the 4^{th} stage (individual fit), with the parameters listed in tab. 6.9. The red dots represent the experimental data, the dark maroon line is the estimation from the LArQL model, and the blue triangles represent the residues.

Global fit

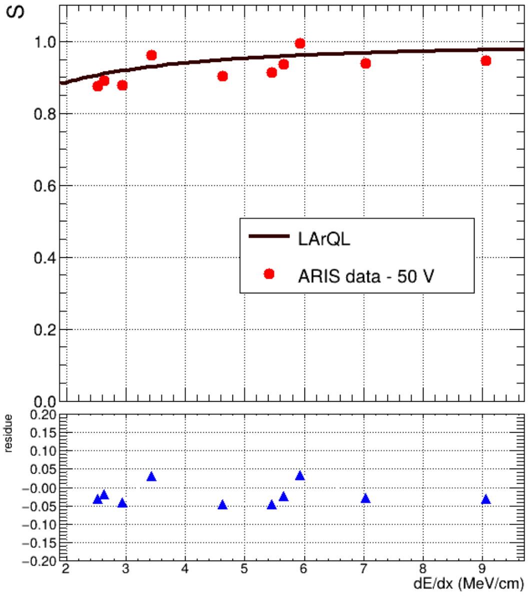

(a) ARIS data, $\varepsilon = 50\,\mathrm{V/cm}$

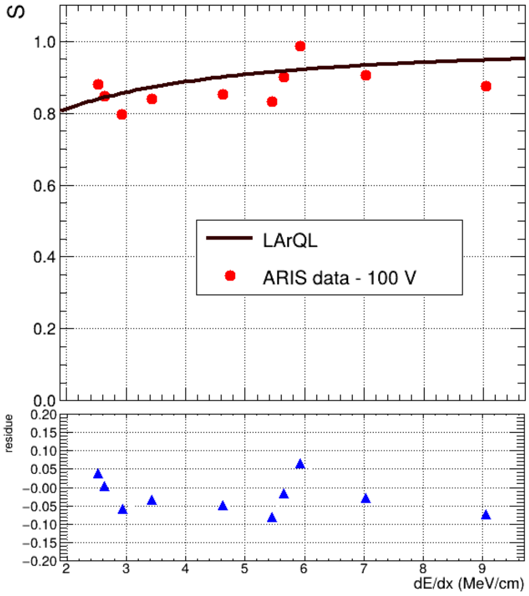

(b) ARIS data, $\varepsilon = 100\,\mathrm{V/cm}$

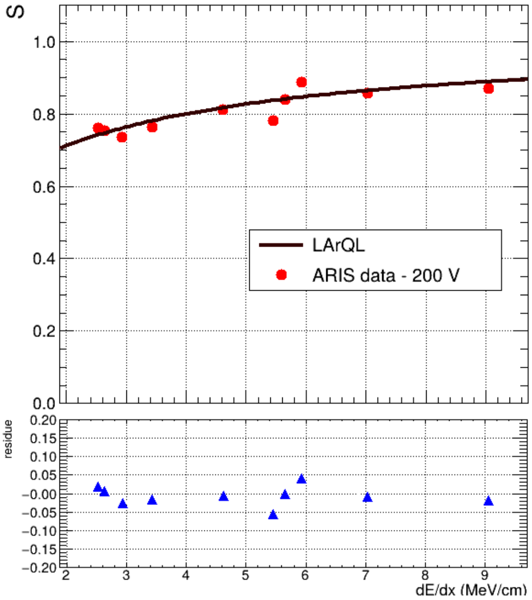

(c) ARIS data, $\varepsilon = 200\,\mathrm{V/cm}$

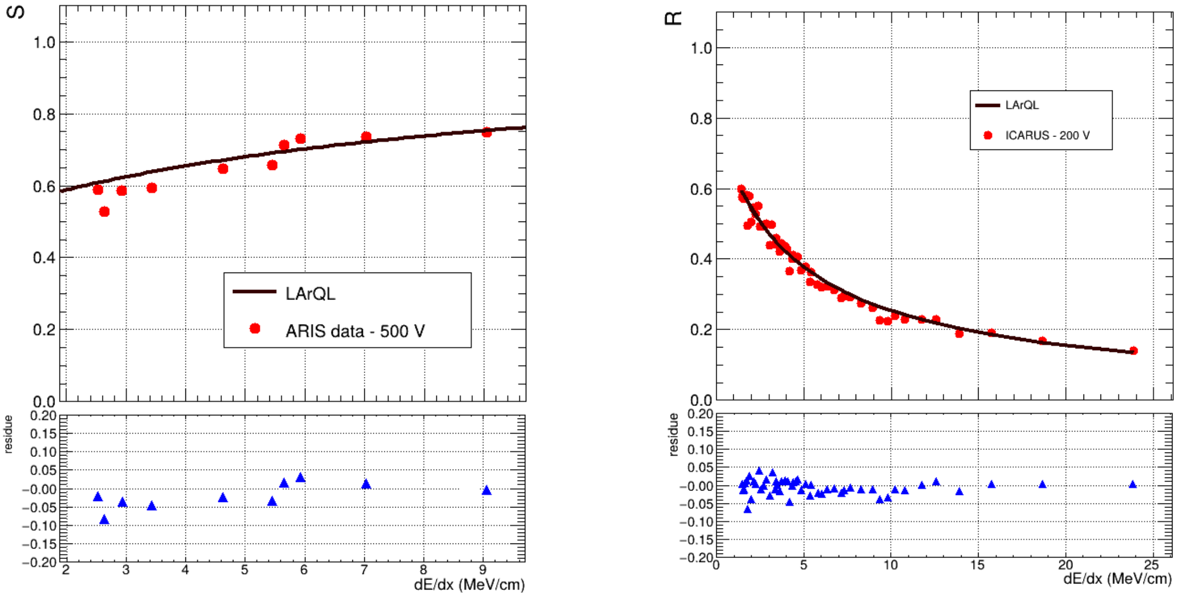

(d) ARIS data, $\varepsilon = 500\,\mathrm{V/cm}$

(e) ICARUS data, $\varepsilon = 200\,\mathrm{V/cm}$

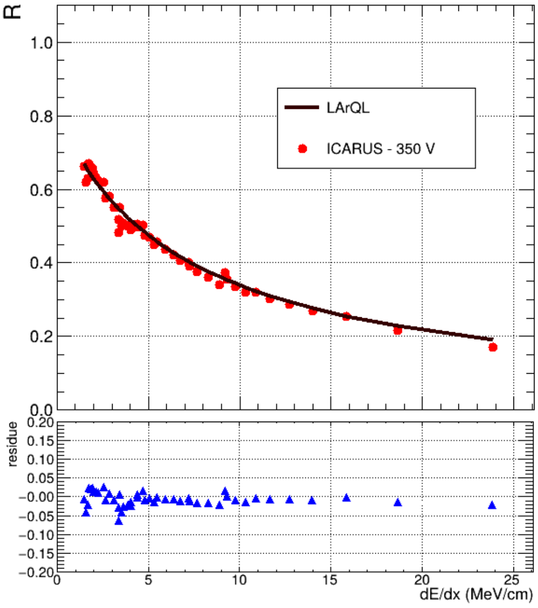

(f) ICARUS data, $\varepsilon = 350\,\mathrm{V/cm}$

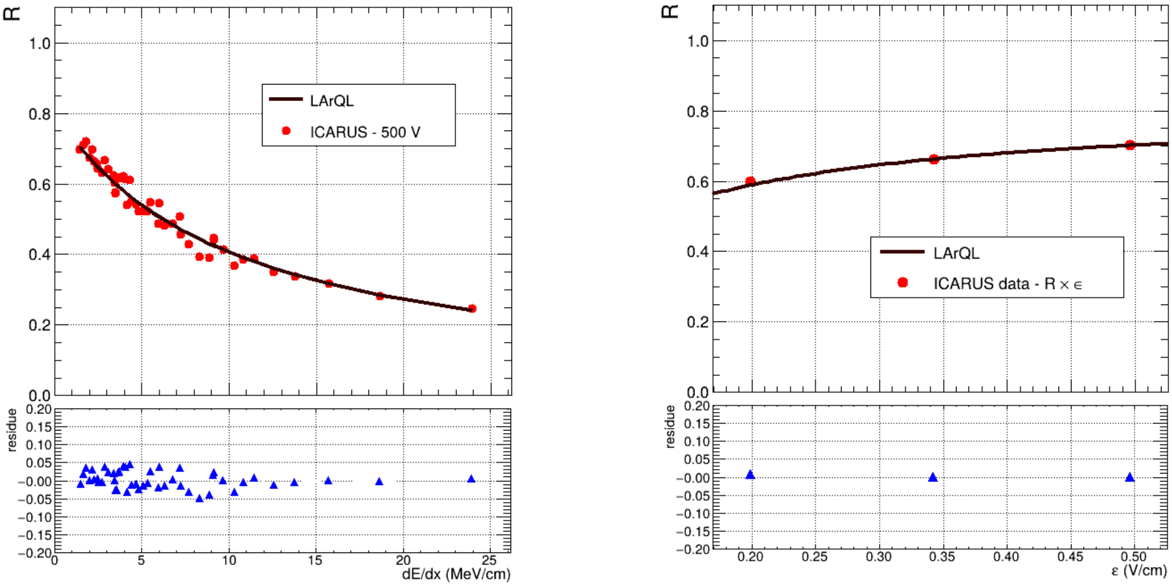

(g) ICARUS data, $\varepsilon = 500\,\mathrm{V/cm}$

(h) ICARUS data, $\frac{dE}{dx} = \mathrm{mip}$

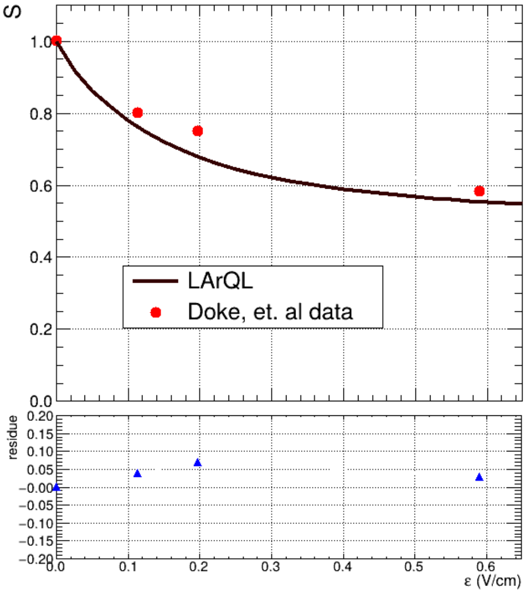

(i) Doke, *et al.*, $\frac{dE}{dx} = \mathrm{mip}$

FIGURE D.2 – Results for the 4^{th} stage (global, single sample), with the parameters listed in tab. 6.11. The red dots represent the experimental data, the dark maroon line is the estimation from the LArQL model, and the blue triangles represent the residues.

Global fit (result from 30 samples)

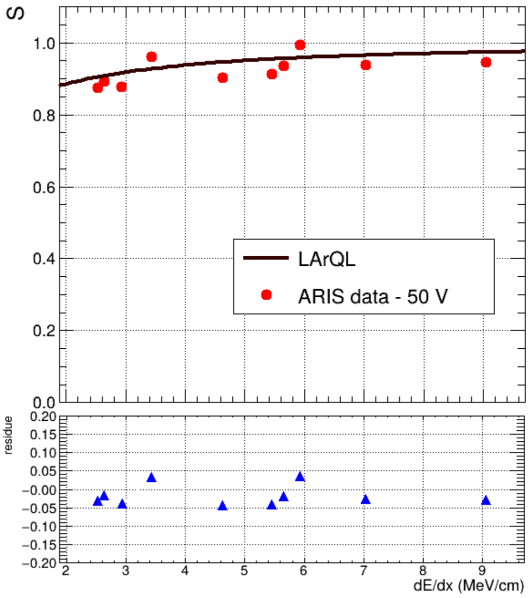

(a) ARIS data, $\varepsilon = 50$ V/cm

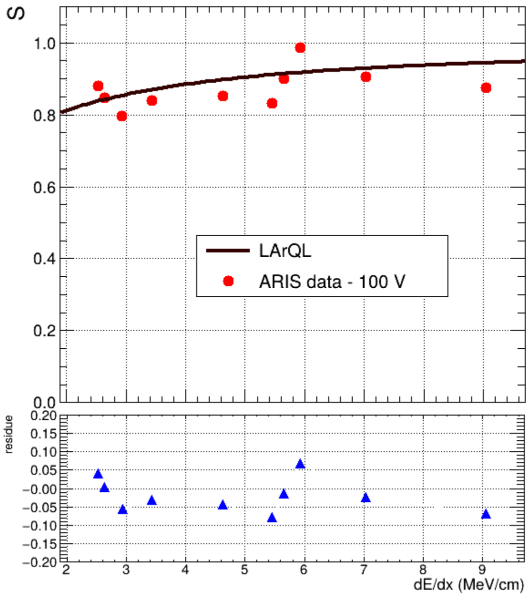

(b) ARIS data, $\varepsilon = 100$ V/cm

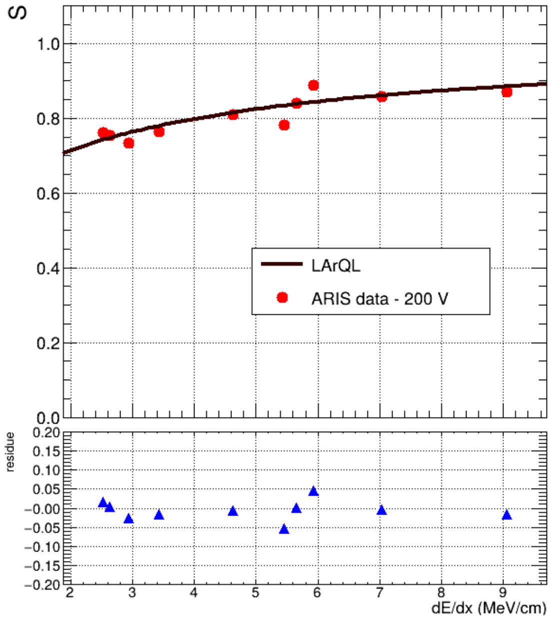

(c) ARIS data, $\varepsilon = 200$ V/cm

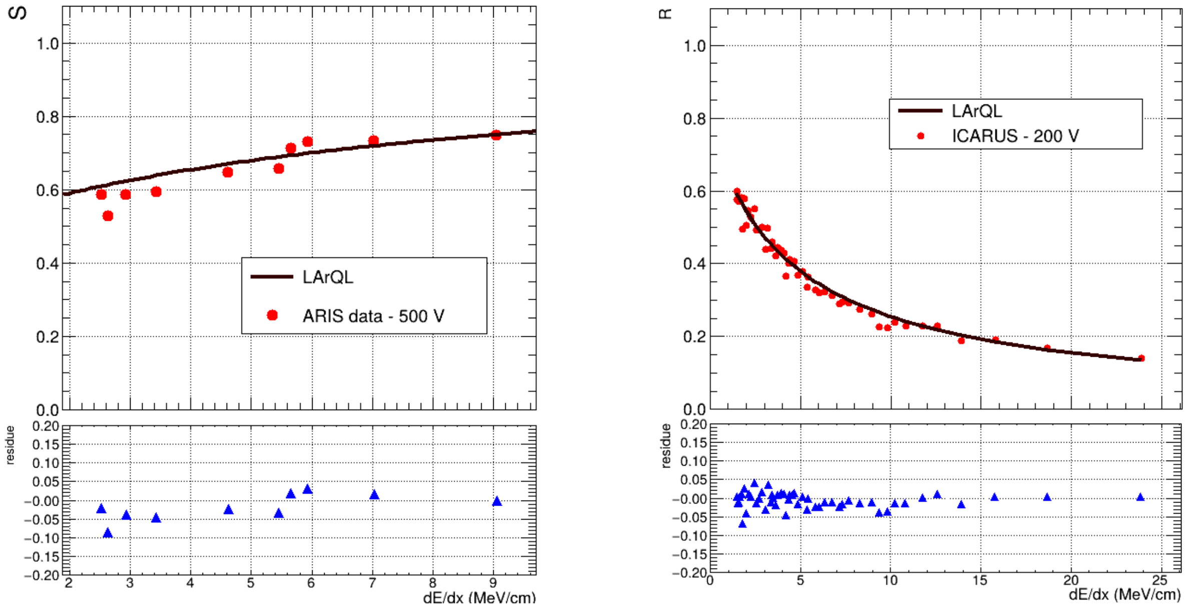

(d) ARIS data, $\varepsilon = 500$ V/cm

(e) ICARUS data, $\varepsilon = 200$ V/cm

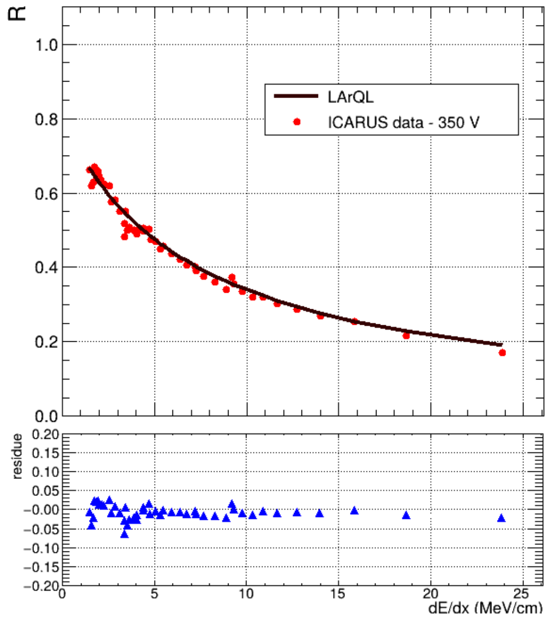

(f) ICARUS data, $\varepsilon = 350$ V/cm

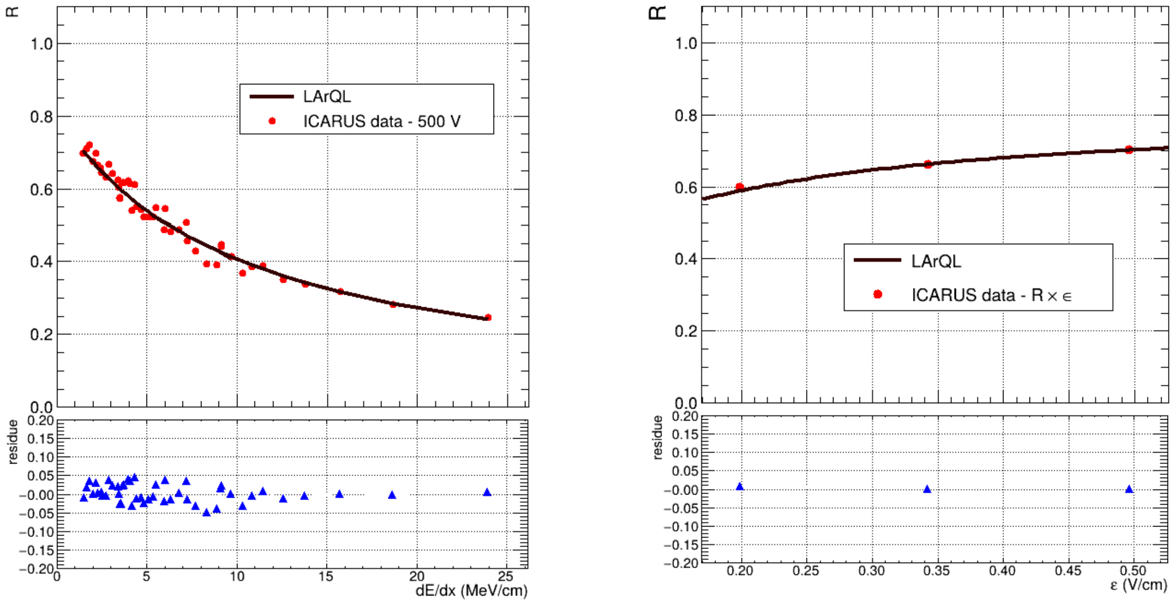

(g) ICARUS data, $\varepsilon = 500$ V/cm

(h) ICARUS data, $\frac{dE}{dx} = mip$

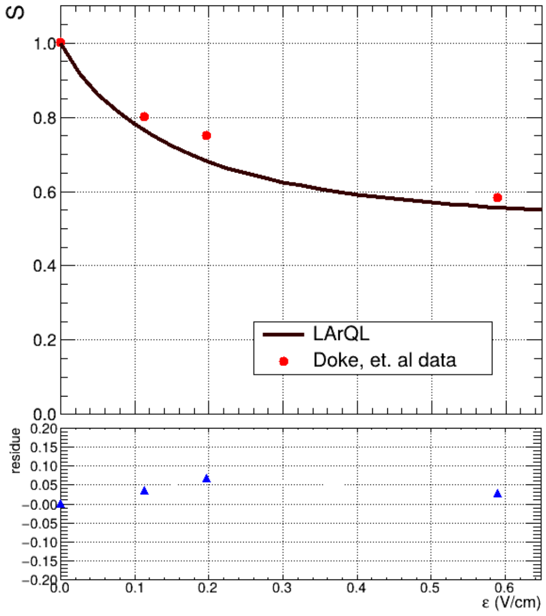

(i) Doke, *et al.*, $\frac{dE}{dx} = mip$

FIGURE D.3 – Results for the global parameters showed in tab. 6.11, obtained from 30 samples listed in tab. 6.12 from 4^{th} optimization. The red dots represent the experimental data, the dark maroon line estimations from the LArQL model, and the blue triangles. The graphs (a), (b), (c), and (d) show $S\left(\frac{dE}{dx}\right)$ correlations. (e), (f) and (g) $\mathscr{R}\left(\frac{dE}{dx}\right)$ correlation. (h) shows $\mathscr{R}(\varepsilon)$ and (i), the $S(\varepsilon)$ correlations.

Appendix E - Fourth stage 30-samples parameter results

TABLE E.1 – Parameter sets and SSR results obtained from the sampling of the 4^{th} optimization stage (global parameters from tab. 6.11).

Sample	**WSSR**	k_B **(g V/cm^{3}MeV)**	A_B	$\chi_0 1$	$\chi_0 2$	$\chi_0 3$	$\chi_0 4$ $(\mathrm{MeV/cm})^{-1}$	α **(V/cm)**	β **(V/cm)**
1	10.75	49.73	0.808	3.63×10^{-3}	-5.73	1.75	2.03×10^{-4}	3.82×10^{-2}	1.33×10^{-2}
2	10.12	49.76	0.808	3.56×10^{-3}	-5.73	1.75	1.99×10^{-4}	3.90×10^{-2}	1.22×10^{-2}
3	10.07	49.85	0.808	3.56×10^{-3}	-5.73	1.75	2.05×10^{-4}	3.94×10^{-2}	1.23×10^{-2}
4	9.92	49.81	0.808	3.62×10^{-3}	-5.72	1.75	2.05×10^{-4}	3.92×10^{-2}	1.22×10^{-2}
5	9.90	49.78	0.808	3.57×10^{-3}	-5.73	1.75	2.02×10^{-4}	3.90×10^{-2}	1.30×10^{-2}
6	9.73	49.61	0.808	3.57×10^{-3}	-5.72	1.75	2.05×10^{-4}	3.75×10^{-2}	1.31×10^{-2}
7	10.56	49.71	0.808	3.61×10^{-3}	-5.63	1.73	2.05×10^{-4}	3.83×10^{-2}	1.33×10^{-2}
8	9.76	49.78	0.807	3.56×10^{-3}	-5.66	1.74	2.04×10^{-4}	3.86×10^{-2}	1.34×10^{-2}
9	10.09	49.72	0.808	3.56×10^{-3}	-5.74	1.75	1.98×10^{-4}	3.81×10^{-2}	1.29×10^{-2}
10	10.02	49.71	0.808	3.56×10^{-3}	-5.73	1.75	2.05×10^{-4}	3.84×10^{-2}	1.20×10^{-2}
11	10.60	49.77	0.808	3.60×10^{-3}	-5.73	1.75	2.05×10^{-4}	3.85×10^{-2}	1.28×10^{-2}
12	10.13	49.77	0.808	3.58×10^{-3}	-5.74	1.75	2.03×10^{-4}	3.87×10^{-2}	1.25×10^{-2}
13	10.27	49.76	0.808	3.56×10^{-3}	-5.70	1.74	2.02×10^{-4}	3.85×10^{-2}	1.33×10^{-2}
14	10.00	49.52	0.807	3.58×10^{-3}	-5.75	1.75	2.03×10^{-4}	3.79×10^{-2}	1.19×10^{-2}
15	10.34	49.83	0.808	3.56×10^{-3}	-5.68	1.74	2.05×10^{-4}	3.87×10^{-2}	1.22×10^{-2}
16	10.42	49.97	0.808	3.57×10^{-3}	-5.72	1.75	2.04×10^{-4}	3.99×10^{-2}	1.30×10^{-2}
17	10.21	49.62	0.808	3.56×10^{-3}	-5.68	1.74	2.05×10^{-4}	3.72×10^{-2}	1.32×10^{-2}
18	10.64	49.81	0.808	3.57×10^{-3}	-5.73	1.75	2.04×10^{-4}	3.88×10^{-2}	1.22×10^{-2}
19	10.05	49.59	0.807	3.56×10^{-3}	-5.68	1.74	2.05×10^{-4}	3.74×10^{-2}	1.28×10^{-2}
20	9.64	49.73	0.808	3.64×10^{-3}	-5.64	1.73	2.05×10^{-4}	3.88×10^{-2}	1.24×10^{-2}
21	9.93	49.53	0.807	3.56×10^{-3}	-5.73	1.75	2.02×10^{-4}	3.81×10^{-2}	1.29×10^{-2}
22	10.40	49.79	0.808	3.60×10^{-3}	-5.72	1.75	2.05×10^{-4}	3.97×10^{-2}	1.20×10^{-2}
23	9.82	49.78	0.808	3.58×10^{-3}	-5.73	1.75	2.05×10^{-4}	3.87×10^{-2}	1.26×10^{-2}
24	10.17	49.84	0.808	3.58×10^{-3}	-5.70	1.74	2.04×10^{-4}	3.90×10^{-2}	1.25×10^{-2}
25	10.41	49.78	0.808	3.61×10^{-3}	-5.67	1.74	2.05×10^{-4}	3.90×10^{-2}	1.22×10^{-2}
26	10.21	49.97	0.808	3.59×10^{-3}	-5.71	1.75	2.04×10^{-4}	4.00×10^{-2}	1.24×10^{-2}
27	9.63	49.79	0.808	3.56×10^{-3}	-5.71	1.74	2.06×10^{-4}	3.90×10^{-2}	1.26×10^{-2}
28	10.44	49.68	0.808	3.56×10^{-3}	-5.65	1.73	2.02×10^{-4}	3.82×10^{-2}	1.28×10^{-2}
29	10.28	49.75	0.808	3.57×10^{-3}	-5.66	1.74	2.03×10^{-4}	3.90×10^{-2}	1.24×10^{-2}
30 (best results)	9.59	49.73	0.808	3.61×10^{-3}	-5.68	1.74	2.01×10^{-4}	3.87×10^{-2}	1.28×10^{-2}

Appendix F - Correlation factor histograms

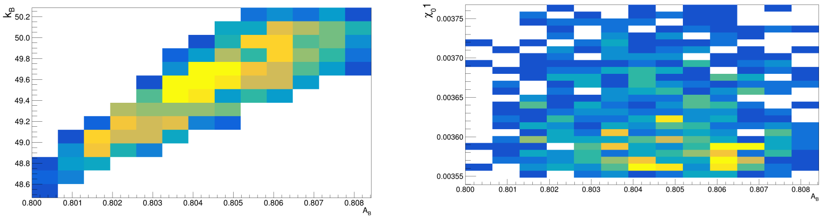

(a) Correlation between $k_B(A_B)$

(b) Correlation between $\chi_0 1(A_B)$

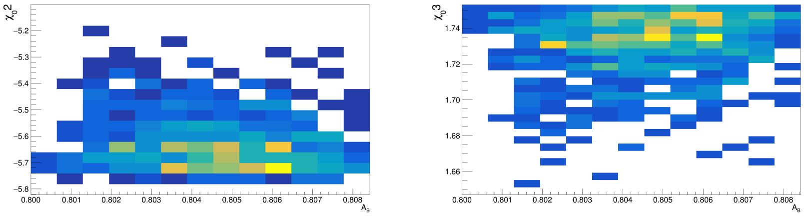

(c) Correlation between $\chi_0 2(A_B)$

(d) Correlation between $\chi_0 3(A_B)$

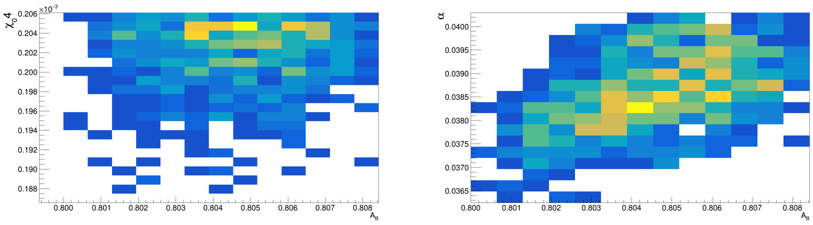

(e) Correlation between $\chi_0 4(A_B)$

(f) Correlation between $\alpha(A_B)$

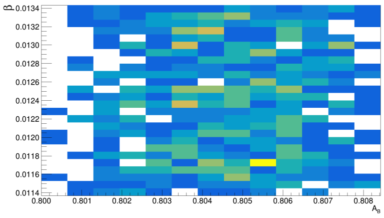

(g) Correlation between $\beta(A_B)$

FIGURE F.1 – Histograms of the correlation between A_B with other parameters.

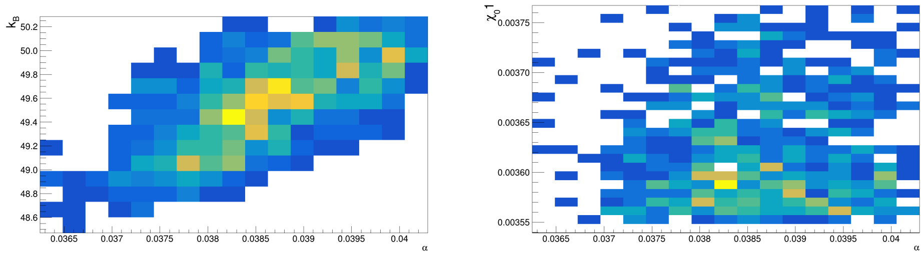

(a) Correlation between $k_B(\alpha)$ (b) Correlation between $\chi_0 1(\alpha)$

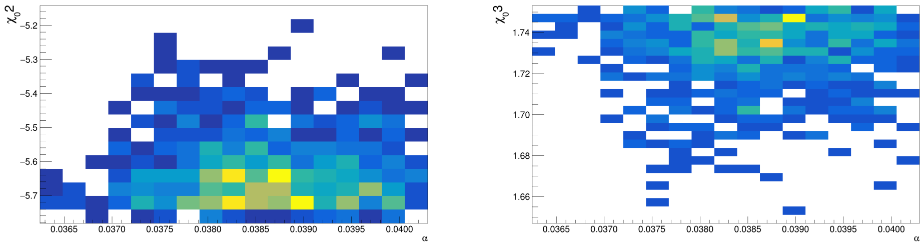

(c) Correlation between $\chi_0 2(\alpha)$ (d) Correlation between $\chi_0 3(\alpha)$

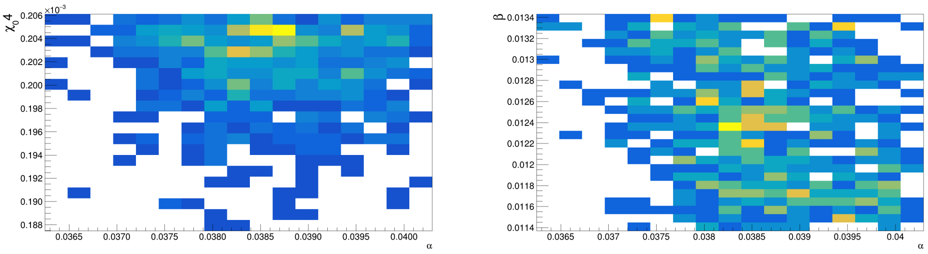

(e) Correlation between $\chi_0 4(\alpha)$ (f) Correlation between $\beta(\alpha)$

FIGURE F.2 – Histograms of the correlation between α with other parameters.

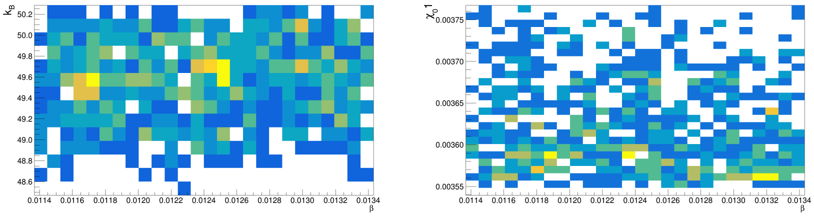

(a) Correlation between $k_B(\beta)$ (b) Correlation between $\chi_0 1(\beta)$

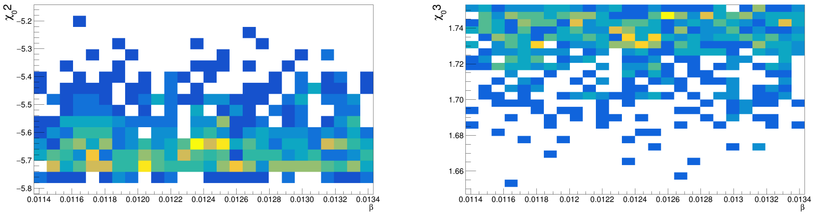

(c) Correlation between $\chi_0 2(\beta)$ (d) Correlation between $\chi_0 3(\beta)$

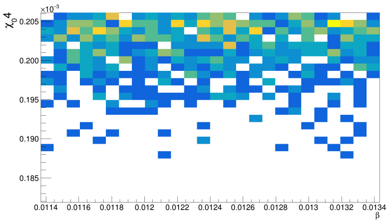

(e) Correlation between $\chi_0 4(\beta)$

FIGURE F.3 – Histograms of the correlation between β with other parameters.

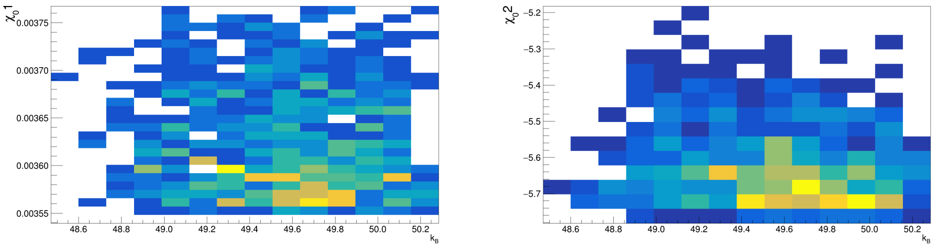

(a) Correlation between $\chi_0 1(k_B)$ (b) Correlation between $\chi_0 2(k_B)$

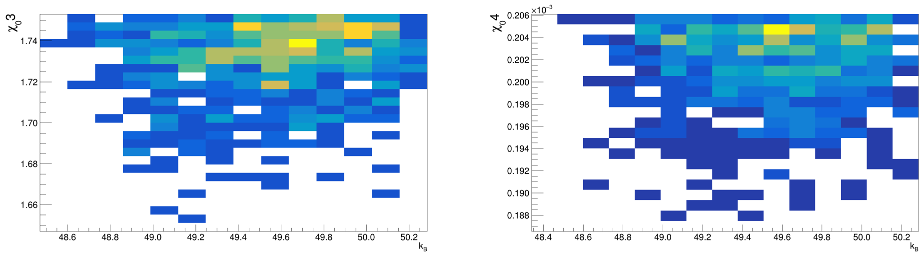

(c) Correlation between $\chi_0 3(k_B)$ (d) Correlation between $\chi_0 4(k_B)$

FIGURE F.4 – Histograms of the correlation between k_B with other parameters.

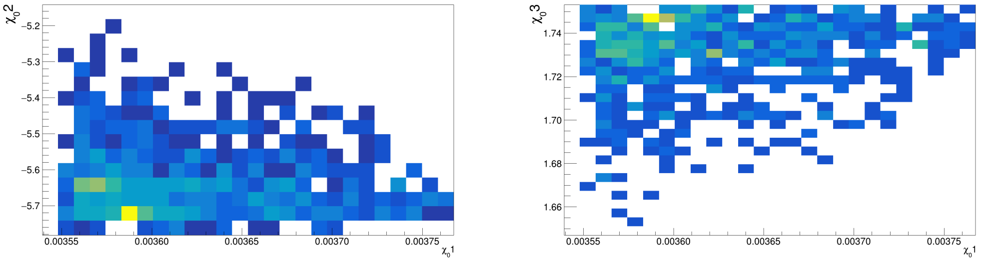

(a) Correlation between $\chi_0 2(\chi_0 1)$ (b) Correlation between $\chi_0 3(\chi_0 1)$

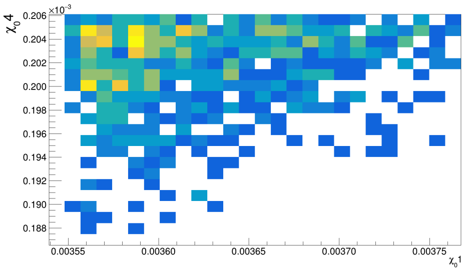

(c) Correlation between $\chi_0 4(\chi_0 1)$

FIGURE F.5 – Histograms of the correlation between $\chi_0 1$ with other parameters.

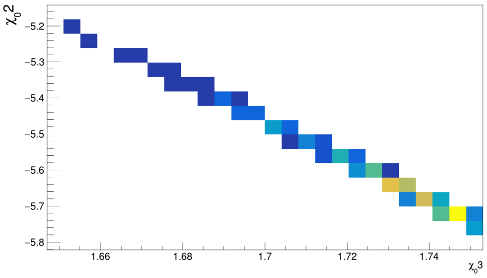

(a) Correlation between $\chi_0 3(\chi_0 2)$

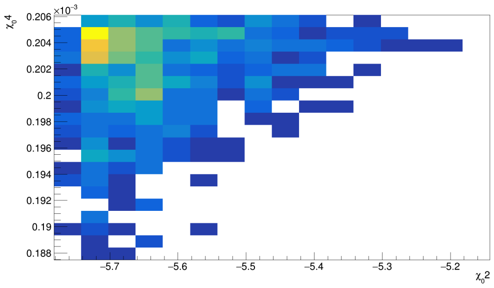

(b) Correlation between $\chi_0 4(\chi_0 2)$

FIGURE F.6 – Histograms of the correlation between $\chi_0 2$ with other parameters.

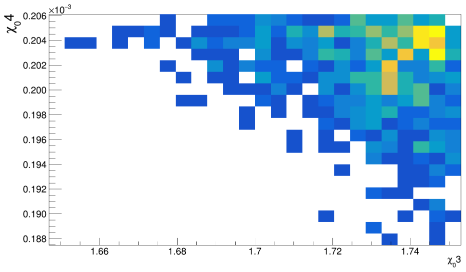

FIGURE F.7 – Histogram of the correlation between $\chi_0 3$ with $\chi_0 4$.

FOLHA DE REGISTRO DO DOCUMENTO

1. CLASSIFICAÇÃO/TIPO DM	2. DATA 22 de maio de 2025	3. DOCUMENTO Nº DCTA/ITA/DM-021/2025	4. Nº DE PÁGINAS 139

5. TÍTULO E SUBTÍTULO:

Studies of scintillation light and ionization charge production in Liquid Argon

6. AUTORA(ES):

Valéria Cristina Souza do Vale

7. INSTITUIÇÃO(ÕES)/ÓRGÃO(S) INTERNO(S)/DIVISÃO(ÕES):

Instituto Tecnológico de Aeronáutica – ITA

8. PALAVRAS-CHAVE SUGERIDAS PELA AUTORA:

Cintilação em argônio líquido; Detecção de neutrinos; Física de partículas experimental

9. PALAVRAS-CHAVE RESULTANTES DE INDEXAÇÃO:

Neutrinos; Cintilação; Interações de partículas; Detecção de neutrinos; Argônio; Propagação da luz; Física nuclear; Física

10. APRESENTAÇÃO: **(X) Nacional** **( ) Internacional**

ITA, São José dos Campos. Curso de Mestrado. Programa de Pós-Graduação em Física. Área de Física Nuclear. Orientador: Prof. Dr. Franciole da Cunha Marinho. Defesa em 25/04/2025. Publicada em 2025.

11. RESUMO:

Neutrino physics is a branch of particle physics dedicated to studying the properties of these particles and their interactions with matter. Although many characteristics of neutrinos are known due to extensive theoretical and experimental efforts over several decades, numerous open questions remain. This motivates the development of technologies such as Liquid Argon Time Projection Chamber (LArTPC) detectors. Next-generation experiments, such as the Deep Underground Neutrino Experiment (DUNE), advance these technologies to investigate neutrino oscillation parameters, CP symmetry violation, and search for physics beyond the Standard Model. Quantifying the production of ionization charge and scintillation light induced by the passage of relativistic charged particles in liquid argon is crucial for the performance of LArTPCs. This work aims to improve the phenomenological model LArQL, which describes the anticorrelation between free charge (Q) and scintillation light (L) production, incorporating recombination and escape charge effects in low electric field regions. The model accounts for the total number of produced quanta, recombination based on Birks' model, electric field dependence, and the average energy per ion pair production. The research will be organized into two main stages. Global fit: Integration of nine electron recoil (ER) datasets in liquid argon, correlating charge, scintillation, electric field, and deposited energy. Model validation: Testing against nine ER datasets not included in the fitting process to assess the model's accuracy and robustness. The proposed adjustments improve the variance of charge and scintillation estimates for ER by $\sim 6.64\%$ for the datasets included in the fit, as evaluated by the average reduction in the Sum of Squared Residuals (SSR) compared to the original LArQL model parameters. Furthermore, for the datasets not included in the fit, the model provided a satisfactory representation of both light and charge data across different experiments.

12. GRAU DE SIGILO:

(X) OSTENSIVO ( ) **RESERVADO** ( ) **SECRETO**